Ab initio calculations of water and ice: structural, electronic, and optical properties

Andreas Hermann

January 16, 2009

A thesis submitted in partial fulfillment of the
requirements of the degree of
Doctor of Philosophy
at
Massey University, Albany
New Zealand

Abstract

Extended aqueous systems, crystalline ice and liquid water, are studied computationally to investigate their ground state and excited state properties. Methods from solid state physics and quantum chemistry are combined to shed light on some of the unusual properties of water and ice.

For the ground state of crystalline ice, density functional theory (DFT) calculations are compared to an *ab initio* incremental ansatz that utilizes periodic Hartree-Fock together with localized electron correlation calculations. It is shown that the many-body decomposition of the electron correlation converges very fast, allowing the achievement of excellent agreement with experimental data even when limiting correlation energy contributions to two-body terms only. The incremental method is utilized by a computer program that combines the periodic and localized calculations, and allows for structural optimization of the system of interest.

The adsorption of water molecules on the surface of ice is studied using DFT. Adsorption is found to be favoured on non-crystallographic adsorption sites, and a slight tendency towards the formation of rough surfaces is reported. The localization of excess electrons at the surface of ice is facilitated by co-adsorbed water molecules. For a correct theoretical description of the latter, a self-interaction correction scheme for the excess electron has to be used. However, it is sufficient to limit the self-interaction correction to the excess electron only, since the neutral ice surface itself is well described within conventional DFT. The self-interaction correction scheme is incorporated into a commonly used DFT program package.

Optical excitations of crystalline ice are calculated using many-body perturbation theory. Solving the two-particle Bethe-Salpeter equation yields optical spectra in excellent agreement with experimental data. Based on this agreement, an embedding model is developed that reduces the hydrogen bond network to its most important contribution. The model is applied to crystalline ice, where it reproduces the experimental spectral features, and to microscopic liquid water structures obtained from molecular dynamics simulations, where it reproduces the energy shift of the first absorption peak and gives overall good agreement with experiment. The driving force of water's anomalous optical behaviour is identified.

Acknowledgments

First and foremost I wish to thank my supervisor, Professor Peter Schwerdtfeger. His permanent support, many useful discussions, and his ability to set me on the right track have made this work possible.

I wish to thank the former and current members of the Schwerdtfeger group at Massey University for help, discussions, and distractions offered at various stages of this work. In quasi chronological order Robert, Matthias, Brian, Behnam, Christian, Susan, Elke, Detlev, and Ralf have always been a pleasure to work with and helped me not to forget my German roots.

My thanks go to the Schmidt group at the University of Paderborn, Germany, for their hospitality and many fruitful discussions. I am especially grateful to Professor Gero Schmidt, who was instrumental in getting this PhD adventure started. I am indebted to Claudia Rödl, Frank Fuchs, and Jürgen Furthmüller of the Bechstedt group at the University of Jena, Germany, for providing me with updated versions of the GW and BSE implementations and useful hints for self-interaction correction modifications in VASP.

I wish to acknowledge the support of Massey University in form of a Doctoral Scholarship and EducationNZ in form of a New Zealand International Doctoral Research Scholarship.

Finally I wish to thank my family who have supported my every choice in life completely and wholeheartedly, and Ishbel who makes my heart sing every day. He whetū koe.

Contents

List of Figures

List of Tables

Water is the driving force of all nature.

Leonardo da Vinci

1 Introduction

It is one of the simplest heteronuclear molecules. It is the material with the largest known number of physical and thermodynamical anomalies. It is one of the most abundant substances on Earth and the most abundant crystalline substance in outer space. It is the most dissolving liquid known. It is the only substance available in all three states of matter under ambient conditions. As far as we know, it is essential for the development of life on our planet. It is suspected to be instrumental in the creation of ozone-destroying free radicals in the upper atmosphere. Water is many things, and it certainly has very interesting properties.

70% of the surface of our planet are covered with water; about 10% of its land mass is covered in ice. 65% of the human body mass is water. US$ 720 million were spent by the North American Space Agency on the Mars Reconnaissance Orbiter spacecraft to search for water on Mars. It is essential for every living organism known to man, yet can lead to lethal intoxication due to osmotic processes. It is the ubiquitous solvent in innumerable chemical and technological applications. Yet despite its omnipresence and fundamental importance, and being the focus of a multitude of experimental

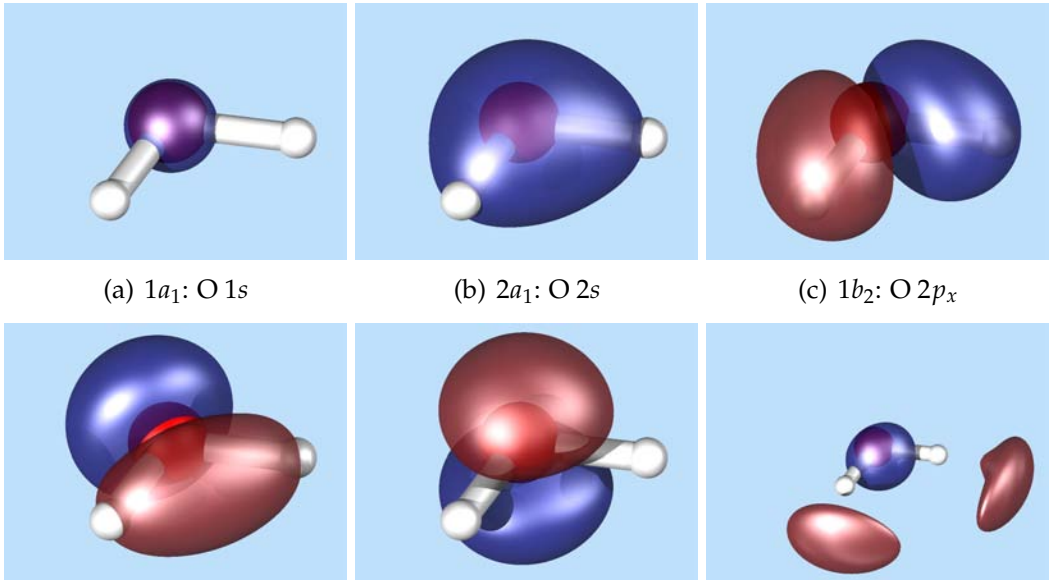

(a) $1a_1$: O $1s$ (b) $2a_1$: O $2s$ (c) $1b_2$: O $2p_x$

(d) $3a_1$: O $2p_y$ (e) $1b_1$: O $2p_z$ (f) $4a_1$: O-H σ^*

Figure 1.1: Isosurfaces of water's molecular orbitals, from Hartree-Fock calculations, including the main atomic orbital contributions. Panels (a)–(e): occupied electronic states; (f) lowest unoccupied electronic state.

and theoretical studies, there are still questions unanswered, and problems unsolved.

The water molecule, as mentioned above, is seemingly very simple: it has C_{2v} symmetry; the mean OH bond length is about 0.957Å [1]; it is bent with a mean HOH angle of about 104.5°, and has a dipole moment of about 1.85 Debye [2]. This corresponds to a partial charge of about -0.7 atomic units at the oxygen atom, and +0.35 atomic units at the hydrogen atoms [3]. These properties can be understood with the illustrative concepts of bond hybridization and atomic electronegativity. However, they also set the stage for the fascinating effects and phenomena that make aggregations of water molecules so unique. The polar character of the water molecule combined with the oxygen lone pairs enables the formation of hydrogen bonds. Their versatility drives the unusual properties of water clusters, liquid water, and solid ice – and, depending on the definition of "unusual", water and ice exhibit about 40 to 60 anomalies in comparison to "normal" liquids and solids.

When freezing, water can crystallize in at least 13 different crystal struc-

tures, depending on pressure and temperature conditions [4]. Experimentally, new phases of ice have been investigated since the start of the twentieth century [5], and even today possible new high pressure phases are reported [6]. The crystalline structures differ with respect to the space group symmetry of the oxygen atoms' lattice, and whether the hydrogen bond network is ordered or not. Disordered hydrogen bonds are usually found at higher temperatures [4]. Locally, all solid phases feature a tetrahedral coordination of water molecules: each molecule donates and accepts two hydrogen bonds. It is beyond these local surroundings that the structures deviate from each other. In addition to the different crystal structures, water can freeze as high density or low density amorphous ice [7,8]. These numerous different solid structures are possible due to the flexibility of the hydrogen bond, as mentioned above.

Standard experimental methods to investigate crystalline phases of water include electron, neutron, and x-ray diffraction. However, their use is limited when the (inherently non-periodic) liquid phase of water is studied: although a short-range order is still approximately kept, the long-range order is lost. These methods can thus yield only averaged structural information, e.g. in the form of radial distribution functions [9]. However, to reveal in more detail the structural and dynamical properties of liquid water, indirect methods such as near-edge x-ray absorption spectroscopy have to be used. Why are these properties of interest? Traditionally, liquid water is seen as a somewhat disordered version of ice: hydrogen bonds are regularly broken and re-formed, and molecules can more or less freely diffuse through the liquid; however, the water molecules are still quasi-tetrahedrally coordinated, with about four nearest neighbours at any given time. This view is supported by virtually all diffraction experiments and theoretical molecular dynamics simulations. Recently, however, this point of view was challenged by ultrafast x-ray absorption measurements in water [10], which found liquid water's spectroscopic fingerprint more closely related to the surface of ice than to bulk ice. According to this research, liquid water molecules would have on average only two nearest neighbours, in crass contrast to the traditional view. This result was listed by Science magazine as one of the scientific "Breakthroughs of the Year" in 2004 [11], and has sparked a flurry of experi-

mental and theoretical investigations. The jury on this matter is still out.

Given this context, theoretical studies on aqueous systems are more important than ever. They provide a means to reproduce experimental findings, establish accurate models of natural systems, and allow for detailed scrutinizing of the phenomena investigated. Parameter-free calculations (here referred to as *ab initio* calculations, or *first principles* calculations) are particularly useful: the ability to describe natural phenomena using a purely microscopic theory of matter, without introduction of empirical parameters, can not be overestimated – it enables us to test the very microscopic theory against nature, while explaining known and predicting new and interesting effects of the systems studied.

The present work aims to investigate extended aqueous systems from *first principles*. It focuses on ground state and excited state properties, and the search for appropriate methodologies to describe these correctly. Chapter 2 introduces the background to the theoretical and computational methodology used. Chapter 3 presents ground state calculations of crystalline ice from a quantum chemical ansatz, combining periodic Hartree-Fock calculations with a localized electron correlation treatment. Using this method, unprecedented accuracy regarding agreement with experimental data is achieved. Chapter 4 contains results of studies of the adsorption of water molecules on the surface of ice. Chapter 5 presents a *first principles* study on the localization of excess electrons at the surface of ice, where a partial self-interaction correction scheme proves crucial. Chapter 6 investigates the optical properties of liquid water and ice. After using Green's function methods to obtain optical spectra of ice in excellent agreement with experiment, a model system is introduced that proves sufficient to reproduce the optical spectrum of ice. The application of this model to liquid water has enabled the first theoretical study that consistently reproduces the energy shifts in the optical spectra of both the liquid and solid phase of water. Chapter 7 contains a summary and conclusions.

There is a mask of theory over the whole face of nature.

William Whewell

A theory must be tempered with reality.

Jawaharlal Nehru

2 Method Review

In this work, a variety of systems are studied computationally that vary in size and dimension from small clusters of molecules, surface systems, to periodic bulk. Thus, different methods have to be employed to correctly describe and calculate the desired properties. This chapter gives a short overview over these methods. For further reading, the reader is referred to standard textbooks on quantum chemistry [12–14], solid state physics [15, 16], and many-body physics [17].

2.1 The Many-Electron Problem

Atoms, molecules, and crystals comprise atomic nuclei and electrons. Correctly describing these systems means including all their mutual interactions. However, considering the problems and properties studied here allows for some major simplifications: the typical length scale is $L \sim 1$Å, and typical velocities are $v \sim \frac{1}{137}c$. Thus, it is convenient to ignore quantum field ($L \gg \lambda_e$, the electron's Compton wave length) and relativistic effects ($v \ll c$, the speed of light), and start from non-relativistic quantum mechanics.

There, a quantum system's wave function $\big|\Phi\big\rangle$ is governed by the Schrödinger equation, which reads in atomic units

$$H_{en}\big|\Phi\big\rangle = i\frac{\partial}{\partial t}\big|\Phi\big\rangle, \tag{2.1}$$

with the Hamiltonian

$$H_{en} = T_n + V_{nn} + T_e + V_{en} + V_{ee}. \tag{2.2}$$

It contains the operators for the nuclear kinetic energy T_n, the nuclear potential energy V_{nn}, the electronic kinetic energy T_e, the electron-nuclear interaction potential V_{en}, and the electronic interaction potential V_{ee}. If the Hamiltonian is not explicitly time-dependent, the time evolution of $\big|\Phi\big\rangle$ can be formulated in terms of the Hamiltonian's eigenfunctions $\big|\Psi_i^{en}\big\rangle$ and corresponding eigenvalues E_i^{en}:

$$\big|\Phi(t)\big\rangle = \sum_i \big\langle\Phi(0)\,\big|\,\Psi_i^{en}\big\rangle e^{-iE_i^{en}t}\big|\Psi_i^{en}\big\rangle, \tag{2.3}$$

$$H_{en}\big|\Psi_i^{en}\big\rangle = E_i^{en}\big|\Psi_i^{en}\big\rangle. \tag{2.4}$$

De-coupling the nuclear degrees of freedom $\{\mathbf{R}_n\}$ and neglecting the coupling between electronic states and nuclear motion (Born-Oppenheimer approximation) separates (2.4) into a nuclear and an electronic part, $H_{en} = H_n + H$ and $\big|\Psi_i^{en}(\mathbf{R}_n)\big\rangle = \psi_i^n(\mathbf{R}_n)\big|\Psi_i\big\rangle$, where

$$H_n\psi_j^n(\mathbf{R}_n) \equiv (T_n + V_{nn})\psi_j^n(\mathbf{R}_n) = E_j^n\psi_j^n(\mathbf{R}_n), \tag{2.5}$$

$$H\big|\Psi_j\big\rangle \equiv (T_e + V_{en} + V_{ee})\big|\Psi_j\big\rangle = E_j(\mathbf{R}_n))\big|\Psi_j\big\rangle. \tag{2.6}$$

The total wave function is expanded into solutions $\big|\Psi_i\big\rangle$ of the electronic Hamiltonian H:

$$\big|\Phi(t)\big\rangle = \sum_j C_j e^{-i(E_j^n + E_j)t}\psi_j^n(\mathbf{R}_n)\big|\Psi_j\big\rangle. \tag{2.7}$$

Solving equation (2.6) to a desired accuracy is a major task of quantum chemistry and theoretical solid state physics. For inhomogeneous systems with

more than one electron, only a few highly symmetric cases allow to solve (2.6) analytically. However, the Rayleigh-Ritz variational principle provides a means to give upper bounds to the system's energy levels E_i by using approximate wave functions $\left|\tilde{\Psi}\right\rangle$: since H is bound from below, it holds

$$\tilde{E} = \frac{\left\langle\tilde{\Psi}\middle|H\middle|\tilde{\Psi}\right\rangle}{\left\langle\tilde{\Psi}\middle|\tilde{\Psi}\right\rangle} \geq \frac{\left\langle\Psi_0\middle|H\middle|\Psi_0\right\rangle}{\left\langle\Psi_0\middle|\Psi_0\right\rangle} = E_0, \tag{2.8}$$

for any trial wave function $\left|\tilde{\Psi}\right\rangle$, where $\left|\Psi_0\right\rangle$ and E_0 denote the electronic ground state and the ground state energy, respectively. For a non-degenerate groundstate $\left|\Psi_0\right\rangle$, the equal sign in (2.8) holds only for $\left|\tilde{\Psi}\right\rangle = \left|\Psi_0\right\rangle$. Excited state energies E_i can be approximated by trial wave functions $\left|\tilde{\Psi}\right\rangle$ that are orthogonal to the subspace spanned by $\{\left|\Psi_j\right\rangle\}_{j<i}$.

Within a parametrized set of trial wave functions $\{\tilde{\Psi}_\nu\}$, the best approximation $\left|\tilde{\Psi}_{\nu^*}\right\rangle$ of the true groundstate wave function is obtained by solving

$$\tilde{\Psi}_{\nu^*} : \nu^* = \min_\nu \left[\left\langle\tilde{\Psi}_\nu\middle|H\middle|\tilde{\Psi}_\nu\right\rangle - \lambda(\left\langle\tilde{\Psi}_\nu\middle|\tilde{\Psi}_\nu\right\rangle - 1)\right]. \tag{2.9}$$

2.2 The Hartree-Fock Method

In second quantization and atomic units, the electronic Hamiltonian reads

$$\begin{aligned} H &= T_e + V_{en} + V_{ee}, && (2.10)\\ T_e &= \sum_\sigma \int d^3\mathbf{r}\, \psi_\sigma^\dagger(\mathbf{r}) \left\{-\frac{1}{2}\nabla^2\right\} \psi_\sigma(\mathbf{r}), && (2.11)\\ V_{en} &= \sum_\sigma \int d^3\mathbf{r}\, \psi_\sigma^\dagger(\mathbf{r}) V(\mathbf{r}) \psi_\sigma(\mathbf{r}), && (2.12)\\ V_{ee} &= \frac{1}{2}\sum_{\sigma,\sigma'} \iint d^3\mathbf{r}\, d^3\mathbf{r}'\, \psi_\sigma^\dagger(\mathbf{r}) \psi_{\sigma'}^\dagger(\mathbf{r}') v(\mathbf{r},\mathbf{r}') \psi_{\sigma'}(\mathbf{r}') \psi_\sigma(\mathbf{r}). && (2.13) \end{aligned}$$

There, we have the electron creation (annihilation) field operators $\psi_\sigma^\dagger(\mathbf{r})$ ($\psi_\sigma(\mathbf{r})$), the external potential $V(\mathbf{r})$, and the Coulombic potential of the interacting electrons,

$$v(\mathbf{r},\mathbf{r}') = \frac{1}{|\mathbf{r}-\mathbf{r}'|}. \tag{2.14}$$

The Hamiltonian also contains sums over the spin degrees of freedom σ. The pair-interaction of the electrons V_{ee} makes the many-electron problem so difficult. Therefore, it would be desirable to map the problem onto a system of non-interacting quasi-particles that do not feel the Coulombic interaction but a suitable effective potential. The wave function $\left|\Psi\right\rangle$ could then be approximated by a product of the quasi-particles' spin orbitals:

$$\Psi(\mathbf{r}) = \left\langle \mathbf{r} \middle| \Psi \right\rangle = \prod_{i=1}^{N} \phi_i(\mathbf{r}_i, \sigma_i) \tag{2.15}$$

Demanding that the approximate wave function fulfills Pauli's exclusion principle leads to the complete antisymmetric sum of the product wave function:

$$\Psi(\mathbf{r}) = \frac{1}{\sqrt{N!}} \sum_{\pi \in \wp(N)} (-1)^{|\pi|} \prod_{i=1}^{N} \phi_{\pi(i)}(\mathbf{r}_i, \sigma_i) \tag{2.16}$$

There, $\wp(N)$ denotes the permutation group of rank N. Introduced independently by Fock [18] and Slater [19], this ansatz for the electronic wave function is also known as a *Slater determinant* (SD):

$$\Psi(\mathbf{r}) = \frac{1}{\sqrt{N!}} \begin{vmatrix} \phi_1(\mathbf{r}_1, \sigma_1) & \phi_2(\mathbf{r}_1, \sigma_1) & \cdots & \phi_N(\mathbf{r}_1, \sigma_1) \\ \phi_1(\mathbf{r}_2, \sigma_2) & \phi_2(\mathbf{r}_2, \sigma_2) & \cdots & \phi_N(\mathbf{r}_2, \sigma_2) \\ \vdots & \vdots & \ddots & \vdots \\ \phi_1(\mathbf{r}_N, \sigma_N) & \phi_2(\mathbf{r}_N, \sigma_N) & \cdots & \phi_N(\mathbf{r}_N, \sigma_N) \end{vmatrix} \tag{2.17}$$

Using all possible SD's (by varying the atomic orbitals ϕ_i) as the set of trial wave functions in (2.9) leads to the well-known *Hartree-Fock equations* for the ϕ_i:

$$H_{\mathrm{HF}} |\phi_i\rangle = \left[h + \sum_{j=1}^{N} (J_j - K_j) \right] |\phi_i\rangle = \varepsilon_i |\phi_i\rangle, \tag{2.18}$$

$$h = -\frac{1}{2}\nabla^2 + V_{en}, \tag{2.19}$$

$$J_j |\phi_i\rangle = \langle \phi_j | v | \phi_j \rangle | \phi_i \rangle, \tag{2.20}$$

$$K_j |\phi_i\rangle = \langle \phi_j | v | \phi_i \rangle | \phi_j \rangle. \tag{2.21}$$

The total energy of the electronic system is given by

$$E = \sum_{i=1}^{N} \langle \phi_i | h | \phi_i \rangle + \frac{1}{2} \sum_{i,j=1}^{N} \left(\langle \phi_i | J_j | \phi_i \rangle - \langle \phi_i | K_j | \phi_i \rangle \right) \tag{2.22}$$

$$= \sum_{i=1}^{N} \varepsilon_i - \frac{1}{2} \sum_{i,j=1}^{N} \left(\langle \phi_i | J_j | \phi_i \rangle - \langle \phi_i | K_j | \phi_i \rangle \right) . \tag{2.23}$$

The operators J_j and K_j represent the mean-field Coulombic interaction (also known as the Hartree term) and the exchange interaction (also known as the Fock term) between electrons i and j. The latter stems from the antisymmetric character of the wave functions and has no classical analogue. That the total energy (2.23) is not equal to the sum of the eigenvalues ε_i illustrates the quasi-particle character of the Hartree-Fock orbitals ϕ_i. The exchange operator K acts only on electrons of the same spin orientation, since v in (2.21) is spin-independent.

2.3 Electron Correlation

In the Hartree-Fock (HF) method, electrons are treated as independent particles obeying the Pauli exclusion principle. They interact based on the *average* position of the other electrons, where in fact their motion is governed by the *actual* position of the other electrons. Electrons of opposite spins, that do not feel the exchange repulsion, can come arbitrarily close to each other in the HF approximation. Displaying the pair distribution function of the homogeneous electron gas visualizes this problem. The pair distribution function $g(\mathbf{r}, \mathbf{r}')$ corresponds to the probability to find an electron at position $\mathbf{r}'$ *provided* an electron is located at position $\mathbf{r}$. In the homogeneous case, $g(\mathbf{r}, \mathbf{r}')$ reduces to $g(r) = g(|\mathbf{r} - \mathbf{r}'|)$. Figure 2.1 shows $g(r)$ for the homogeneous electron gas, obtained from various numerical approaches. In the Hartree approximation, where the wave function takes the product form (2.15) which corresponds to neglecting the exchange operator K_i from (2.21) it holds $g(r) = 1$: having an electron at $\mathbf{r}$ does not influence the probability of having another electron at any other point $\mathbf{r}'$. In the HF approximation, an "exchange hole" is created around the electron at $\mathbf{r}$, illustrating the repul-

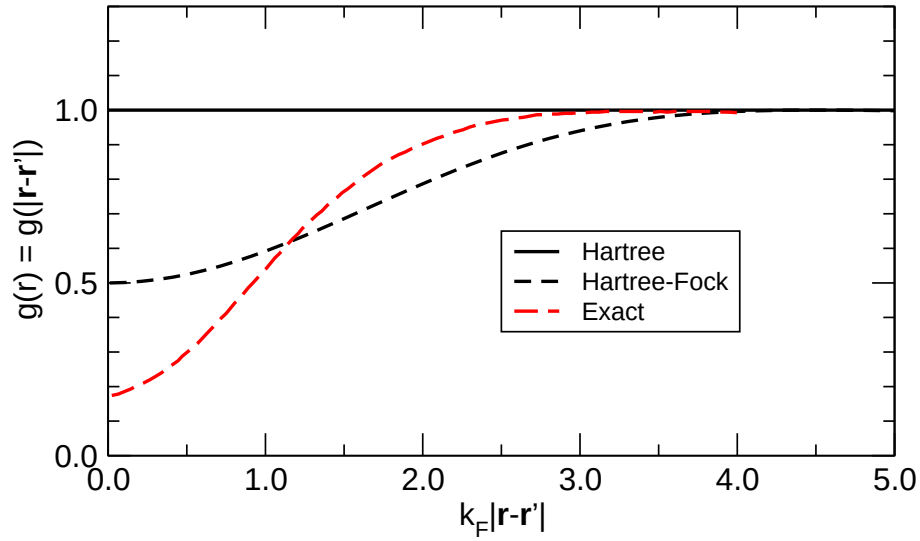

Figure 2.1: Pair-distribution function $g(\mathbf{r}, \mathbf{r}') = g(|\mathbf{r} - \mathbf{r}'|)$ for the homogeneous electron gas, from various numerical approximations. k_F denotes the Fermi wave vector.

sion of electrons of equal spin; $g(0) = 0.5$ in the HF approximation. In reality, however, Coulombic repulsion creates an "exchange-correlation hole" around the electron at $\mathbf{r} = 0$ that is deeper and more localized than in the HF approximation.

In electronic structure theory, "electron correlation" coins the sum of all interactions beyond the Hartree and Fock terms, that is, the difference between the HF approximation and the exact Hamiltonian. The following sections present several methods that treat electronic correlation, based on the HF wave function as a starting guess for the electronic structure.

2.3.1 Many-body perturbation theory

An intuitive way to include electron correlation is to treat the difference between HF and the exact Hamiltonian perturbatively:

$$H = H_{\mathrm{HF}} + \lambda V, \tag{2.24}$$

$$V = V_{ee} - \sum_{i=1}^{N} (J_i - K_i). \tag{2.25}$$

This many-body perturbation theory (MBPT) is also known as Møller-Plesset theory [20]. A power expansion of the electronic wave function and energies with respect to the coupling constant λ,

$$\left|\Psi\right\rangle = \left|\Psi_{\mathrm{HF}}\right\rangle + \lambda\left|\tilde{\Psi}^{(1)}\right\rangle + \lambda^2\left|\tilde{\Psi}^{(2)}\right\rangle + \cdots, \tag{2.26}$$

$$E = E_0 + \lambda E_1 + \lambda^2 E_2 + \cdots, \tag{2.27}$$

leads to

$$E_0 = \left\langle\Psi_{\mathrm{HF}}\right|H_{\mathrm{HF}}\left|\Psi_{\mathrm{HF}}\right\rangle = \sum_{i=1}^{N}\varepsilon_i, \tag{2.28}$$

$$E_1 = \left\langle\Psi_{\mathrm{HF}}\right|V\left|\Psi_{\mathrm{HF}}\right\rangle = -\frac{1}{2}\sum_{i,j=1}^{N}\left(\left\langle\phi_i\right|J_j\left|\phi_i\right\rangle - \left\langle\phi_i\right|K_j\left|\phi_i\right\rangle\right), \tag{2.29}$$

$$E_2 = \left\langle\Psi_{\mathrm{HF}}\right|V\left|\tilde{\Psi}^{(1)}\right\rangle = \frac{1}{4}\sum_{i,j}^{occ}\sum_{r,s}^{vir}\frac{\left|\left\langle\Psi_{\mathrm{HF}}\right|V\left|\Psi_{ij}^{rs}\right\rangle\right|^2}{E_0 - E_{ij}^{rs}}. \tag{2.30}$$

There, $\left|\Psi_{ij}^{rs}\right\rangle = a_s^\dagger a_r^\dagger a_j a_i\left|\Psi_{\mathrm{HF}}\right\rangle$ is a doubly excited HF state, where electrons from the orbitals $\left|\phi_i\right\rangle$, $\left|\phi_j\right\rangle$ are excited to the virtual states $\left|\phi_r\right\rangle$, $\left|\phi_s\right\rangle$. Here, $a_i^\dagger$ (a_i) denote electron creation (annihilation) operators that increase (decrease) the occupation number of orbital $\left|\phi_i\right\rangle$ by 1. The sums in (2.30) sum over all occupied and virtual states, respectively. Note that $E_{\mathrm{HF}} = E_0 + E_1$, and thus the *second* order MBPT gives the first energy correction E_2 beyond HF. This level of correlation treatment (known as MBPT2 or MP2) is a common method to improve the HF energy E_{HF}. Higher order corrections (MPn) are possible, but computation time scales like $\mathcal{O}(N^{n+3})$. As is the nature of perturbation theory, its efficiency depends on the size of the perturbation or, in other words, the usefulness of the unperturbed Hamiltonian. If HF is not suitable to describe the electronic system correctly, higher order perturbation theory may be needed, in which case it can be more efficient to use other correlation methods. Further, if the energy difference in the denominator of (2.30) becomes small, the expansion (2.27) may not converge. This is a fundamental problem in the treatment of electron correlation effects in metallic systems.

2.3.2 Configuration Interaction

The HF method yields by construction the best single-determinant approximation to the electronic wave function. Extending $\left|\Psi_{\mathrm{HF}}\right\rangle$ to a multi-determinant wave function seems to be a natural way to improve the description of an electronic system. In the configuration interaction (CI) approach, more determinants are constructed by exciting electrons to virtual orbitals, that span (with variable coefficients c_i) the total wave function [21–23]:

$$\left|\Psi_{\mathrm{CI}}\right\rangle = \left|\Psi_{\mathrm{HF}}\right\rangle + \sum_{a}^{occ}\sum_{r}^{vir} c_a^r \left|\Psi_a^r\right\rangle + \sum_{a,b}^{occ}\sum_{r,s}^{vir} c_{ab}^{rs}\left|\Psi_{ab}^{rs}\right\rangle + \cdots \tag{2.31}$$

$$= \left|\Psi_{\mathrm{HF}}\right\rangle + \sum_{S} c_S \left|\Psi_S\right\rangle + \sum_{D} c_D \left|\Psi_D\right\rangle + \sum_{T} c_T \left|\Psi_T\right\rangle + \cdots . \tag{2.32}$$

There, S (D, T) sums over all single (double, triple) excitations of the HF wave function. The groundstate energy is obtained by minimization with respect to the coefficient set $\{c_i\}$:

$$E_{\mathrm{CI}} = \min_{\{c_i\}} \frac{\left\langle \Psi_{\mathrm{CI}}\middle|H\middle|\Psi_{\mathrm{CI}}\right\rangle}{\left\langle \Psi_{\mathrm{CI}}\middle|\Psi_{\mathrm{CI}}\right\rangle}. \tag{2.33}$$

That means solving the secular equation

$$H^{\mathrm{CI}}\mathbf{c} = E_{\mathrm{CI}}\mathbf{c}, \tag{2.34}$$

where $H_{ij}^{\mathrm{CI}} = \left\langle \Psi_i\middle|H\middle|\Psi_j\right\rangle$. Note that all orbitals are frozen at the HF level of theory, and only the determinants' coefficients are optimized. The lowest eigenvalue $E_{CI,0}$ is the electronic groundstate energy, and the groundstate is determined by the corresponding eigenvector $\mathbf{c}_0$. The second lowest eigenvalue $E_{CI,1}$ and its eigenvector $\mathbf{c}_1$ correspond to the first excited electronic state etc.

A *full CI* calculation includes all possible excitations into all virtual orbitals – the number of which in an actual calculation equals the number of linearly independent basis functions. Since the number of determinants grows exponentially with the number of orbitals, these calculations are prohibitively large for all but the smallest molecular systems. Usually, the excitation expansion is truncated at some level. Common *truncated CI* methods use the

excited state determinants up to double (CISD) or triple (CISDT) excitations.

The truncated CI method suffers from two major shortcomings. The first is the lack of size-extensivity. That is, treating two electronic systems as non-interacting fragments of the same compound will generally not equal the sum of the individual energies of the two systems. If, for instance, two fragments are calculated on CISD level of theory, a consistent treatment of the compound system should include certain triple and quadruple excitations; namely, those that are products of the fragments' single and double excitations. Thus, a CISD compound calculation will give a *higher* energy than the sum of the fragments' energies. Secondly, the only consistent way to truncate CI is by the number of excitations of the HF state, i.e. after including *all* single, double, or triple excitations. That means that often a very large number of (not particularly important) determinants has to be considered; the convergence of the total energy with respect to the size of the wave function is thus rather slow.

2.3.3 Coupled Cluster Theory

The coupled cluster (CC) theory, developed in the field of nuclear physics [24,25] and adapted later for use in atomic and molecular calculations [26,27], aims to overcome the above mentioned shortcomings of CI. In a CC expansion, the single determinant wave function is expanded by incorporating excitations of a given type (single, double, etc.) to infinite order in a product wave function ansatz, with variable coefficients t_i:

$$\left|\Psi_{\mathrm{CC}}\right\rangle = \left[\prod_{a,r}(1 + t_a^r a_r^\dagger a_a)\right]\left[\prod_{ab,rs}(1 + t_{ab}^{rs} a_s^\dagger a_r^\dagger a_b a_a)\right]\cdots\left|\Psi_{\mathrm{HF}}\right\rangle \tag{2.35}$$

A full CC expansion, including up to N-tuple excitations, gives the same wave function as a full CI expansion. However, due to the product ansatz even truncated CC wave functions are inherently size extensive. Since $(a_r^\dagger a_a)^2 = 0$, it holds

$$(1 + t_a^r a_r^\dagger a_a) = \sum_{k=0}^{\infty}\frac{1}{k!}(t_a^r a_r^\dagger a_a)^k = \exp t_a^r a_r^\dagger a_a, \tag{2.36}$$

and the full CC wave function (2.35) can be rewritten in an exponential form as

$$\big|\Psi_{\mathrm{CC}}\big\rangle = \exp T \big|\Psi_{\mathrm{HF}}\big\rangle \tag{2.37}$$

$$T = T_1 + T_2 + \cdots + T_N, \tag{2.38}$$

where T_i denotes the sum over all possible excitations of i electrons:

$$T_1 = \sum_{a,r} t_a^r a_r^\dagger a_a, \tag{2.39}$$

$$T_2 = \sum_{ab,rs} t_{ab}^{rs} a_s^\dagger a_r^\dagger a_b a_a, \ldots \tag{2.40}$$

The exponential operator $\exp T$ then reads, re-ordered by the number of excitations,

$$\exp T = e^T = 1 + T_1 + \left(T_2 + \frac{1}{2}T_1^2\right) + \left(T_3 + T_2T_1 + \frac{1}{3!}T_1^3\right) + \cdots . \tag{2.41}$$

The CC wave function fulfills a Schrödinger equation for the electronic Hamiltonian H,

$$H\big|\Psi_{\mathrm{CC}}\big\rangle = E_{\mathrm{CC}}\big|\Psi_{\mathrm{CC}}\big\rangle. \tag{2.42}$$

The coefficients (or "amplitudes") of the excitation operators (t_a^r, t_{ab}^{rs}, and so on) are to be optimized. However, unlike in the previously discussed methods, the CC ansatz does not allow for the use of the variational principle. The variational minimum conditions for the excitation amplitudes $t_{ab\ldots}^{rs\cdots}$,

$$\big\langle \Psi_{ab\ldots}^{rs\cdots} \big| e^T H \big| \Psi_{\mathrm{CC}} \big\rangle = E_{\mathrm{CC}} \big\langle \Psi_{ab\ldots}^{rs\cdots} \big| e^T \Psi_{\mathrm{HF}} \big\rangle \tag{2.43}$$

lead to highly nonlinear equations coupling *all* CC amplitudes (which in general contain non-physical solutions). Solving these equations is not possible for all but the smallest molecular systems. Instead, (2.42) is usually written as a projected Schrödinger equation, with an effective non-hermitian Hamiltonian H^T acting on the HF state:

$$e^{-T} H e^T \big|\Psi_{\mathrm{HF}}\big\rangle \equiv H^T \big|\Psi_{\mathrm{HF}}\big\rangle = E_{\mathrm{CC}}\big|\Psi_{\mathrm{HF}}\big\rangle. \tag{2.44}$$

Projection onto $\left|\Psi_{\mathrm{HF}}\right\rangle$ and all excited states $\left|\Psi_{ab\ldots}^{rs\cdots}\right\rangle$ that are obtained by the excitation operators in T yields the *linked coupled cluster equations* for the energy E_{CC} and the amplitudes $t_{ab\ldots}^{rs\cdots}$:

$$\left\langle\Psi_{\mathrm{HF}}\right|e^{-T}He^{T}\left|\Psi_{\mathrm{HF}}\right\rangle = E_{\mathrm{CC}}, \tag{2.45}$$

$$\left\langle\Psi_{ab\ldots}^{rs\cdots}\right|e^{-T}He^{T}\left|\Psi_{\mathrm{HF}}\right\rangle = 0. \tag{2.46}$$

Equations (2.46) are much easier to handle than (2.43): combining the nature of T, comprising sums of commutating excitation operators, with the fact that H contains only one- and two-electron operators means a Baker-Campbell-Hausdorff expansion of the similarity-transformed Hamiltonian H^T vanishes identically after the fourth term:

$$\begin{aligned} H^T = e^{-T}He^{T} =& H + [H,T] + \frac{1}{2}[[H,T],T] + \frac{1}{3!}[[[H,T],T],T] \\ &+ \frac{1}{4!}[[[[H,T],T],T],T]. \end{aligned} \tag{2.47}$$

Thus, equations (2.46) contain the coupled cluster amplitudes *at most* to fourth order; amplitudes of the highest excitations appear only linearly.

The property of H to include only up to two-electron operators also greatly simplifies the energy expression (2.45):

$$E_{\mathrm{CC}} = \left\langle\Psi_{\mathrm{HF}}\right|H^{T}\left|\Psi_{\mathrm{HF}}\right\rangle = \left\langle\Psi_{\mathrm{HF}}\right|H(1 + T_1 + T_2 + \frac{1}{2}T_1^2)\left|\Psi_{\mathrm{HF}}\right\rangle \tag{2.48}$$

$$= E_{\mathrm{HF}} + \sum_{a,r} t_a^r \left\langle\Psi_{\mathrm{HF}}\right|H\left|\Psi_a^r\right\rangle + \frac{1}{4}\sum_{ab,rs}(t_{ab}^{rs} + t_a^r t_b^s - t_a^s t_b^r)\left\langle\Psi_{\mathrm{HF}}\right|H\left|\Psi_{ab}^{rs}\right\rangle. \tag{2.49}$$

While the energy E_{CC} is completely determined by the single and double excitation amplitudes alone, these in turn depend through (2.46) on all higher amplitudes included in the CC calculation.

For practical calculations, the CC expansion has to be truncated. A common choice is restricting T to single and double excitations, $T = T_1 + T_2$, the CCSD approximation, which scales like $\mathcal{O}(N^6)$. Including triple excitations, $T = T_1 + T_2 + T_3$, results in the CCSDT approximation ($\mathcal{O}(N^8)$). Because the latter is not feasible beyond the smallest of molecular systems, a perturba-

tive treatment of the triple excitations on top of CCSD calculations is often dubbed the "gold standard" of single reference calculations: the CCSD(T) approximation, scaling like $\mathcal{O}(N^7)$.

Symmetry adapted cluster expansion

For totally symmetric spin singlet states the CC expansion is a very good and successful method. For open-shell systems, however, the excitation operators can create a CC wave function of mixed symmetry. While the amplitudes of the incorrect symmetry excitations will vanish identically, they still increase the number of variables and thus the complexity of the CC equations (2.46). An elegant way to expand the HF wave function in this case is using *symmetry adapted* cluster operators (SAC), that yield only the desired number of independent variables [28, 29]:

$$\left|\Psi_{\mathrm{SAC}}\right\rangle = \mathcal{P}e^{S}\left|\Psi_{\mathrm{HF}}\right\rangle \tag{2.50}$$

$$S = S_1 + S_2 + \cdots + T_N \tag{2.51}$$

where $\mathcal{P}$ is a symmetry projection operator and S_i denotes the sum over all symmetry-adapted excitations of i electrons:

$$S_1 = \sum_{\tau_1}^{f_1} \sum_{a,r} C^{r}_{\tau_1,a} S^{\dagger}_{\tau_1,a,r} \tag{2.52}$$

$$S_2 = \sum_{\tau_2}^{f_2} \sum_{ab,rs} C^{rs}_{\tau_2,ab} S^{\dagger}_{\tau_2,ab,rs} \cdots . \tag{2.53}$$

The sum over τ_i runs over all symmetry functions of interest. Defined in that way, $\left|\Psi_{\mathrm{SAC}}\right\rangle$ contains only determinants of the desired symmetry.

The resulting SAC equations are similar to the conventional CC equations (2.46) and are solved for the amplitudes $C^{rs\cdots}_{\tau_i,ab\ldots}$.

Excited states, SAC-CI

The SAC expansion also serves as a good starting point for excited state calculations: the SAC wave function $\left|\Psi_{\mathrm{SAC}}\right\rangle$ can be used as input for a conventional CI expansion, in what is known as the SAC-CI method [30, 31]. It is

based on the fact that the set of functions $\{|\Psi_K\rangle\}$ defined by

$$|\Psi_K\rangle = \left(1 - |\Psi_{\text{SAC}}\rangle\langle\Psi_{\text{SAC}}|\right) \mathcal{S}e^S R_K^\dagger |\Psi_{\text{HF}}\rangle \tag{2.54}$$

forms a basis for the excited states:

$$\langle\Psi_K|\Psi_{\text{SAC}}\rangle = 0 \tag{2.55}$$

$$\langle\Psi_K|H|\Psi_{\text{SAC}}\rangle = 0. \tag{2.56}$$

The operator $R_K^\dagger$ denotes an electronic excitation of some kind. Expanding an excited state $|\Psi_e\rangle$ in the basis (2.54) gives

$$|\Psi_e\rangle = \sum_K a_K \left[R_K^\dagger + \sum_i C_i S_i^\dagger R_K^\dagger\right] |\Psi_{\text{HF}}\rangle - \sum_K a_K \langle\Psi_{\text{SAC}}|R_K^\dagger|\Psi_{\text{SAC}}\rangle|\Psi_{\text{SAC}}\rangle. \tag{2.57}$$

The coefficients a_K are obtained from solving the secular equation

$$H^{\text{SAC-CI}}\mathbf{a} = E_{\text{SAC-CI}}\mathbf{a}, \tag{2.58}$$

where $H_{IJ}^{\text{SAC-CI}} = \langle\Psi_I|H|\Psi_J\rangle$. The lowest eigenvalue $E_{\text{SAC-CI}}^0$ (and its eigenvector $\mathbf{a}_0$) correspond to the first excited state of the chosen symmetry, $E_{\text{SAC-CI}}^1$ and $\mathbf{a}_1$ to the second excited state, and so on.

2.4 Density Functional Theory

The Hartree-Fock method has proven a valuable tool in atomic and molecular calculations, if only to serve as a starting point for the correlation methods discussed in section 2.3. To treat crystalline materials, it can be extended to describe systems with periodic boundary conditions; however, due to the non-local character of the exchange operator (2.21) these calculations are rather time-consuming, and a more efficient method is needed. Density functional theory is this method.

Hohenberg and Kohn [32] identified the *electronic density* $n(\mathbf{r})$ of the ground state as a central quantity that uniquely determines the ground state and (except for a constant) the external potential V_{en}. Thus, the ground state

energy E_0 is a functional of the ground state density:

$$E_0 = E_0[n] = F_0[n] + \int d^3\mathbf{r}\, V_{en}(\mathbf{r})n(\mathbf{r}),\ F_0[n] = \langle \Psi_0 | T_e + V_{ee} | \Psi_0 \rangle. \quad (2.59)$$

The functional $F_0[n]$ is universal, independent of the external potential.

Since $E_0[n]$ reaches its minimum at the actual ground state density associated with V_{en}, a variational principle can be set up:

$$E_0 = \min_{\tilde{n}} E_0[\tilde{n}]. \quad (2.60)$$

To exploit the minimum property of $E_0[n]$, Kohn and Sham devised a scheme to map the many-electron system to a system of non-interacting quasiparticles in an effective potential such that it has the *same* ground state density $n(\mathbf{r})$ as the interacting system [33]. Writing the wave function of the non-interacting system as a SD with single-particle orbitals $\{\phi_i\}$, the ground state energy and electron density are

$$n(\mathbf{r}) = \sum_{i=1}^{N} |\langle \mathbf{r} | \phi_i \rangle|^2, \quad (2.61)$$

$$E = F_0[n] + \sum_{i=1}^{N} \langle \phi_i | V_{en} | \phi_i \rangle, \quad (2.62)$$

$$F_0[n] = \sum_{i=1}^{N} \langle \phi_i | -\frac{1}{2}\nabla^2 | \phi_i \rangle + E_H[n] + E_{xc}[n], \quad (2.63)$$

All electron interaction contributions beyond the Hartree energy E_H are included in the *exchange-correlation energy* functional $E_{xc}[n]$, which is unknown. The variational principle (2.60) leads to the *Kohn-Sham equations* for the orbitals $|\phi_i\rangle$:

$$H_{\mathrm{KS}} |\phi_i\rangle = \left[-\frac{1}{2}\nabla^2 + V_{en} + V_H[n] + V_{xc}[n] \right] |\phi_i\rangle = \varepsilon_i |\phi_i\rangle. \quad (2.64)$$

$$V_H(\mathbf{r}) = \frac{\delta E_H}{\delta n(\mathbf{r})} = \int d^3\mathbf{r}'\, n(\mathbf{r}')v(\mathbf{r}, \mathbf{r}') \quad (2.65)$$

$$V_{xc}(\mathbf{r}) = \frac{\delta E_{xc}}{\delta n(\mathbf{r})}. \quad (2.66)$$

Like the HF equations, the Kohn-Sham equations have to be solved iteratively, since the orbitals $|\phi_i\rangle$ determine via the density $n(\mathbf{r})$ from (2.61) the Kohn-Sham Hamiltonian H_{KS}. Also, like in HF theory, the quasi-particle character of the non-interacting system is illustrated in the total energy, which is not equal to the sum of the Hamiltonian's eigenvalues ε_i:

$$E = \sum_{i=1}^{N} \varepsilon_i - E_H[n] + E_{xc}[n] - \int d^3\mathbf{r}\, V_{xc}(\mathbf{r}) n(\mathbf{r}). \tag{2.67}$$

In principle, solving the Kohn-Sham equations gives the correct electronic ground state electron density and energy. However, the unknown exchange-correlation functional $E_{xc}[n]$ has to be approximated in practical applications, and all currently available approximations suffer from such shortcomings that limit the applicability of DFT.

2.4.1 Approximations to the exchange-correlation energy

The exchange-correlation energy $E_{xc}[n]$ contains all electron-electron interactions beyond the Hartree energy as a functional of the electronic ground state density; more precisely, it also contains the self-interaction correction to the Hartree term and the difference between the kinetic energy $\langle\Psi|T_e|\Psi\rangle$ and its non-interacting counterpart, $\sum_i \langle\phi_i| - \frac{1}{2}\nabla^2|\phi_i\rangle$.

The Local Density Approximation

Basically all approximations to $E_{xc}[n]$ start from the homogeneous electron gas (which itself is a good approximation for valence electrons in metals). In the *local density approximation* (LDA), $E_{xc}[n]$ integrates over local contributions from the homogeneous electron gas' exchange-correlation energy density $\epsilon_{xc}^{hom}(n)$:

$$E_{xc}^{\mathrm{LDA}}[n] = \int d^3\mathbf{r}\, n(\mathbf{r}) \epsilon_{xc}^{hom}(n)\big|_{n(\mathbf{r})}. \tag{2.68}$$

The exchange-correlation potential $V_{xc}(\mathbf{r})$ in (2.64) is then given by

$$V_{xc}^{\mathrm{LDA}}[n](\mathbf{r}) = \epsilon_{xc}^{hom}(n)\big|_{n(\mathbf{r})} + n(\mathbf{r}) \frac{\partial}{\partial n} \epsilon_{xc}^{hom}(n)\big|_{n(\mathbf{r})}. \tag{2.69}$$

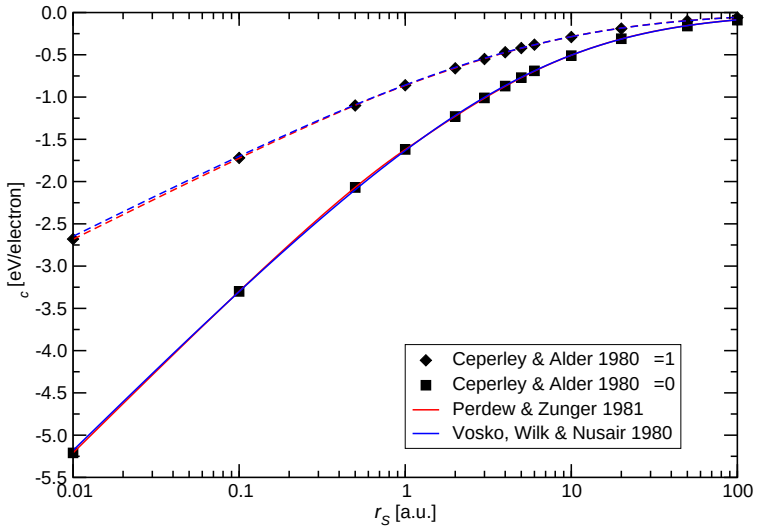

Figure 2.2: Homogeneous electron gas correlation energy density, plotted vs. Wigner radius $r_S = (\frac{3}{4}\pi n)^{-1/3}$, from QMC calculations [34], and most common fits [35,36].

The homogeneous electron gas was subject to extensive theoretical studies [37,38]. Its exchange energy density can be written out analytically,

$$\epsilon_x(n,\zeta) = -\frac{3}{4\pi}\left(3\pi^2 n\right)^{\frac{1}{3}} f(\zeta),\ f(\zeta) = \frac{1}{2}\left[(1+\zeta)^{4/3} + (1-\zeta)^{4/3}\right], \quad (2.70)$$

where $\zeta = (n_\alpha - n_\beta)/n$ is the relative spin polarization of the electron gas. The remaining correlation energy density $\epsilon_c(n) = \epsilon_{xc}(n) - \epsilon_x(n)$ can be calculated to high accuracy using quantum Monte Carlo methods (QMC) [34]. Subsequent fits of $\epsilon_c(n)$ by Perdew and Zunger [35] or Vosko *et al.* [36] complete the construction of $E_{xc}^{\mathrm{LDA}}[n]$, see Figure 2.2.

Despite being a rather crude approximation, the LDA has been applied successfully to calculate ground state energies, lattice constants, and phonon frequencies of various materials, especially for metallic systems; most of which deviate strongly from the originating homogeneous electron gas, or even a slowly varying electron density. Several reasons for that can be identified: the LDA often gives a good approximation of the sperical average of the exchange-correlation hole; it also fulfills the sum rule that the charge of the exchange-correlation hole be exactly -1. However, LDA has many short-

comings, one of which is a notorious under-estimation of the band gap of semiconductors or insulators, of up to 100%.

Generalized Gradient Approximations

An obvious extension to LDA is the consideration of density gradient information in the exchange-correlation kernel:

$$E_{xc}[n] = \int d^3\mathbf{r}\, n(\mathbf{r})\epsilon_{xc}(n, \nabla n)\big|_{n(\mathbf{r})}. \tag{2.71}$$

Over the last decades, various of these *generalized gradient approximations* (GGA) have been suggested, and, with varying success, applied to a wide range of materials. Among the most common functionals are PW91 [39, 40] (named after its developers Perdew and Wang) and PBE [41] (named after Perdew, Becke, and Ernzerhof). Both use the following models, depending on the local electron density n and the spin polarization ζ:

$$E_x[n] = \frac{1}{2}\tilde{E}_x[(1+\zeta)n] + \frac{1}{2}\tilde{E}_x[(1-\zeta)n], \tag{2.72}$$

$$\tilde{E}_x[\tilde{n}] = \int d^3\mathbf{r}\, \tilde{n}(\mathbf{r})F(s)\epsilon_x^{hom}(n)\big|_{\tilde{n}(\mathbf{r})}, \quad s \equiv \frac{|\nabla\tilde{n}|}{2\tilde{k}_F\tilde{n}}; \tag{2.73}$$

$$E_c[n] = \int d^3\mathbf{r}\, n(\mathbf{r})\left[\epsilon_c^{hom}(n,\zeta) + H(t, r_S, \zeta)\right], \quad t = \frac{|\nabla n|}{2gk_s n}, \tag{2.74}$$

$$g(\zeta) = \frac{1}{2}\left[(1+\zeta)^{2/3} + (1-\zeta)^{2/3}\right], \quad k_s(n) = \sqrt{\frac{4k_F}{\pi}}. \tag{2.75}$$

The parametrizations use scaled density gradients s and t, the local Fermi wave vector k_F and screening wave vector $k_s = (4k_F/\pi)^{1/2}$, and the local Wigner radius r_S. They differ in the parametrization of the enhancement function $F(s)$ and $H(t, r_S, \zeta)$ (in LDA it holds $F(s) \equiv 1$ and $H \equiv 0$). Both GGAs fulfill the sum rule for the exchange-correlation charge, and over a wide range of materials give better results than LDA: atomic ground state energies and molecular binding energies are improved; hydrogen bonds are decribed better; simple metal lattice constants agree better with experiment; the ground state of iron is predicted correctly. However, the semi-local approach to the exchange-correlation energy of (2.71) still leads to fundamental shortcomings within these (and all) GGAs: no possibility to describe disper-

sion forces; an unphysical asymptotic exponential decay of the electrostatic potential above surfaces; self-interaction of the electrons; no discontinuity in $V_{xc}(\mathbf{r})$ with respect to the electron number N, thus a systematic underestimation of the band gap in semiconductors and insulators [42].

2.4.2 Self-interaction correction schemes

Self-interaction coins the interaction of an electron in orbital $|\phi_i\rangle$ with itself in the Hartree energy term:

$$E_{SI}[n_i] \equiv E_H[n_i] = \int d^3\mathbf{r}\, d^3\mathbf{r}'\, n_i(\mathbf{r}) v(\mathbf{r},\mathbf{r}') n_i(\mathbf{r}'). \tag{2.76}$$

In Hartree-Fock theory, E_{SI} is cancelled exactly by a corresponding term in the exchange energy E_x. The same holds in exact DFT,

$$E_H[n_i] + E_{xc}[n_i] = 0. \tag{2.77}$$

However, in all practical DFT implementations (i.e., in all available exchange-correlation approximations) the identity in (2.77) does not hold.

Since E_{SI} is mediated by the Coulombic potential $v(\mathbf{r},\mathbf{r}')$, the self-interaction is largest for localized orbitals. Several schemes have been proposed to explicitly (yet efficiently) dispose of artificial self-interaction; for instance, an early work by Stoll and co-workers suggested subtracting the correlation energy of electrons with the same spin from the total correlation energy [43].

The Perdew Zunger scheme

Perdew and Zunger suggested to explicitly subtract the term (2.77) from the total energy expression [35]:

$$E_{xc}^{PZ}[n] = E_{xc}[n] - \sum_i \left(E_H[n_i] + E_{xc}[n_i]\right). \tag{2.78}$$

Using E_{xc}^{PZ} in (2.60) leads to an orbital-dependent Hamiltonian:

$$H^{PZ}|\phi_i\rangle = \left[-\frac{1}{2}\nabla^2 + V_{en} + V_H[n] + V_{xc}^{PZ}[n,\phi_i]\right]|\phi_i\rangle = \varepsilon_i|\phi_i\rangle, \tag{2.79}$$

$$V_{xc}^{PZ}(\mathbf{r}) = V_{xc}(\mathbf{r}) - \int d^3\mathbf{r}'\, n_i(\mathbf{r}')v(\mathbf{r},\mathbf{r}') - \frac{\partial E_{xc}}{\partial n_i(\mathbf{r})}. \tag{2.80}$$

Solving (2.79) iteratively is computationally very demanding, and the non-hermicity of the Hamiltonian H^{PZ} requires more attention in the iterative process.

The Mauri scheme

If a $2N+1$ electron system is investigated that contains an excess electron or hole, extra care should be taken to correctly describe the excess charge. If the underlying $2N$ electron system (in case of an excess electron) is well described within DFT, one could restrict the self-interaction correction to the excess charge. Moreover, claiming that the magnetization density $m(\mathbf{r}) = n_\alpha(\mathbf{r}) - n_\beta(\mathbf{r})$ be equal to the excess charge, a new energy functional can be proposed that corrects self-interaction based on the magnetization density [44]:

$$E_{xc}^{M}[n_\alpha, n_\beta] = -E_H[m] + E_{xc}[n_\alpha - m, n_\beta]. \tag{2.81}$$

The Hartree self-interaction of the magnetization density is removed from the total energy expression, and the exchange-correlation energy is calculated only for the $2N$ electron system. Due to $E_H[m]$, this functional tends to maximize $m(\mathbf{r})$ and thus leads to unphysical spatial separation of spins α, β; with the condition $|\phi_{i\alpha}\rangle = |\phi_{i\beta}\rangle = |\phi_i\rangle$ ($i = 1 \ldots N$), however, this is prevented, and the resulting total energy expression reads

$$E = T[n] + E_H[n_\alpha + n_\beta] + E_{xc}^{M}[n_\alpha, n_\beta] + \sum_{ij}\eta_{ij}(\langle\phi_i|\phi_j\rangle - \delta_{ij}). \tag{2.82}$$

This approach is a very efficient method, but only applicable for spin-1/2 systems with an additional electron or hole. Ionic defects in semiconductors can thus be described more accurately. The correction term does not affect the results of the neutral system, in contrast to the Perdew-Zunger approach.

2.5 Green's Function Formalism

Density functional theory is essentially a ground state theory. Wave function based methods such as CI can calculate excited states, but the number of configurations become too large when describing extended systems. In that case, one usually has to resort to time-dependent density functional theory (TDDFT) [45–47], or Green's function techniques. The Green's function formalism is extremely useful to access observables connected with electronic excitations, such as ionization energies, electron affinities, optical transition matrix elements, or dynamic polarizabilities. It is equally applicable to molecular and periodic systems, and allows for systematic improvement of calculated properties by providing a well defined perturbation series. In the following, the theory of Green's functions is presented, with special focus on one-electron excitations and electron-hole interaction in the case of optical excitations. The theory for the latter is based on Hedin's work [48], for reviews see [49–51].

2.5.1 One and two electron Green's functions

In a N-electron system, the one-electron Green's function is defined by

$$G(\mathbf{r}t, \mathbf{r}'t') = \left\langle N \middle| T\{\psi(\mathbf{r}, t)\psi^\dagger(\mathbf{r}', t')\} \middle| N \right\rangle, \tag{2.83}$$

where $\psi^\dagger(\mathbf{r}, t)$ ($\psi(\mathbf{r}', t')$) are the Heisenberg electron creation (annihilation) operators; T creates the time-ordered product of ψ and $\psi^\dagger$. Thus, for $t < t'$, $G(\mathbf{r}t, \mathbf{r}'t')$ describes a $(N-1)$-electron state, where a hole is created at $(\mathbf{r}, t)$ and propagated to $(\mathbf{r}', t')$. For $t > t'$, $G(\mathbf{r}t, \mathbf{r}'t')$ describes the propagation of an extra electron, added to the system at $(\mathbf{r}, t)$, and detected at $(\mathbf{r}', t')$. The one-electron Green's function is suitable to describe one-electron processes like (inverse) photo-electron spectroscopy. In case of a time-independent external potential G depends only on the difference $\tau = t - t'$ between t, t':

$$G(\mathbf{r}, \mathbf{r}', \tau) = G(\mathbf{r}, \mathbf{r}', t - t') = G(\mathbf{r}t, \mathbf{r}'t'). \tag{2.84}$$

Analogously, the two-electron Green's function is defined as

$$G(12,1'2') = \big\langle N\big|T\{\psi(1)\psi(2)\psi^\dagger(1')\psi^\dagger(2')\}\big|N\big\rangle, \tag{2.85}$$

with the abbreviated notation $1 \equiv (\mathbf{r}_1, t_1)$. Depending on the time-ordering, $G(12,1'2')$ describes the probabilities of electron-electron ($t_1, t_2 > t_1', t_2'$), hole-hole ($t_1, t_2 < t_1', t_2'$), or electron-hole ($t_1, t_1' \gtrless t_2, t_2'$) propagation processes. The latter describes optical excitations.

Spectral Representations

In frequency space, G reads

$$G(\mathbf{r},\mathbf{r}',\omega) = \int_{-\infty}^{\infty} d\tau\, G(\mathbf{r},\mathbf{r}',\tau)e^{i\omega\tau} = \int_{-\infty}^{\infty} d\omega'\, \frac{A(\mathbf{r},\mathbf{r}';\omega')}{\omega-\omega'}, \tag{2.86}$$

where the spectral function $A(\mathbf{r},\mathbf{r}';\omega)$ is introduced. If a complete set of H eigenstates of $(N-1)$ and $(N+1)$ electrons is inserted in (2.83), $G(\mathbf{r},\mathbf{r}',\omega)$ can be written in a Lehmann representation with the amplitudes

$$f_s(\mathbf{r}) = \begin{cases} \big\langle N\big|\psi(\mathbf{r})\big|N+1,s\big\rangle, \epsilon_s > \mu \\ \big\langle N-1,s\big|\psi(\mathbf{r})\big|N\big\rangle, \epsilon_s < \mu \end{cases} \tag{2.87}$$

as

$$G(\mathbf{r},\mathbf{r}',\omega) = \sum_s \frac{f_s(\mathbf{r})f_s^*(\mathbf{r}')}{\omega - [\epsilon_s + i\eta\,\mathrm{sgn}(\mu-\epsilon_s)]} \tag{2.88}$$

$$A(\mathbf{r},\mathbf{r}',\omega) = \sum_s f_s(\mathbf{r})f_s(\mathbf{r}')\delta(\omega-\epsilon_s). \tag{2.89}$$

where the chemical potential μ was introduced; s labels the $(N+1)$- and $(N-1)$-electron states; and the positive infinitesimal number η ensures correct analytical properties of G. Thus, poles of G correspond to electron addition or removal energies. For non-interacting particles, all N and $(N\pm1)$ states are Slater determinants, and the poles of G are at the eigenvalues of the respective effective Hamiltonian. For interacting electrons, the state summation in (2.88) will in general yield broad peaks, the finite width of which relates to the lifetime of these quasiparticle excitations.

Equation of motion

From the field operators' equation of motion, $i\dot{\psi} = [\psi, H]$, where H is the electronic Hamiltonian from (2.10), one derives the equation of motion of the one-electron Green's function:

$$\begin{aligned}&\left[i\frac{\partial}{\partial t} + \frac{1}{2}\nabla^2 - V(\mathbf{r})\right] G(\mathbf{r}t, \mathbf{r}'t') \\ &+ i\int d^3\mathbf{r}''\, v(\mathbf{r}, \mathbf{r}'')\big\langle N\big|T\{\psi(\mathbf{r}, t)\psi(\mathbf{r}'', t)\psi^\dagger(\mathbf{r}'', t)\psi^\dagger(\mathbf{r}', t')\}\big|N\big\rangle \\ &= \delta(\mathbf{r} - \mathbf{r}')\delta(t, t').\end{aligned} \tag{2.90}$$

To solve (2.90), one needs to know the two-electron Green's function that appears due to the Coulombic interaction term between the electrons. Similarly to (2.90), an equation of motion could be constructed for the two-electron propagator that in turn contains higher order Green's functions. Alternatively, however, a set of coupled integro-differential equations can be constructed with the electronic self energy operator Σ as central quantity [48].

2.5.2 Electronic Self Energy and Hedin's equations

Rewriting (2.90), the electronic self energy operator Σ is defined by

$$\begin{aligned}&\left[i\frac{\partial}{\partial t} + \frac{1}{2}\nabla^2 - V(\mathbf{r}) - V_H(\mathbf{r})\right] G(\mathbf{r}t, \mathbf{r}'t') \\ &- i\int d^3\mathbf{r}''\, dt''\, \Sigma(\mathbf{r}t, \mathbf{r}''t'')G(\mathbf{r}''t'', \mathbf{r}'t') = \delta(\mathbf{r} - \mathbf{r}')\delta(t, t').\end{aligned} \tag{2.91}$$

There, the Hartree potential $V_H(\mathbf{r})$ is extracted from the Coulomb integral of (2.90). Although only defined implicitly, Σ as introduced in (2.91) is the foundation for an expansion into the screened Coulomb potential W, that allows for accurate calculation of one-electron properties.

In frequency space, (2.91) reads

$$\begin{aligned}&\left[\omega + \frac{1}{2}\nabla^2 - V(\mathbf{r}) - V_H(\mathbf{r})\right] G(\mathbf{r}, \mathbf{r}', \omega) \\ &- \int d^3\mathbf{r}''\, \Sigma(\mathbf{r}, \mathbf{r}''; \omega)G(\mathbf{r}'', \mathbf{r}', \omega) = \delta(\mathbf{r} - \mathbf{r}').\end{aligned} \tag{2.92}$$

Two approximations to Σ are immediately obvious. $\Sigma \equiv 0$ leads to the Hartree approximation; self-energy effects are then completely ignored. $\Sigma(\mathbf{r}t, \mathbf{r}'t') = iv(\mathbf{r}, \mathbf{r}')G(\mathbf{r}t, \mathbf{r}'t')\delta(t, t')$ leads to the Hartree-Fock approximation; the self-energy is approximated to be mediated by the bare Coulomb potential, and in frequency space equals the exchange potential: $\Sigma(\mathbf{r}, \mathbf{r}'; \omega) = -v(\mathbf{r}, \mathbf{r}')\langle N|\psi^\dagger(\mathbf{r}')\psi(\mathbf{r})|N\rangle = V_x(\mathbf{r}, \mathbf{r}')$. Using the bare Coulomb potential is a crude approximation, since screening effects become very important in molecules and periodic systems. An expression of Σ in terms of the screened Coulomb potential W is thus desirable.

In general, let $G_0(\mathbf{r}, \mathbf{r}', \omega)$ be the Green's function of some effective Hamiltonian,

$$\left[\omega + \frac{1}{2}\nabla^2 - V(\mathbf{r}) - V_H(\mathbf{r}) - V_{eff}(\mathbf{r})\right] G_0(\mathbf{r}, \mathbf{r}', \omega) = \delta(\mathbf{r} - \mathbf{r}'), \tag{2.93}$$

then (2.92) can be rewritten as a Dyson equation:

$$G(12) = G_0(12) + \int d34\, G_0(13)\left(\Sigma(34) - V_{eff}(\mathbf{r})\delta(3-4)\right) G(42), \tag{2.94}$$

where the short notation $1 \equiv (\mathbf{r}_1, t_1)$ etc., is re-introduced.

Hedin's equations

Using a generating functional ϕ, a method commonly used in field theory [17, 52], one obtains a central relation between the one-electron Green's function's variational derivative and the two-electron Green's function:

$$\frac{\delta G(12;\phi)}{\delta\phi(3^+)} = G(12;\phi)G(33^+;\phi) - G(13, 23^+;\phi). \tag{2.95}$$

Superscript "+" indicates infinitesimal shift of the time coordinate in the complex plane to ensure convergence. Combining this result with (2.85), and comparing (2.90) and (2.91) gives an explicit expression for Σ:

$$\Sigma(12;\phi) = i\int d34\, v(\mathbf{r}_1, \mathbf{r}_3)\frac{\delta G(14;\phi)}{\delta\phi(3^+)}G^{-1}(42;\phi) \tag{2.96}$$

$$= -i\int d34\, v(\mathbf{r}_1, \mathbf{r}_3)G(14;\phi)\frac{\delta G^{-1}(42;\phi)}{\delta\phi(3^+)}. \tag{2.97}$$

Introducing the screened Coulomb potential W as

$$W(12) = \int d3\, v(\mathbf{r}_1, \mathbf{r}_3)\epsilon^{-1}(32) \tag{2.98}$$

with the inverse of the microscopic dielectric function ϵ,

$$\epsilon(12) = \delta(12) - \int d3\, P(32)v(\mathbf{r}_1, \mathbf{r}_3) \tag{2.99}$$

and the microscopic polarization function P,

$$P(12) = i \int d34\, G(23)G(42)\frac{\delta G^{-1}(42)}{\delta V_H(1)} \tag{2.100}$$

a set of coupled equations, Hedin's equations, can be formulated, that eventually defines Σ:

$$\begin{aligned}
\Sigma(12) &= i \int d34\, W(1^+3)G(14)\Lambda(42;3) && \text{(2.101a)}\\
W(12) &= v(\mathbf{r}_1, \mathbf{r}_2) + \int d34\, W(13)P(34)v(\mathbf{r}_4, \mathbf{r}_2) && \text{(2.101b)}\\
P(12) &= -i \int d34\, G(23)G(42)\Lambda(34;1) && \text{(2.101c)}\\
\Lambda(12;3) &= \delta(12)\delta(13) && \text{(2.101d)}\\
&\quad + \int d4567\, \frac{\delta\Sigma(12)}{\delta G(45)} G(46)G(75)\Lambda(67;3).
\end{aligned}$$

Together with the Dyson equation (2.94), Hedin's equations (2.101) are the foundation for a perturbation series that allow for iterative calculation of G and thus all one-electron properties. Essential are the dynamically screened Coulombic interaction $W(12)$, which in turn is determined by the polarization $P(12)$ that describes the N-electron system's response to the presence of an additional electron or hole. The vertex function $\Lambda(12;3)$ contains the information about the interaction of the screening electrons and holes.

2.5.3 *GW* Approximation

Hedin's equations (2.101) can be treated iteratively to obtain ever improving expressions for the self energy operator Σ. Starting from $\Sigma = 0$, the vertex

function is $\Lambda(12;3) = \delta(12)\delta(13)$. That in turn gives the following set of equations:

$$\Sigma(12) = iG(12)W(1^+2) \tag{2.102a}$$
$$W(12) = v(\mathbf{r}_1, \mathbf{r}_2) + \int d34 W(13)P(34)v(\mathbf{r}_4, \mathbf{r}_2) \tag{2.102b}$$
$$P(12) = -iG(12)G(21) \tag{2.102c}$$

In this so-called GW approximation, Σ is simply the product of the one-electron Green's function G and the screened interaction W. The dynamical screening in W leads to a much better description of self energy effects than the HF approximation, where the unscreened Coulomb potential is used.

The polarization function P is simply the product of an electron and hole propagator – the GW approximation does not go beyond the random phase approximation (RPA), and thus should not be expected to yield high quality absorption spectra.

The iterative procedure works as follows: starting from some Green's function G_0 from a suitable independent particle system, a polarization function $P_0 = -iG_0G_0$ can be calculated; then, the screened interaction $W_0 = \epsilon_0^{-1}v$ is set up, and the self energy operator $\Sigma_0 = G_0W_0$ is calculated; the Dyson equation $G = G_0 + G_0(\Sigma - V_{eff})G$ (2.94) gives an improved Green's function; and so on, until self consistency is reached. In practical calculations, however, this process is often aborted after the first iteration (giving $\Sigma = G_0W_0$) [53, 54]. In fact, striving towards self-consistency in the GW approximation (2.102) often worsens results after the first iteration, due to neglect of vertex corrections [51].

In periodic systems, a common starting point for a GW calculation is DFT. Kohn-Sham wave functions are used to construct G_0 in the form of (2.88). The screened interaction W can be difficult to compute, since the dielectric matrix $\epsilon(12)$ has to be inverted at every frequency ω. Model dielectric functions [55] or the plasmon-pole approximation [56] circumvent this step; the detailed frequency behaviour of $\epsilon(12)$ can be argued to be of little importance, since $W = \epsilon^{-1}v$ contains an integration over all frequencies. Thus, quasi-particle

energies ϵ_i^{QP} and wave functions $|\phi_i^{QP}\rangle$ are obtained by

$$|\phi_i^{QP}\rangle = |\phi_i\rangle, \tag{2.103}$$

$$\epsilon_i^{QP} = \epsilon_i + \langle\phi_i|\Sigma(\epsilon_i^{QP}) - V_{xc}|\phi_i\rangle \tag{2.104}$$

$$\approx \epsilon_i + \langle\phi_i|\Sigma(\epsilon_i) - V_{xc}|\phi_i\rangle \left(1 + \frac{\partial\Sigma}{\partial\epsilon}\bigg|_{\epsilon_i}\right)^{-1}, \tag{2.105}$$

where in the last step Σ was expanded linearly around the KS eigenvalue ϵ_i. The thus obtained eigenvalues ϵ_i^{QP} can be compared directly to photo electron spectroscopy data (for occupied states) or inverse photo electron spectroscopy data (for unoccupied states).

2.5.4 Bethe-Salpeter Equation

Optical excitations are governed by the two-particle polarization function. Closer inspection of Hedin's equations shows that $P(12)$ is in fact a contraction of such a two-particle polarization function:

$$P(12) = P(11^+, 22^+) \tag{2.106}$$

$$P(11', 22') = -iG(12)G(2'1') \tag{2.107}$$

Substituting (2.101d) in (2.101c), and using $\delta\Sigma/\delta G = iW$, one obtains the Bethe-Salpeter equation for the microscopic polarization function, in GW approximation:

$$P(11^+, 22^+) = -iG(12)G(2^+1^+) + i\int d34 G(14)G(31^+)W(34)P(34, 22^+). \tag{2.108}$$

2.5.5 Response Functions

The microscopic dielectric function was introduced in the previous chapter, see (2.99). Its spatial Fourier transform determines the loss function $L(\omega)$, which is measured in electron energy loss spectroscopy (EELS). Photon absorption, however, is related to the *macroscopic* dielectric function $\epsilon_M(\omega)$. For

periodic crystals, it holds [57–59]

$$\epsilon_M(\hat{\mathbf{q}},\omega) = \lim_{\mathbf{q}\to 0} \frac{1}{\epsilon^{-1}_{00}(\mathbf{q},\omega)}, \tag{2.109}$$

with the head element ϵ_{00} of the dielectric matrix $\epsilon_{\mathbf{G}\mathbf{G}'}(\mathbf{q},\omega)$. The contribution of off-diagonal elements of $\epsilon_{\mathbf{G}\mathbf{G}'}$ to ϵ_M are local-field effects, originating from density fluctuations on the microscopic scale. The macroscopic dielectric function can be derived from a macroscopic polarization function $\bar{P}$,

$$\epsilon_M(\hat{\mathbf{q}},\omega) = 1 - \lim_{\mathbf{q}\to 0} v(\mathbf{q})\bar{P}_{00}(\mathbf{q},\omega), \tag{2.110}$$

which in turn fulfills the Dyson equation

$$\bar{P}(12) = P(12) + \int d34 P(13)\bar{v}(\mathbf{r}_3,\mathbf{r}_4)\bar{P}(42), \tag{2.111}$$

$$\bar{v}_{\mathbf{G}}(\mathbf{q}) = \begin{cases} 0 & , \mathbf{G} = 0 \\ v_{\mathbf{G}}(\mathbf{q}), & \mathbf{G} \neq 0 \end{cases} \tag{2.112}$$

$\bar{v}$ is a short-ranged Coulomb potential, where the $\mathbf{G} = 0$ Fourier component is set to 0.

Writing $\bar{P}$ as a contraction of a two-particle polarization function, and using the Bethe-Salpeter equation (2.108) for P leads to the defining equation for the macroscopic polarization function:

$$\bar{P}(11^+,22^+) = -iG(12)G(2^+1^+) + i\int d3456 G(14)G(31^+)\Xi(3456)\bar{P}(56,22^+) \tag{2.113}$$

with the four point kernel Ξ that contains the screened electron-hole attraction and a short-range electron-hole exchange term:

$$\Xi(3456) = W(34)\delta(35)\delta(46) - \bar{v}(35)\delta(34)\delta(56). \tag{2.114}$$

Instead of calculating the microscopic polarization via (2.108) with the kernel W, and then using (2.111) to obtain $\bar{P}$, one can solve the Bethe-Salpeter equation with the modified kernel $\Xi = W - \bar{v}$ to obtain $\bar{P}$ directly.

2.5.6 Optical Excitation Calculations

To solve a Bethe-Salpeter equation such as (2.113), a four-point function has to be inverted at every frequency of interest. A more convenient and also intutive way is to expand $\bar{P}$ into the orthonormal and complete set of eigenfunctions $|\phi_i\rangle$ of the initial effective single-particle Hamiltonian:

$$\bar{P}(11', 22') = \sum_{n_1,\ldots,n_4} \phi^*_{n_1}(\mathbf{r}_1)\phi_{n_2}(\mathbf{r}_2)\phi_{n_3}(\mathbf{r}_3)\phi^*_{n_4}(\mathbf{r}_4)\bar{P}_{n_1n_2,n_3n_4}. \tag{2.115}$$

The matrix elements $\bar{P}_{n_1n_2,n_3n_4}$ are determined via

$$\bar{P}_{n_1n_2,n_3n_4} = [H^{exc} - \omega]^{-1}_{n_1n_2,n_3n_4}(f_{n_4} - f_{n_3}) \tag{2.116}$$

with the (effective two-particle) excitonic Hamiltonian

$$H^{exc}_{n_1n_2,n_3n_4} = (\epsilon_{n_2} - \epsilon_{n_1})\delta_{n_1,n_3}\delta_{n_2,n_4} + (f_{n_1} - f_{n_2})\Xi_{n_1n_2,n_3n_4}. \tag{2.117}$$

and the occupation numbers f_i and quasi-particle energies ϵ_i. This picture is very intuitive: for $\Xi = 0$ (no electron-hole interaction) H^{exc} is diagonal and contains quasi-particle energy differences on the diagonal; that corresponds to $\bar{P} = -iGG$, the random phase approximation. Including the electron-hole interaction means all excited states mix in the polarization matrix elements (2.116). The eigenvalues E_λ and eigenvectors A_λ of H^{exc} determine the macroscopic dielectric function by

$$\begin{aligned}\epsilon_M(\hat{\mathbf{q}}, \omega) = 1 - \lim_{\mathbf{q}\to 0} v(\mathbf{q}) \sum_{\lambda,\lambda'} \sum_{n_1,n_2} \langle\phi_{n_1}|e^{i\mathbf{q}\cdot\mathbf{r}}|\phi_{n_2}\rangle A^{n_1n_2}_\lambda \frac{1}{\omega - E_\lambda + i\eta} \\ \times \sum_{n_3,n_4} \langle\phi_{n_3}|e^{i\mathbf{q}\cdot\mathbf{r}'}|\phi_{n_4}\rangle A^{*\,n_3n_4}_{\lambda'}(f_{n_3} - f_{n_4}).\end{aligned} \tag{2.118}$$

The eigenvalues E_λ of the excitonic Hamiltonian H^{exc} determine the peak positions of $\epsilon_M(\omega)$, and the coefficients $A^{n_in_j}_\lambda$ determine the mixing of the formerly independent transitions $\langle\phi_i|e^{i\mathbf{q}\cdot\mathbf{r}}|\phi_j\rangle$.

A direct diagonalisation of H^{exc}, however, may not be feasible for large systems. Instead, determining the scalar product $\langle\mu \mid A_\lambda\rangle$ with $\mu_{ij} = \langle\phi_i|e^{i\mathbf{q}\cdot\mathbf{r}}|\phi_j\rangle$ from an initial value problem leads to an $\mathcal{O}(N^2)$ method to directly calculate $\epsilon_M(\omega)$ [60–62].

I like everything around me to be clear as crystal and completely calm.

Alfred Hitchcock

I am obsessed with ice cubes. Obsessed.

Drew Barrymore

3

Ground state properties of crystalline ice

3.1 Crystalline Ice

Water and ice have been, and continue to be, the subject of innumerable experimental and theoretical studies, due to their abundance on Earth and their important role in many chemical, biological, and geological processes, or simply because of their many unusual properties [4]. Understanding these properties is crucially linked to understanding the hydrogen bond network that forms in water's liquid and solid phase. The accurate quantum theoretical simulation of water is, however, still a formidable task.

Water in the crystallized state is tetrahedrally coordinated, see Figure 3.1. Each molecule donates and accepts two hydrogen bonds to/from neighbouring molecules, such that there is exactly one hydrogen atom between neighbouring oxygen atoms [63]. While this means that the local environment of all molecules in the crystal is similar, there are a multitude of possible

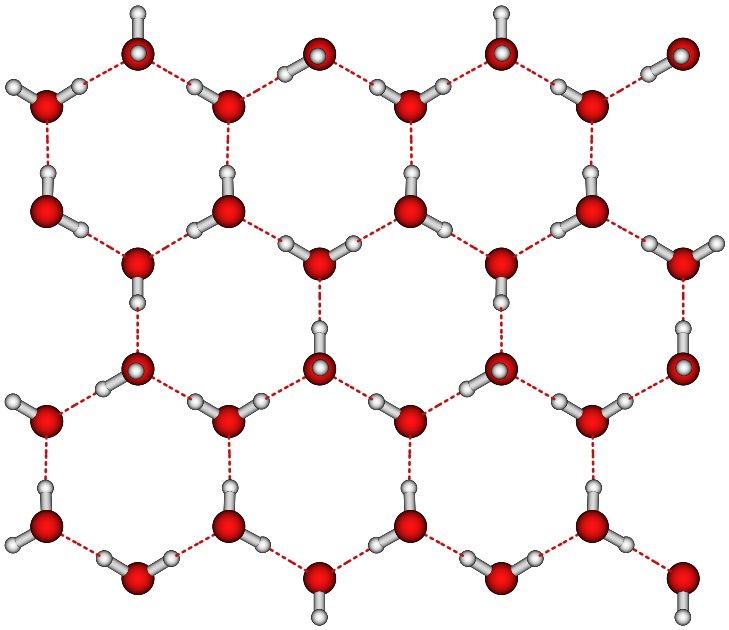

Figure 3.1: Ice Ih: crystal structure of this hydrogen-disordered hexagonal phase; top view along crystallographic c axis. Red (white) spheres indicate oxygen (hydrogen) atoms, dashed lines indicate hydrogen bonds.

arrangements of the ice crystal as a whole, due to the large number of possible distributions of donated and accepted hydrogen bonds [64]. Indeed, depending on temperature and pressure, water crystallizes in more than a dozen different structures, some of which occupy only small areas of phase space, see Figure 3.2, or do not have areas of absolute stability at all.

The ice we encounter daily, i.e. formed under low pressure from frozen liquid water, usually crystallizes in the hexagonal phase Ih, although a cubic phase Ic can also form. Both are hydrogen disordered structures, where the hydrogen bond network has a lower crystalline symmetry than the positions of the water molecules. More precisely, the notions "hexagonal" and "cubic" refer to the oxygen atoms' symmetry. In contrast to the hydrogen atoms' positions, oxygen atoms' positions are much more readily detected using low-energy electron diffraction (LEED). Under zero pressure, the average distance of neighbouring oxygen atoms is about 2.70Å, and the intramolecular OH distance is about $0.95 \cdots 1.00$Å.

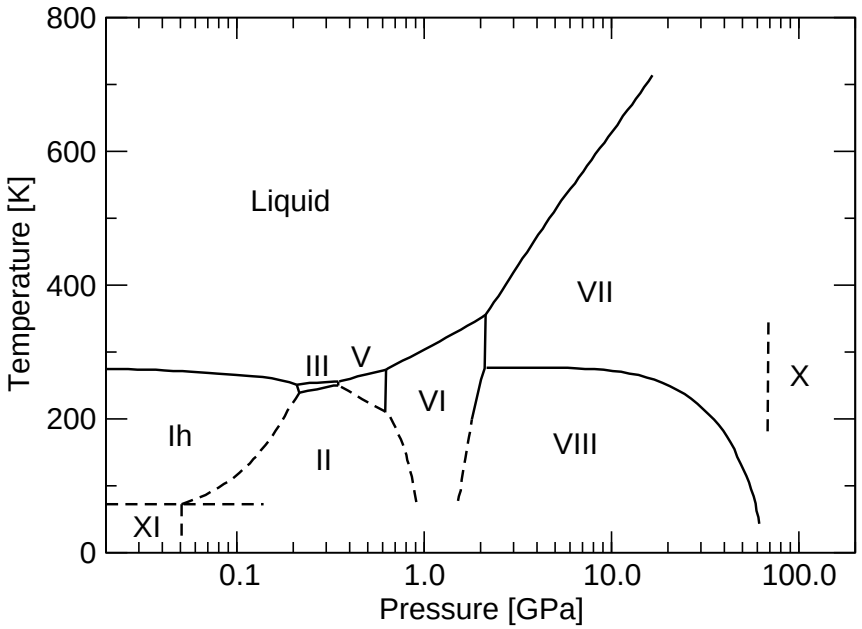

Figure 3.2: Phase diagram of liquid and solid phases of water; roman numerals denote different crystalline phases and their regions of stability. From Ref. [4].

The ice Ih and Ic phases are rather open and spacious. Increasing pressure can lead to complete rearrangement of the oxygen lattice, and thus very different crystal structures. At low temperatures and/or high pressures, hydrogen ordered phases are stable. For instance, ice XI is the ordered phase of ice Ih; ice VIII is the ordered phase of ice VII; and ice IX (which is metastable compared to ice II) is the ordered phase of ice III. Ice II itself is hydrogen ordered; it has a rhombohedral unit cell [65], see Figure 3.3. Going beyond these phases to higher pressure levels will lead to structural motifs with the nearest oxygen-oxygen (OO) distance being only twice as large as the intramolecular oxygen-hydrogen (OH) distance. In that case the hydrogen atoms will in fact sit between the oxygen atoms and bridge the OO bonds. Technically, the molecular character of the ice crystal breaks down at that point. It should be noted that the corresponding phase ice X has not been resolved unambiguously.

Computationally, a multitude of quantum chemical methods are routinely used to study water clusters [66–68], and extended systems are usually inves-

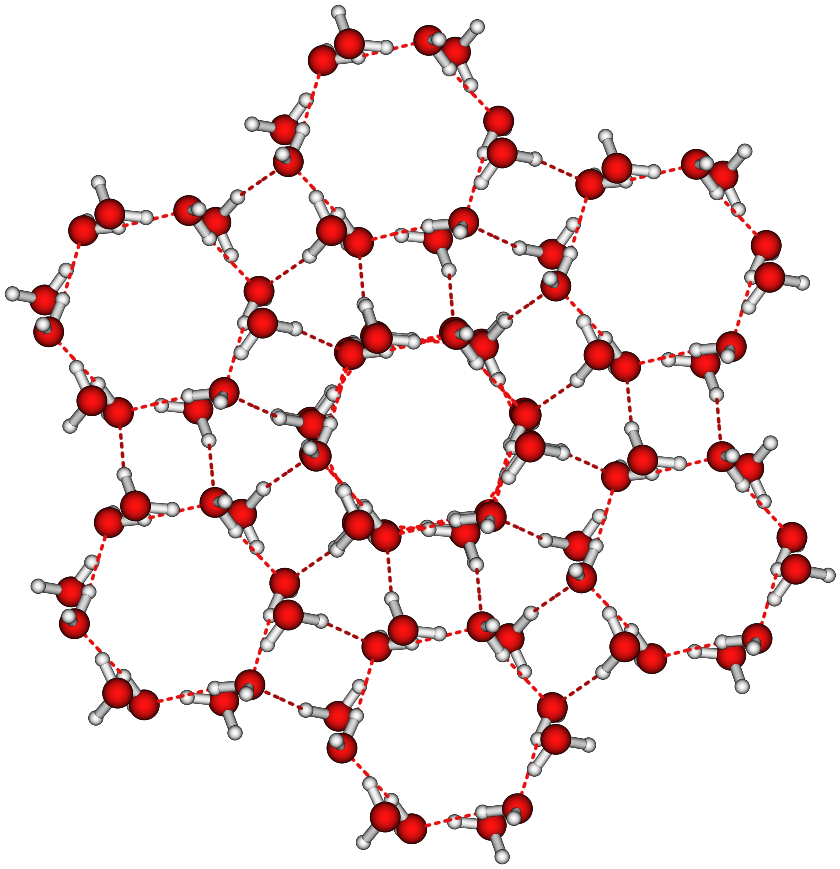

Figure 3.3: Crystal structure of the hydrogen ordered phase ice II. Top view along crystallographic *c* axis.

tigated by (semi)classical force field simulations or density functional theory based calculations. Correctly describing water's force field by a classical potential is a long-standing goal of the theoretical community. Originally, rigid frames of point charges would be used to describe water, with varying distribution and amount of electric charges [69–72]. The charges are fitted such that the potentials describe quantities like the melting point of ice, liquid water's density anomaly, or relative energies of various ice phases as accurately as possible. However, transferability of these potentials is rather low. An improvement are polarizable water models that allow for a response of the water molecule to its electrostatic environment [73–75]. These potentials are better suited to describe water in a broader variety of chemical environ-

ments. The potential from Ref. [75] is fitted not to experimental data but to *ab initio* calculations, and has been tested extensively on the water dimer's vibrational spectrum as well as on liquid water's structural properties [76,77].

Going beyond fitted potentials, density functional theory offers a computationally affordable way to calculate solid and liquid water. Following the introduction of non-norm conserving ultrasoft pseudopotentials in the 1990s [78], efficient plane wave basis set calculations of aqueous systems were possible, including the high-pressure transition to ice X [79], ground state properties of cubic ice Ic [80], and Car-Parrinello molecular dynamics [81] of liquid water [82,83]. After these early works, the question arose as to how well DFT is suited to describe the hydrogen bonds of ice and water. A systematic study of the performance of LDA and popular GGA functionals found that both PBE and PW91 are able to reproduce ground state properties of ice in good agreement with experiment [84]. These findings, however, were biased by a fortuitious error cancellation between the GGA functionals and non-convergence in the reciprocal space summation. More recent results [85–87] find that PBE and PW91 tend to overestimate ice's binding energy by up to 100 meV (about 15%) per molecule. They yield, however, equilibrium lattice constants in good agreement with experiment, see also section 3.2 below. This generally good performance, but also the lack of alternative *first principles* approaches, has led to wide usage of DFT for simulating liquid water and melting processes under extreme conditions [88,89], water at surfaces and interfaces, and solvation processes in water or ice [90,91].

3.2 Density Functional Theory calculations

Although DFT calculations of crystalline ice are available in the literature [84], they are presented here for two reasons. Firstly, to serve as a well defined starting point for further investigations, like the *ab initio* many-body treatment of crystalline ice (see section 3.4), the surface of ice (see chapter 4), or the optical properties of ice (see chapter 6). Secondly, to correct the point of view in the above mentioned literature [84] about the accuracy of the GGA functionals used.

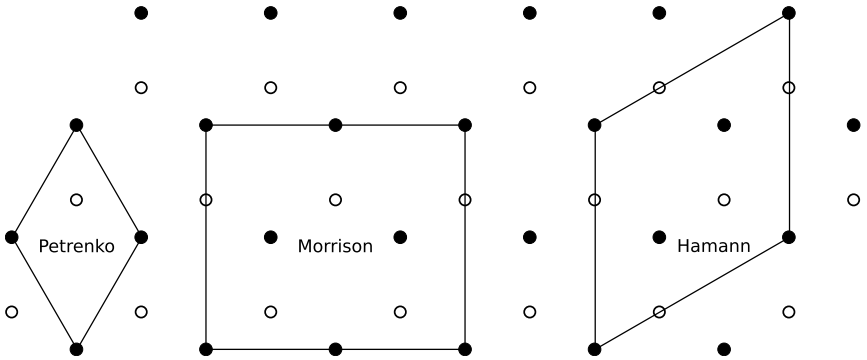

Figure 3.4: Commonly used unit cells for ice Ih by Petrenko *et al.* [92], Morrison *et al.* [93], and Hamann [84]. Filled (open) circles represent oxygen atoms at the corner of (inside) the primitive hexagonal unit cell.

3.2.1 Hexagonal ice Ih

Computational details of the calculations are presented in the next subsection, followed by results of the DFT calculations. Unless mentioned otherwise, the most common crystal structure of ice, hexagonal ice Ih, was studied.

Ice Ih has a hexagonal crystal structure; it forms bilayers of hydrogen-bonded water molecules, that are themselves connected by hydrogen bonds. The primitive unit cell contains four molecules [92]; it is, however, not possible to construct (by appropriate distribution of the hydrogen atoms) a primitive unit cell that has no permanent dipole moment. This unphysical situation would lead to problems and certainly errors in the description of ice, which is why bigger unit cells are used in calculations with periodic boundary conditions. Dipole free unit cells were suggested and used by Morrison *et al.* [93] and Hamann [84]; see Figure 3.4 for a top view on these cells. Hamann's cell contains 12 molecules, and Morrison's cell contains 16 molecules. Besides allowing for a dipole free unit cell, larger super cells are better positioned to simulate the hydrogen bond disorder found in ice Ih. The variation of the total energy depending on the microscopic arrangement of the hydrogen bond network was recently calculated to be of the order of 10 meV per molecule or less [86]. Note that while Morrison's super cell contains 16 molecules, it is made up of two identical orthorhombic sub-units,

each of which contain two symmetry non-equivalent water molecules.

3.2.2 Plane wave basis and pseudopotentials

To solve the KS equations (2.64) numerically in an actual calculations, the KS orbitals $|\phi_i\rangle$ have to be expanded into a suitable basis set $|\chi_q\rangle$:

$$|\phi_i\rangle = \sum_q \chi_{qi} |\chi_q\rangle,\ \chi_{qi} = \langle \chi_q \,|\, \phi_i \rangle. \tag{3.1}$$

Possible basis functions are Slater type orbitals (STO's) [94], which correctly describe the wave function's cusp at the nucleus; Gaussian type orbitals (GTO's) [95], which allow for efficient calculation of overlap and exchange integrals like (2.21); finite elements or a real space grid [96, 97], which allow high accuracy and good parallel scaling by domain decomposition; and plane waves. The latter are especially suited for periodic boundary condition calculations, both from a physical point of view, with electronic eigenfunctions (Bloch states) spread out over the entire system, and from a technical point of view, since the kinetic energy operator is diagonal, and symmetry in the periodic space simplifies the calculations' complexity.

Every plane wave $|\mathbf{q}\rangle$ is characterized by its wave vector $\mathbf{q}$, defined by $\langle \mathbf{r} \mid \mathbf{q} \rangle = e^{i\mathbf{q}\cdot\mathbf{r}}$. In a periodic system, the wave vector $\mathbf{q}$ can be split into $\mathbf{q} = \mathbf{k} + \mathbf{G}$, where $\mathbf{k}$ is in the first Brillouin zone, and $\mathbf{G}$ is a reciprocal lattice vector. That way, every electronic state can be expressed as

$$|\phi_{n\mathbf{k}}\rangle = \sum_{\mathbf{G}} \chi_{n\mathbf{k}}(\mathbf{G}) |\mathbf{kG}\rangle,\ \chi_{n\mathbf{k}}(\mathbf{G}) = \langle \mathbf{kG} \,|\, \phi_{n\mathbf{k}} \rangle. \tag{3.2}$$

$|\mathbf{kG}\rangle$ denote the plane wave basis vectors, $\langle \mathbf{r} \mid \mathbf{kG} \rangle = \exp i(\mathbf{k}+\mathbf{G})\cdot\mathbf{r}$. The sum over $\mathbf{G}$ has to be truncated in an actual calculation. A single parameter $G_{max} = \max|\mathbf{G}|$, the maximum length of all included reciprocal lattice vectors, controls the size of the plane wave basis. Increasing G_{max} or, equivalently, the kinetic energy cutoff $E_c = G_{max}^2/2$, increases the basis set size monotonously. All basis functions are orthogonal, thus no basis set superposition error occurs.

The number of basis functions scales like $E_c^{3/2}$, and a typical DFT calculation thus scales like $E_c^3 \ldots E_c^{4.5}$. In other words, it is desirable to minimize

the basis set expansion as much as possible. The inter-atomic part of the KS wave functions is generally well described by relatively few plane waves: over distance, the wave functions do not vary much. Near the nuclei, however, the KS wave functions will exhibit nodes and strong fluctuations, which contain high spatial frequencies and thus require a large cutoff energy E_c for a quantitatively good description. Much of the interesting physics and chemistry happens in the overlap regions of the valence orbitals; the core regions, and especially the core electrons, do not contribute significantly to a number of material properties such as equilibrium lattice constants, phonon frequencies, and optical properties. This argument justifies the "frozen core approximation", where the core electron wave functions are not determined self-consistently, but rather kept frozen from an all-electron atomic calculation. The KS equations (2.64) are then solved for the valence electrons only, however, with a modified one-electron potential V_{en}^c:

$$H_{KS}|\phi_i\rangle = \left[-\frac{1}{2}\nabla^2 + V_{en}^c + V_H[n_v] + V_{xc}[n_v]\right]|\phi_i\rangle = \varepsilon_i|\phi_i\rangle, \tag{3.3}$$

$$V_{en}^c = V_{en} + V_H[n_c] + V_{xc}[n_c + n_v] - V_{xc}[n_v]. \tag{3.4}$$

Here, n_c (n_v) denotes the core (valence) electron density. Due to the non-linearity of V_{xc} in $n(\mathbf{r})$, the core-valence exchange-correlation potential can be written exactly only as the difference $V_{xc}[n_c + n_v] - V_{xc}[n_v]$. It can be estimated, however, as

$$V_{xc}[n_c + n_v] - V_{xc}[n_v] \approx \sum_s V_{xc}[n_{c,s}^{AE} + n_{v,s}^{AE}] - V_{xc}[n_{v,s}^{AE}], \tag{3.5}$$

where s runs over all atomic centres in the unit cell, and n^{AE} denotes an electron density from an all-electron atomic calculation.

Applying the frozen-core approximation reduces the number of electronic degrees of freedom and can speed up calculations drastically. However, this is paid for by a certain unphysical description of the regions near the atomic nuclei. Going further, one can postulate that not only the description of the core but also of the *valence* electrons near the nuclei should have small influence on a large number of physical and chemical properties. Thus, employing a *pseudopotential*, that deviates from the actual potential close to the

nuclei and leads to a numerically convenient description of the valence electron wave functions, should be of much use while introducing only minor unphysical effects. The concept of pseudopotentials has received much attention since its introduction in atomic [98] and nuclear physics [99] and is a research field of ongoing activity. Whether or not the use of pseudopotentials will be rendered unnecessary by ever increasing computational power is difficult to say.

Norm-conserving Pseudopotentials

Introduced by Kleinman and Phillips [100], and after further work by Hamann *et al.* [101,102], an easy way to construct so called norm-conserving pseudopotentials was presented by Troullier and Martins [103]. Starting from a desired analytical fit of the wave function near the nucleus, the inverse radial Schrödinger equation is solved for each angular momentum component l for the pseudopotential. The pseudo wave function fulfills several physical and numerical conditions:

- Transferability : atomic all-electron and pseudo eigenvalues are equal, $\epsilon_l^{AE} = \epsilon_l^{PP}$, and wave functions are equal outside a cutoff radius r_l.
- Norm conservation: $\left\langle \phi_i^{PP} \middle| \phi_i^{PP} \right\rangle = 1$.
- Softness: $\left| \phi_i^{PP} \right\rangle$ is nodeless, and has no cusp at $r = 0$.
- Smoothness: at $r = r_l$, pseudo and all-electron wave function are equal up to fourth radial derivative.

Ultrasoft Pseudopotentials

Studying first-row elements with pseudopotentials of the Troullier-Martins type is numerically expensive, since the valence $2p$ orbitals are localized close to the nuclei. The cutoff radius r_p is thus rather small, and the smoothness and norm conservation conditions lead to a pseudo wave function that is not much different from the all-electron wave function. Thus, high plane wave cutoff energies (around 35 a.u. for oxygen) are necessary. Vanderbilt introduced so-called ultrasoft pseudopotentials, based on the following generalisations of the Troullier-Martins scheme [78]:

- Scattering properties of all-electron and pseudo state should not be equal at the eigenvalue ϵ^{AE} but at an arbitrarily chosen energy $\tilde{\epsilon}$ that is closer to the chemically interesting energy range.

- Scattering properties should be equal at *several* arbitrarily chosen energies $\tilde{\epsilon}_i$.

- Allow non-norm conserving pseudo wave functions.

The last condition transforms the KS problem into a generalized eigenvalue problem. The additional computational cost will in general be outweighed by the smaller plane wave basis set.

Central quantity is the overlap operator $\mathcal{S}$ between the pseudo wave functions:

$$\mathcal{S} = \mathbb{1} + \sum_{i,j} Q_{ij} |\beta_i\rangle\langle\beta_j|, \tag{3.6}$$

$$Q_{ij} = \langle \phi_i^{AE} \,|\, \phi_j^{AE} \rangle - \langle \phi_i^{PP} \,|\, \phi_j^{PP} \rangle \tag{3.7}$$

$$|\beta_i\rangle = \sum_j B_{ij}^{-1} |\chi_j\rangle \tag{3.8}$$

$$B_{ij} = \langle \phi_i^{PP} \,|\, \chi_j \rangle \tag{3.9}$$

$$|\chi_i\rangle = (\tilde{\epsilon}_i - T_e - V_{loc}) |\phi_i^{PP}\rangle \tag{3.10}$$

It fulfills the orthonormalization condition $\langle \phi_i^{PP} | \mathcal{S} | \phi_j^{PP} \rangle = \delta_{ij}$. The KS equations read

$$\left[-\frac{1}{2}\nabla^2 + V_{en}^c + V_H[n_v] + V_{xc}[n_v] + \sum_{ij} D_{ij} |\beta_i\rangle\langle\beta_j| \right] |\phi_i\rangle = \epsilon_i \mathcal{S} |\phi_i\rangle \tag{3.11}$$

$$D_{ij} = \int d^3\mathbf{r} \; (V_H[n_v] + V_{xc}[n_v]) \, Q_{ij}(\mathbf{r}) \tag{3.12}$$

Relaxing the norm-conservation condition allows significant reduction of the plane wave cutoff. First-row elements can be described accurately using a cutoff energy as low as 15 a.u. in case of oxygen [85].

Projector Augmented Wave Method

The central quantity in the ultrasoft pseudopotential scheme is the overlap operator $\mathcal{S}$. Recognizing that $\mathcal{S} = \mathcal{T}^{\dagger}\mathcal{T}$ is the square of a transformation operator $\mathcal{T}$ is the essential step to extend this scheme to the projector augmented wave method (PAW) [104]. Using $\mathcal{T}$ instead of $\mathcal{S}$ means constructing a frozen core approximation, combined with a dual basis set ansatz similar to LMTO or LAPW approaches. In the PAW method, radial projector functions transform between all-electron wave functions defined on a radial grid, and soft wave functions expanded into a plane wave basis set. This way, the all-electron wave functions near the nuclei are always available, unlike in the ultrasoft scheme, where they are lost. It also means that every observable will be evaluated on the plane wave grid and on the radial grid using the all-electron wave functions near the core. The PAW method is much better suited to compute e.g. optical properties, at a computational cost for the self-consistent step that is comparable to the ultrasoft pseudopotential scheme.

3.2.3 Results and Discussion

Density functional theory calculations are performed for crystalline ice Ih, using a plane wave basis and the projector augmented wave method as implemented in the Vienna Ab-initio Simulation Package (VASP) [105,106]. The exchange-correlation contribution to the total energy is modelled using the generalized gradient approximation (GGA) [40, 41]. For comparison, some calculations were performed within the local density approximation. The unit cell of Ref. [84] was used to model the hydrogen disordered hydrogen bond network. The cutoff energy for the wave function expansion is 15 a.u. Integrations over the Brillouin zone were sampled at 12 special k-points in the irreducible part [107]. For a given unit cell volume, internal degrees of freedom are relaxed until the remaining forces on the atoms are below 5 meV/Å. Minimum energies over the given lattice constant range are fitted with a solid state equation of state [108].

The description of hydrogen bonds is sensitive with respect to the exchange-correlation functional used [84]. Using the PW91 [40] and PBE [41] functionals, Hamann [84] obtained results for the sublimation energy, equi-

	a_0 [Å]	E_b [eV]	B_0 [kBar]	B'
Experiment	4.497	-0.580	89.0	
LDA	4.157	-1.139	263.6	4.56
GGA (PW91)	4.418	-0.702	157.6	4.71
GGA (PBE)	4.424	-0.670	149.0	5.01

Table 3.1: Ground state properties of ice Ih from DFT calculations: lattice constant a_0, binding energy E_b, bulk modulus B_0, and its derivative $B' = dB/dp$, listed for various exchange-correlation functionals and compared to experiment.

librium volume, and bulk modulus in very good agreement with experiment. Our calculations, however, result in an ice cohesive energy of 0.70 eV for the PW91 functional, somewhat higher than the experimental value of 0.58 eV per molecule [109], see Figure 3.5. The present result exceeds the value of 0.55 eV calculated in Ref. [84], but agrees with other recent calculations [86,87]. Hamann's results may suffer from a fortuitious cancellation between exchange-correlation functional errors and non-converged reciprocal space sampling. While the shortcomings of the exchange-correlation functional can not be avoided, care was taken in this study to achieve convergence in all numerical parameters such as the plane wave expansion and the sampling of the Brillouin zone.

The LDA significantly overestimates the hydrogen bond strength, see Table 3.1: the binding energy is about twice as large as found in experiment. Accordingly, lattice and elasticity constants are much smaller than found experimentally. Both GGA flavours, however, are much better suited to describe ice. The PW91 equilibrium lattice constant of 4.418 Å is about 1.8% smaller than the experimental value of 4.497 Å [110]. The rather large discrepancies for the bulk modulus may result from temperature effects, as the experiment was carried out at about 250K [111]. Because the PBE and PW91 functionals lead to almost the same results, PW91 is used for most ice DFT calculations in this work. The contribution of lattice vibrations to the sublimation energy of the crystal was also estimated, using monochromatic and Debye approximations for the intramolecular and rotational/translational vibrations, respectively. These sum up to 88 meV per molecule, in excellent agreement with the experimental result of 90 meV per molecule [109].

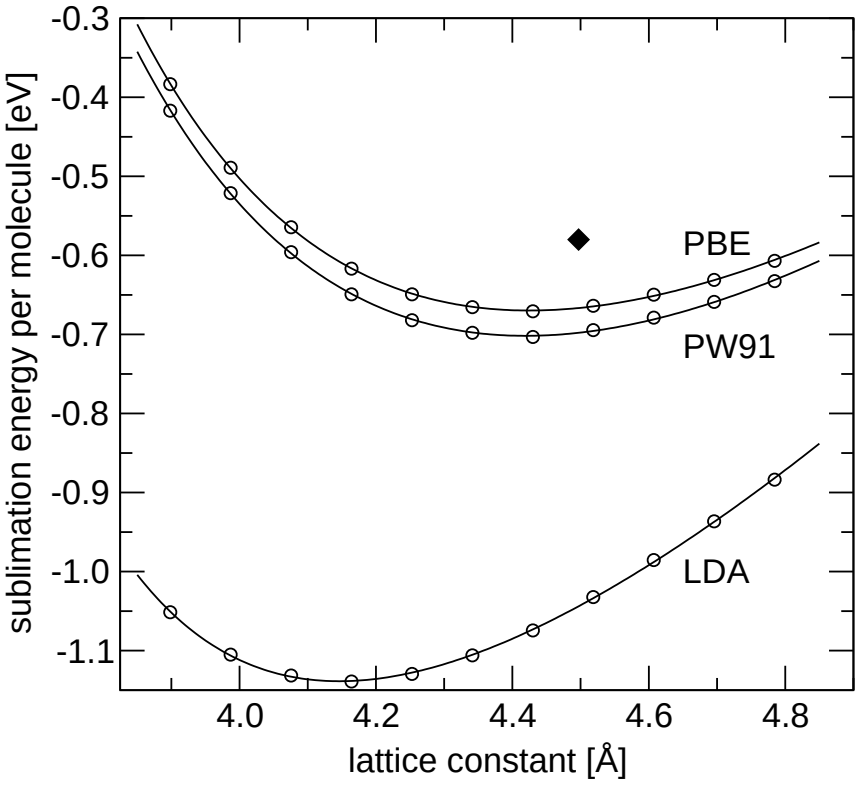

Figure 3.5: Cohesive energy of ice Ih, from DFT calculations. The filled diamond indicates experimental results [109, 110]. Figure taken from Ref. [85].

3.3 The Incremental Scheme

DFT calculations provide a means to calculate material properties rather quickly, and quite reliably. As seen above, they are also capable to describe hydrogen bonded ice. However, there is no systematic scheme to improve DFT results towards experimental accuracy. Wave function based methods offer this systematic improvement, be it configuration interaction (see section 2.3.2) or coupled cluster theory (see section 2.3.3). For extended systems, periodic Hartree-Fock calculations are well established but neglect electron correlation which often proves crucial when calculating material properties. It is highly desirable to go beyond the periodic HF scheme and include electron correlation for extended systems. However, the treatment of electron correlation from *first principles* methods constitutes one of the most fundamental problems in solid state physics. It is currently not known how to treat sys-

tems with small band gaps or even metals using accurate electron correlation methods such as the above mentioned CI or CC theories [112, 113].

A major improvement in this direction consists of the introduction of the incremental correlation method by Stoll and co-workers [114, 115], the successful application of which was reported even for metallic systems like mercury [116]. Note, however, that while this method is a way to systematically obtain correlation energy corrections, it is not a true two-particle theory that provides correlated wave functions in a periodic system. Instead, it combines an effective single-particle theory (Hartree-Fock) used in a periodic system with local correlation methods.

It was shown that the electron correlation energy of small water clusters converges rapidly with the order of the many-body decomposition in the interaction energy, much faster than the total interaction energy [117]. While this illustrates the local nature of electron correlation, it also raises the question whether solid water could be described by combining periodic HF calculations with localized correlation energy calculations truncated at two- or three-body level (see below). If the former is sufficient, for instance liquid water could be simulated from *ab initio* wave function based methods by combining HF calculations and a parametrized dimer correlation potential, in the spirit of a recently presented *ab initio* water pair potential [75].

In the incremental approach, the total interaction energy of ice is separated into the HF energy E_{HF} and the electron correlation energy E_c:

$$E = E_{\mathrm{HF}} + E_c. \tag{3.13}$$

E_{HF} is obtained from periodic Hartree-Fock calculations, whereas E_c (normalized to one unit cell) is expanded in a many-body decomposition [118]:

$$E_c = \sum_n E_c^{(n)} = \sum_i E_c^{(1)}(i) + \sum_{i,j} E_c^{(2)}(ij) + \sum_{i,jk} E_c^{(3)}(ijk) + \dots \tag{3.14}$$

The index i in each sum runs over all correlation units in the crystalline unit cell, whereas the higher indices $j, k, \dots$ run over the whole crystal. There is

an infinite number of many-body sums. The individual terms are defined as

$$E_c^{(1)}(i) = \epsilon_c(i) \tag{3.15}$$

$$E_c^{(2)}(ij) = \epsilon_c(ij) - \epsilon_c(i) - \epsilon_c(j) \tag{3.16}$$

$$E_c^{(3)}(ijk) = \epsilon_c(ijk) - \epsilon_c(ij) - \epsilon_c(jk) - \epsilon_c(ki) + \epsilon_c(i) + \epsilon_c(j) + \epsilon_c(k) \tag{3.17}$$

where $\epsilon_c(x)$ denotes the total correlation energy of correlation unit x. The incremental scheme proves a valuable computational tool if the series (3.14) converges sufficiently fast (i) in terms of number of sums that have to be considered, and (ii) in terms of number of contributions within each sum that have to be included. The first condition asks for the physical or chemical nature of the interaction in the system studied: how good is it described with a pure pair interaction, or how many higher-order interactions are important. The second condition asks for the range, or the screening, of the interaction: up to which distance are for instance pair interactions important. If the series (3.14) converges sufficiently fast, it can be truncated after the two- or three-body terms $E_c^{(2)}(ij)$ or $E_c^{(3)}(ijk)$. Another choice has to be made regarding which subsets of the atomic basis form the primitive correlated units. In case of ice, the natural choice is to treat every water molecule in the unit cell as smallest independent correlated unit.

The FORTRAN90 program `corrpbc` was written to perform the incremental scheme calculations. It interfaces with the CRYSTAL06 [119] program package for the periodic boundary condition Hartree-Fock calculations, and with the MOLPRO program package (2006 release version) for the local correlation energy calculations. Input data for `corrpbc` includes a complete CRYSTAL06 input file (including unit cell and atomic basis parameters, basis sets for the periodic HF calculations, k-point sampling, and all other computational parameters needed); basis sets for the correlation calculations; an energy threshold for the geometry optimization. Supported correlation methods are MBPT2 (see section 2.3.1) and CCSD(T) (see section 2.3.3). `corrpbc` can perform single point calculations and geometry optimizations; for the latter, it can optimize internal coordinates and/or unit cell parameters (either globally or at fixed unit cell volume). Gradients for all internal coordi-

nates are calculated analytically – for the HF energy E_{HF} from the periodic HF calculations, and for the correlation energy E_c from the localized correlation calculations, by $\nabla E_c = \nabla E_{tot}^{loc} - \nabla E_{\mathrm{HF}}^{loc}$. Gradients for the unit cell parameters are calculated numerically. Update of atomic coordinates and unit cell parameters (possibly constrained by the constant volume condition) is done by using either a conjugate gradient or a quasi-Newton optimization algorithm [120, 121]. Structural optimizations run until the change in the total energy $E = E_{\mathrm{HF}} + E_c$ is smaller than some energy criterion E_{min}. Implementing a gradient based criterion should also be possible. Figure 3.6 shows a flowchart diagram of `corrpbc`'s operation mode.

The program can be used for atomic and molecular crystals, with arbitrary choice of primitive correlation units. It can handle many-body expansions up to the trimer term $E_c^{(3)}(ijk)$. The monomer term $E_c^{(1)}$ is of interest in molecular crystals; although it is not expected to influence binding energies, it could contribute to changes of the equilibrium geometry. Note that no "embedding procedure" of any kind has been implemented; all localized units are calculated in the gas phase. Surrounding them by appropriate basis set centres, polarizable fields, or simply a dielectric background would make the generation of the local units more demanding, but take into account a screening effect of the interaction that may lead to faster convergence of the many-body expansion.

The selection of monomer, dimer, and trimer units is not automatised. Thus, all monomers, dimers, and trimers have to be handed to `corrpbc` explicitly. It should, however, be possible to extend the program to automatically generate all sub-units based e.g. on a distance cutoff criterion. Another optimization route would be parallelizing the correlation calculations, which can be performed independently.

3.4 *Ab initio* Study of Crystalline Ice Ih

We simulate the most common crystalline phase of ice under ambient conditions, hexagonal ice Ih. Its hydrogen bond disorder is considered by using the 16 molecule super cell by Morrison *et al.* [93]. Note, however, that Morrison's cell contains the same eight molecule unit cell twice. In our calcula-

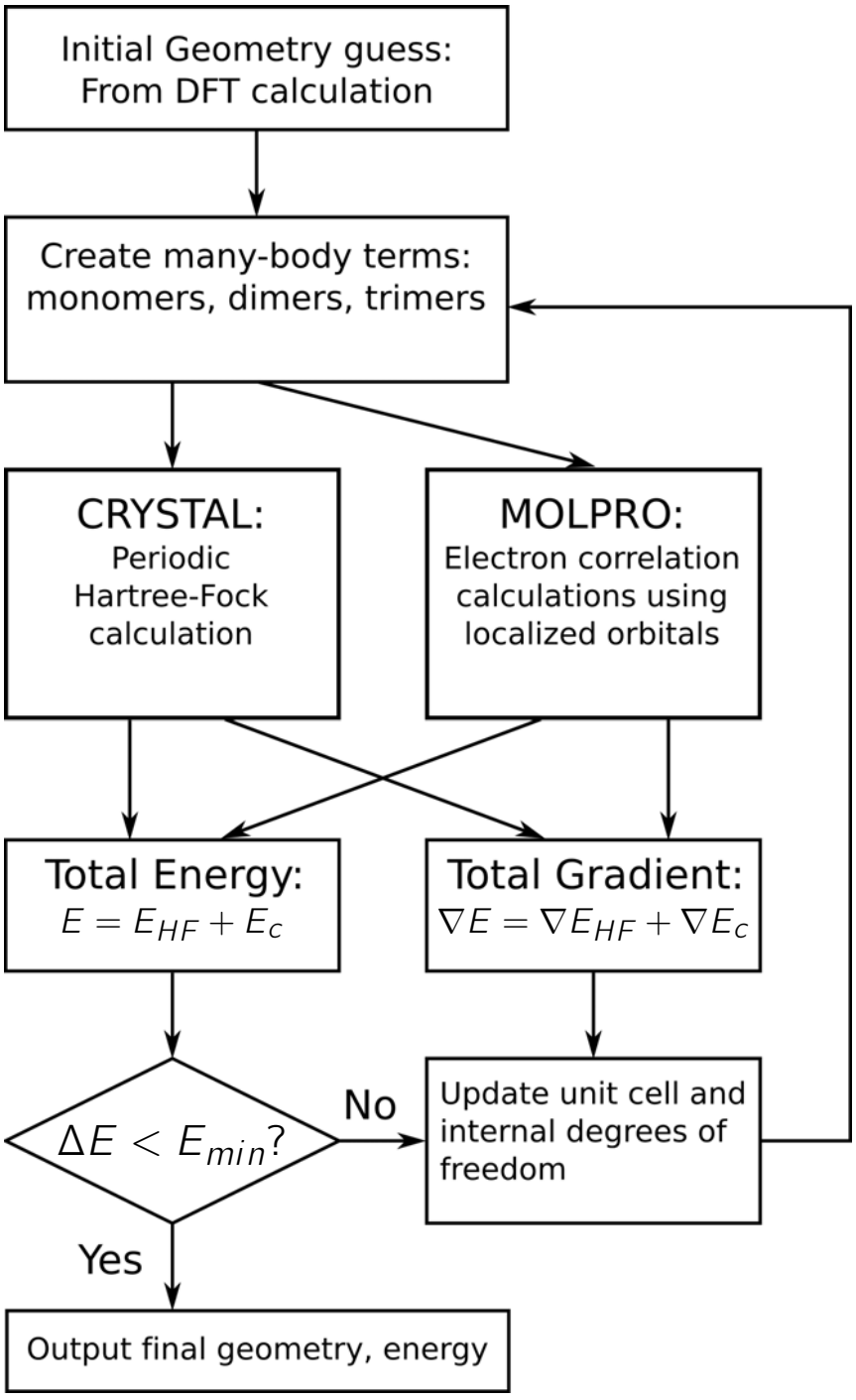

Figure 3.6: Flowchart of the incremental scheme program `corrpbc`.

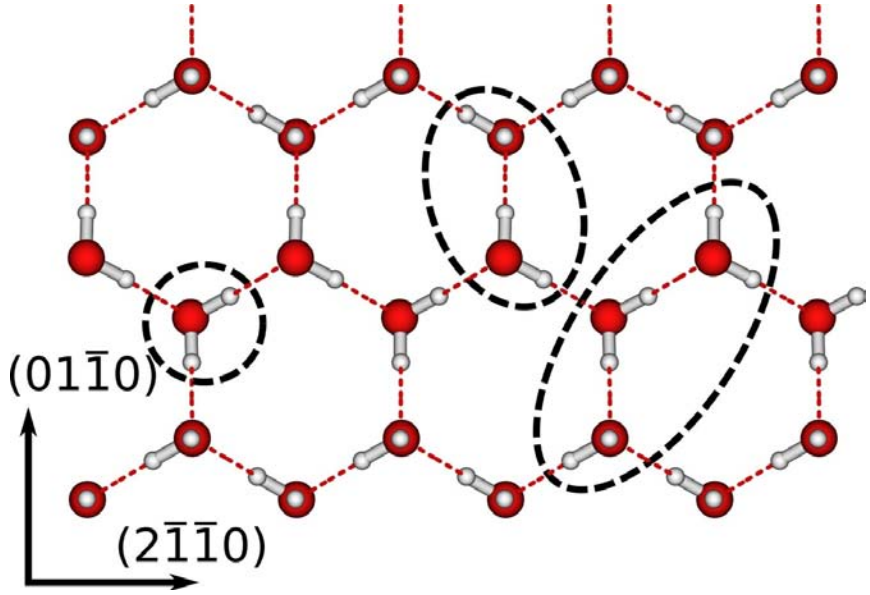

Figure 3.7: Top view on the ice Ih crystal structure, depicting one-, two-, and three-body terms used in the many-body decomposition of the crystal's correlation energy.

tions, we will use the primitive unit cell with eight water molecules. This orthorhombic unit cell, space group P6/mmm, contains *two* water molecules in the irreducible unit. Thus, six atomic positions and three unit cell coordinates are to be optimized.

Being a molecular crystal, the one-body correlation energies $E_c^{(1)}(i)$ describe intra-molecular correlation; they will influence the water molecule's geometry, and thus indirectly the hydrogen bond network. Going further, we study the influence of the two-body correlation, especially its spatial decay, and estimate the influence of three-body terms. See Figure 3.7 for a top view of the crystal structure and illustrations of two- and three-body terms.

3.4.1 Computational Details

Atom centered Gaussian basis sets for the periodic boundary calculations have to be chosen carefully: too diffuse basis functions cause linear dependencies or prohibit convergence of the iterative solution of the HF equations, while too small basis sets fail to describe correctly the hydrogen bonds in ice

Basis Set	Total Energy [a.u.]	r_{OH} [Å]	$\angle HOH$ [deg]
6-311G**	-76.047012	0.94098	105.46
aug-cc-pVTZ	-76.061203	0.94103	106.32
aug-cc-pVQZ	-76.066676	0.93980	106.32
aug-cc-pV5Z	-76.068009	0.93963	106.33

Table 3.2: Water molecule in gas phase, basis set tests. Comparison of total HF energies and molecular geometries.

and produce large basis set superposition errors (BSSE) [122]. We found several oxygen basis sets previously used in periodic HF calculations [123, 124] as well as common double zeta basis sets [125, 126] not to be suitable for describing ice: the above mentioned problems, namely too diffuse oxygen $2p$ basis functions, cause convergence problems. Dense, proton-ordered ice phases have been calculated successfully [127, 128] using the Hartree-Fock optimized split-valence 6-31G** basis sets developed by Pople *et al.* [129]. In our work Pople's 6-311G** basis sets [130] are used for both oxygen and hydrogen. Though they do not yield well converged energies for the water molecule in the gas phase, see Table 3.2, they are sufficient for solid state calculations, where the presence of basis functions on neighbouring molecular centres leads to an improved description of the electronic structure.

This very presence of basis functions, however, causes a basis set superposition error (BSSE) that needs to be taken into account when calculating the lattice (or binding) energy of the ice crystal. To calculate this binding energy, the BSSE in our solid state HF calculations is corrected for by using the Boys-Bernardi counterpoise scheme [122]: water's gas phase energy is calculated with empty basis sets on the positions of surrounding water molecules in the crystal. This corrected gas phase energy is then subtracted from the total energy of the unit cell to obtain the binding energy of the crystal. Table 3.3 shows the convergence of water's total energy with respect of the number of surrounding basis set centres. It shows that the total energy is converged to 10^{-3} a.u. after including three coordination shells of basis set centres. The corresponding energy $E = -76.053443$ a.u. is used as BSSE-corrected gas phase energy. The unit cell [93] is generated by *two* water molecules in the asymmetric unit. Their internal coordinates and the unit cell parameters are

No. of basis set shells	No. of molecular centres	Total energy [a.u.]
0	0	-76.047012
1	4	-76.052843
2	16	-76.053353
3	47	-76.053443

Table 3.3: Water molecule, BSSE correction for gas phase energy. HF energy calculated with 6-311G** basis set is listed versus the number of surrounding empty basis set centres on crystallographic positions.

optimized over a range of fixed unit cell volumes V. The energy-volume curve $E(V)$ is then fitted using Vinet's equation of state [108]. Brillouin zone integrations are sampled at eight special k-points [107].

Localized correlation calculations are performed using augmented correlation consistent triple zeta basis sets [131] for both oxygen and hydrogen. Both second order many-body perturbation theory [20] and coupled-cluster theory [132, 133] (CCSD(T), including single, double and perturbative triple excitations) are used to calculate correlation energies. The system's geometry is fully optimized up to inclusion of two-body next nearest neighbour interactions. Correlation contributions from outer neighbour shells are added as single point energy corrections to the minimum structure; too many dimer terms prohibited full geometry optimization in these cases. Similarly, all CCSD(T) energies are computed using the respective MBPT2 geometries; the correlation calculations were computationally too demanding to perform full geometry optimizations. A parallelized code for the correlation terms would be useful to perform these calculations.

Note that the correlation contributions also need to be corrected for BSSE. For instance, calculating the two-body increment $E_c^{(2)}(ij)$ involves subtraction of the one-body increments $E_c^{(1)}(i)$, $E_c^{(1)}(j)$, see (3.16). The one-body increment $E_c^{(1)}(i)$ ($E_c^{(1)}(j)$) should thus be calculated with the basis set of unit j (unit i) present. This has been implemented into `corrpbc`, and plays a significant role: the BSSE correction for $E_c^{(2)}$ only from the nearest neighbour two-body increments ranges from 41 to 49 meV per molecule, depending on the lattice constant. The BSSE correction for next nearest neighbour increments is even higher, ranging from 50 to 61 meV per molecule.

	a_0 [Å]	E_b [eV]	B_0 [kBar]	B'
Experiment	4.497[a]	-0.580[b]	89.0[c]	
(incl. ZPVE)		*-0.490*[b]		
HF only	4.735	-0.402	100.4	3.97
+MBPT2 $E_c^{(1)}$	4.686	-0.401	111.6	5.14
+MBPT2 $E_c^{(2)}$, NN	4.549	-0.530	142.9	5.03
+MBPT2 $E_c^{(2)}$, 2NN	4.518	-0.556	148.5	5.06
+MBPT2 $E_c^{(2)}$, 3NN	4.504	-0.568	151.4	5.12
+MBPT2 $E_c^{(2)}$, 5NN	4.501	-0.571	150.4	4.97
(incl. ZPVE)	*4.529*	*-0.470*	*135.4*	*5.27*
+MBPT2 $E_c^{(3)}$	4.509	-0.569	150.7	5.05
+CCSD(T) $E_c^{(1)}$	4.687	-0.401	107.9	5.43
+CCSD(T) $E_c^{(2)}$, NN	4.560	-0.529	141.3	5.44
+CCSD(T) $E_c^{(2)}$, 2NN	4.522	-0.560	148.3	5.40
+CCSD(T) $E_c^{(2)}$, 3NN	4.505	-0.574	153.3	5.68
+CCSD(T) $E_c^{(2)}$, 5NN	4.501	-0.577	152.4	5.54
(incl. ZPVE)	*4.529*	*-0.476*	*135.9*	*5.78*

[a] from Ref. [110]
[b] from Ref. [109]
[c] from Ref. [111]

Table 3.4: Ground state properties of ice Ih from incremental scheme calculations, compared to experimental values: equilibrium lattice constants a_0, lattice energies E_b, bulk moduli B_0, and their derivatives $B' = dB/dp$.

3.4.2 Results and Discussion

Essential results of the incremental scheme calculations are compiled in Table 3.4 and Figures 3.8 and 3.9, and compared to experimental data. The experimental lattice energy was obtained by Whalley by adjusting ice's heat of sublimation for zero point vibrational energy (ZPVE) corrections [109].

Periodic HF calculations underestimate the hydrogen bond network, yielding too large a lattice constant (4.735 Å as compared to 4.497 Å, more than 5% too large), and too small a binding energy (0.4 eV per molecule, missing about 30% of the interaction). Including one-body MBPT2-correlation terms $E_c^{(1)}(i)$, i.e. intramolecular correlation energies, does not improve these results, see also Figure 3.8. This is to be expected as most ground state

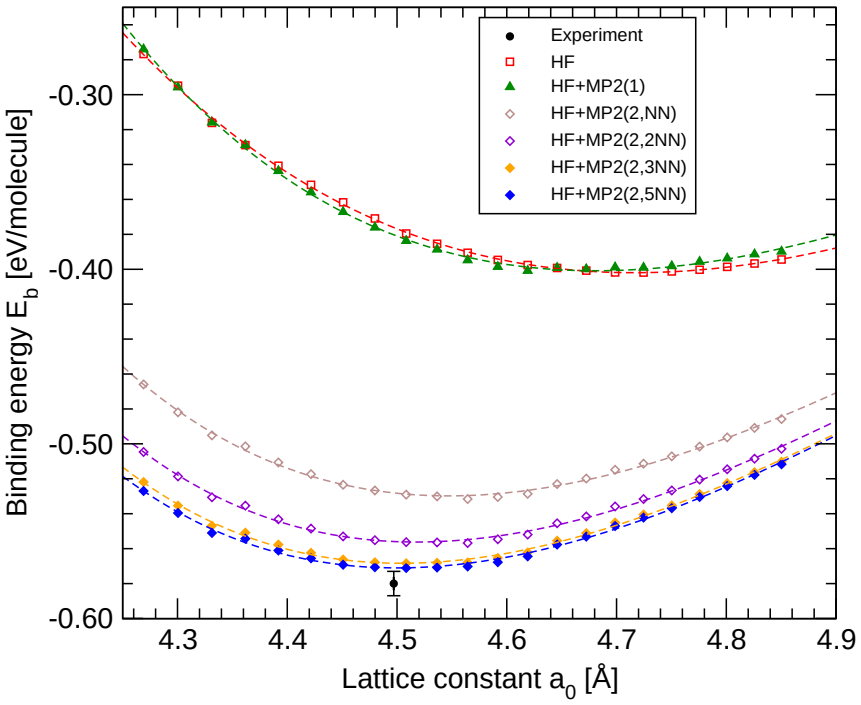

Figure 3.8: Lattice energy of ice from HF and various MBPT2 correlation treatments, compared to experiment [109, 110]. Notation: MP2(2,xNN) denotes periodic HF plus two-body MBPT2 up to the xth shell in nearest neighbors.

properties depend on the correct description of the *inter*molecular hydrogen bonds. However, including two-body terms $E_c^{(2)}(ij)$ leads to close agreement with experimental results, depending on the spatial extent over which the interactions are taken into account. Table 3.4 illustrates the improvement which is achieved by successively including outer neighbour shells into the two-body energy summation. We find the two-body interaction energy to be converged when including up to the third nearest neighbour shell, that is, including the 47 closest dimer correlation contributions for every molecule in the unit cell, up to a distance of roughly 7 Å (at equilibrium lattice constant). Including the 4th and 5th nearest neighbours (about 150 additional dimer terms, up to a distance of roughly 11 Å) adds only very small energy contributions of about $-2 \cdots -5$ meV per molecule to the total binding energy. A similarly rapid convergence behaviour was previously found in rare gas solid state calculations [134]. The thus obtained lattice constant of

4.501 Å from MBPT2 is in excellent agreement with the experimental result of 4.497 Å. The c/a ratio of 1.627 also agrees with experiment (1.628, [110]); at HF level, $c/a = 1.609$ is significantly smaller. Similarly, the lattice energy of -0.571 eV per molecule is very close to the experimental value of -0.580 $\pm$ 0.007 eV per molecule. As for the bulk modulus: the experimental value was obtained at $T = -16°C$ and is thus significantly smaller than the calculated values of about 150 kBar at absolute zero. Extrapolating experimental fits for $B_0(T)$ to absolute zero yields values ranging from $B_0(T = 0) = 107$ kBar [135] to $B_0(0) = 121$ kBar [111], still much smaller than the calculated value.

Advancing from many-body perturbation theory, we also used coupled cluster theory to calculate the local correlation contributions. Due to computational cost of these calculations, however, the respective MBPT2 geometries were used. The influence of the correlation method is rather weak, see Table 3.4 and Figure 3.9. Including all two-body terms up to the 5th coordination shell, we obtain an equilibrium lattice constant of 4.501 Å, and a binding energy of -0.577 eV per molecule. Again, both values are extremely close to experimental results, see Figure 3.9. As for the bulk modulus, we obtain a similar deviation from experimental results. Considering the temperature dependent quantity $B(T)$ was measured over a rather narrow range of temperatures, the theoretical value of $B_0 = 152.4$ kBar at the coupled cluster level is the most reliable reference value at 0 K. We further conclude that for the two-body summation of the correlation energy, a cutoff radius of about 7 Å gives reasonably converged results.

In water clusters, the three-body correlation energy $E_c^{(3)}(ijk)$ was previously found to be much smaller than the two-body term $E_c^{(2)}(ij)$ [117]. Moreover, that study found the three-body correlation to be mostly compensated by an equally large four-body term of opposite sign. For crystalline ice, the magnitude of the three-body correlation is estimated at MBPT2 level of theory by considering the most important three-body terms: water trimers with *two* hydrogen bonds, i.e. the most compact trimer configurations that can be constructed, see also Figure 3.7. Their contributions to the total energy sum up to between -0.4 meV and +5 meV per molecule, depending on the lattice constant; the changes in the ground state properties are

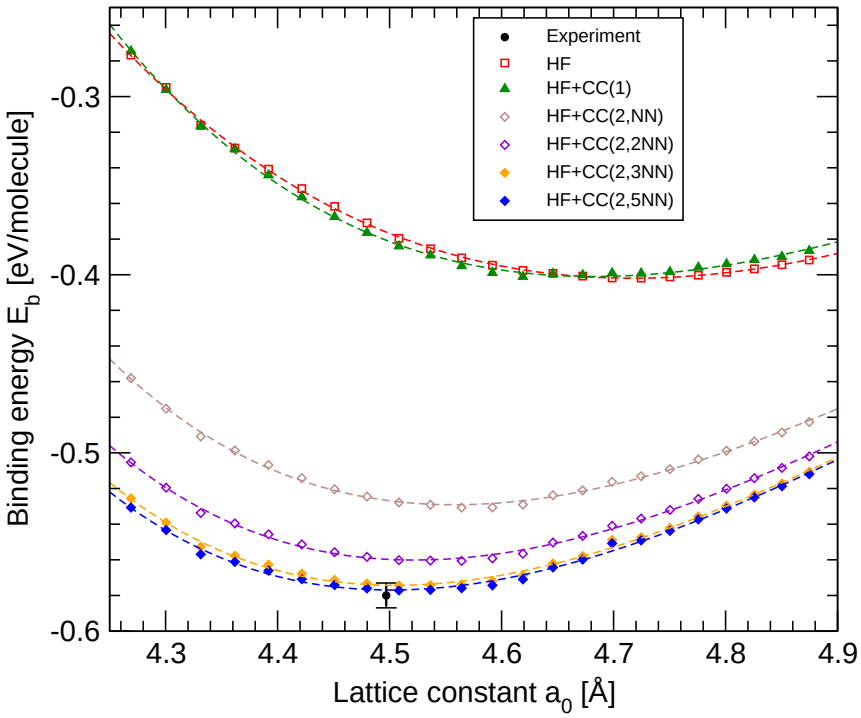

Figure 3.9: Lattice energy of ice from HF and various CCSD(T) correlation treatments, compared to experiment [109, 110]. For notation see Figure 3.8

thus comparably small, see Table 3.4. Three-body terms from more distantly located trimer configurations are expected to contribute much less to the correlation term $E_c^{(3)}(ijk)$. At equilibrium lattice constant, it holds $E_c^{(3)}(ijk) = 0.0012 E_c^{(2)}(ij)$, confirming the rapid convergence of the many-body expansion already found in finite water clusters. Thus, it should be reasonable to truncate the expansion after the two-body term, which in turn can be spatially restricted to a maximum distance of about 7 Å between the molecules considered.

The zero point vibrational energy of ice has been estimated to be 90 meV per molecule from experimental vibrational data [109], and 88 meV per molecule from DFT calculations [85]. Here, we perform a similar analysis for the calculated *ab initio* structures. Lattice vibrations are calculated at MBPT2 level of theory, using an augmented double zeta basis set [131], for the central molecule of a $(H_2O)_5$ cluster which in turn is embedded in the dipole electrostatic field of surrounding ice [136]. Acoustic (translational and libra-

tional) modes are occupied using the Debye model, optical (intramolecular) modes using the harmonic Einstein model. Over the volume range considered, binding energy shifts range from 110 meV to 87 meV per molecule, with 102 meV at the equilibrium lattice constant. The ZPVE-corrected binding energy of -0.470 (-0.476) eV from MBPT2 (CCSD(T)) calculations compares well to the experimental heat of sublimation of -0.490 eV, see Table 3.4. However, the equilibrium lattice constants are about 0.7% higher than in experiment. The simple vibrational model employed here most likely overestimates the ZPVE corrections, and a more accurate treatment of the phonon dispersion or the inclusion of anharmonicity effects should yield better results. The corrected bulk moduli decrease to about 135 kBar, in better agreement with extrapolated experimental results.

DFT calculations, see section 3.2, give less accurate results for ice's ground state properties. The local density approximation (LDA) for the electron exchange-correlation energy overestimates the hydrogen bond strength severely, resulting in a lattice constant 7.5% too small. Generalized gradient (GGA) functionals give better crystal parameters and bulk moduli, but still overestimate the lattice energy by about 100 meV per molecule. Judging from HF's underestimation of the hydrogen bond strength, it is expected and has been found recently [137] that hybrid-density functionals (by mixing in some exact exchange) should be somewhat better suited to describe solid water or ice. The optimized effective potential method [138,139] is another promising option to go beyond DFT. Both approaches, however, will achieve higher accuracy by significantly reducing the calculation speed, because the non-local exchange operator or an effective interaction kernel have to be calculated.

3.4.3 Conclusions

In conclusion, we have presented here the first *ab initio* many-body decomposition for the total energy of crystalline ice. In line with recent water cluster calculations it was shown that it is sufficient to truncate the correlation energy expansion after the two-body term. The calculated ground state properties agree very well with experimental data. We predict the bulk modulus of ice at very low temperatures to be higher than extrapolations from high-temperature measurements suggest. The fast convergence of the correlation

energy (regarding both the many-body expansion and the spatial extent of the interaction) justifies the combination of periodic HF calculations with a parametrized high-level *ab initio* dimer correlation potential, for instance in liquid water simulations. The application to liquid water simulations is of particular interest given the recent, as of yet unresolved, discussion in the literature about water's microscopic structure [10].

Beauty, like ice, our footing does betray;
Who can tread sure on the smooth, slippery way:
Pleased with the surface, we glide swiftly on,
And see the dangers that we cannot shun.

John Dryden

4

The surface of ice

The surface structure of ice, in contrast to the bulk properties of the crystal, remains little understood. Investigating the basal plane of hexagonal ice alone has been the aim of numerous experimental and theoretical studies, see, e.g., Ref. [140] for an early review, or Ref. [141] for a more recent work. One interesting question, which dated back to Faraday [142], is whether or not a quasi-liquid layer exists on the surface of ice. We now know that a pre-melting effect leads to a liquid layer on the ice surface, at temperatures lower than ice's melting point. However, the onset temperature T_p for this surface pre-melting is still debated. Recently, dynamical low-energy electron diffraction (LEED) at $T = 90$ K accompanied by Hartree-Fock total energy calculations and semi-empirical molecular dynamics (MD) simulations found the Ih(0001) basal plane to be fully bilayer-terminated and unreconstructed [143, 144]. Also, Helium atom scattering on thick ice layers, grown at $T = 125$ K, showed the surface to have 1×1 hexagonal symmetry and to be terminated by a full ice bilayer [145]. X-ray absorption spectroscopy measurements on ice films grown at $T = 130 \ldots 150$ K, on the other hand, indicate the presence of occupied surface sites different from bulk crystallographic

positions [146, 147]. The reported onset temperatures T_p of surface pre-melting seem to depend strongly on the respective method and experimental conditions. Surface vibrational spectroscopy studies found $T_p \approx 200$ K [148]. Other experimental studies, however, found T_p to be as high as 260 K [149]. Theoretical studies on the pre-melting of the surface reported significant surface disordering at $T = 230$ K in a semi-empirical MD study [150] and at $T = 190$ K in a Car-Parrinello MD study [151]. Obviously, the picture of the ice surface structure depending on temperature is far from complete. However, in the low-temperature regime, the assumption of a crystalline surface covered with ad-molecules seems to be justified.

Recent empirical calculations [152] using the TIP4P pair interaction potential [71] considered the adsorption, diffusion and island formation of water ad-molecules on ice. Surprisingly, for some adsorption configurations it was found that the binding energy of water ad-molecules exceeds the cohesive energy of the bulk [152]. That implies that the formation of many surfaces, e.g., by formation of microscopic ice clusters, would be thermodynamically favoured over the formation of macroscopic ice crystals – in crass disagreement with everyday experiences. The calculations presented here are modelling the surface structure of ice from *first principles*, using density functional theory.

4.1 Surface Calculations

Studying surface systems computationally is an especially challenging task. They are infinite (and periodic) within the surface plane, but semi-infinite (and thus non-periodic) along the surface normal directions. Both typical quantum chemical codes (which are optimized for 0D-periodicity) as well as solid state programs (designed for 3D-periodicity) must make compromises when treating surfaces. Either the surface is modelled by huge clusters (in a quantum chemical approach) or by repeated "slabs" of material, separated by sufficient vacuum (in a solid state approach). Both varieties demand huge computational resources: a cluster modelling a surface must be large enough to eliminate finite size effects; slab cells must contain enough material and vacuum to avoid spurious interactions between adjacent surfaces,

both through the material and the vacuum. Those restrictions mean surface calculations will easily be 10 to 100 times more computationally demanding than calculations for the corresponding bulk material.

Here, density functional theory calculations (DFT) are performed, to model the surface of ice. A plane-wave basis is used in conjunction with the projector augmented wave method (PAW) [104] as implemented in the Vienna Ab-initio Simulation Package (VASP) [105, 106]. The exchange-correlation contribution to the total energy is modelled using the PW91 functional within the generalized gradient approximation (GGA) [40]. The plane wave cutoff for the wave function expansion is 15 a.u. The surface is modelled by periodically repeated slabs: each slab contains four bilayers (eight layers) of ice within a 2×2 surface periodicity (see Figure 4.1 for a side view). The slabs are separated by vacuum, equivalent in its thickness to four ice bilayers (eight layers). Both the number of k-points and the thickness of the slab and the vacuum were tested for numerical convergence. Somewhat in contrast to the case of bulk calculations, we found the k-point sampling to be of minor importance for the calculation of surface formation energies and molecular adsorption energies. Upon changing the sampling of the surface Brillouin zone (BZ) from using the Γ point only to a regular mesh of 6 k-points in the irreducible part of the BZ, the calculated adsorption energies change only by a few meV per adsorbate molecule. We use 6 irreducible k-points for all surface calculations presented below. The adsorption geometries are relaxed until the remaining forces on the atoms are below 5 meV/Å. The oxygen atoms of the bottom bilayer of the slab are kept fixed in their ideal bulk positions.

To assess the influence of the proton disorder on the total energy of the slab describing the surface, different hydrogen bond configurations were calculated for a 16 molecule bulk cell of ice [93]. The total energy was found to fluctuate by less than 5 meV per molecule for the different structures. This confirms earlier force-field results for bulk ice cells [86]. The proton disorder *within* the slab is therefore not expected to affect the binding energy of an adsorbate molecule significantly. Thus, we construct the slab cells by first choosing the desired hydrogen arrangement at the surface and then proceed to distribute – obeying the ice rules – the remaining protons. The cells are set up to have

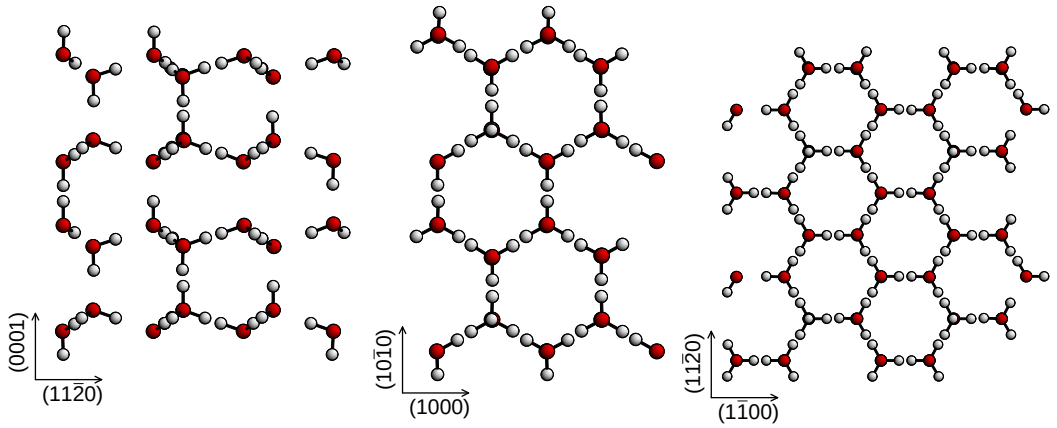

Figure 4.1: Slab realisations of low index surfaces of ice Ih, side views. From left to right: basal plane, (0001) surface; prism face, $(10\bar{1}0)$ surface; secondary prism face, $(11\bar{2}0)$ surface.

zero net dipole moment.

4.2 Surface formation energies for ice Ih

Ice Ih is a hexagonal crystal, and has several interesting low index surfaces, see Figure 4.2. The basal plane surface, along the crystallographic (0001) direction, is terminated by "chair" conformations of water rings of six hydrogen-bonded molecules. Ice Ih forms bilayers along the (0001) direction, that are in turn connected by hydrogen bonds. The primary prismatic face, along the $(10\bar{1}0)$ direction, has no identifiable bilayer structure, and the surface layer consists of folded six-rings of water molecules. The surface of the secondary prismatic face, along $(11\bar{2}0)$, consists of water dimer motifs connected to the sub-surface layer, see Figure 4.1. Note that all these surface features are derived from the ideal, bulk-like terminated surface constructions. However, in optimizing the surface geometries, we did not find major reconstructions for any of these surfaces, instead retaining these features.

We calculate the surface formation energies for the surfaces mentioned above, by using the slabs shown in Figure 4.1. The surface formation energy is actually an energy density per area, and equals to the energy cost involved in splitting an infinite crystal into two halves, thus creating two surfaces. Ob-

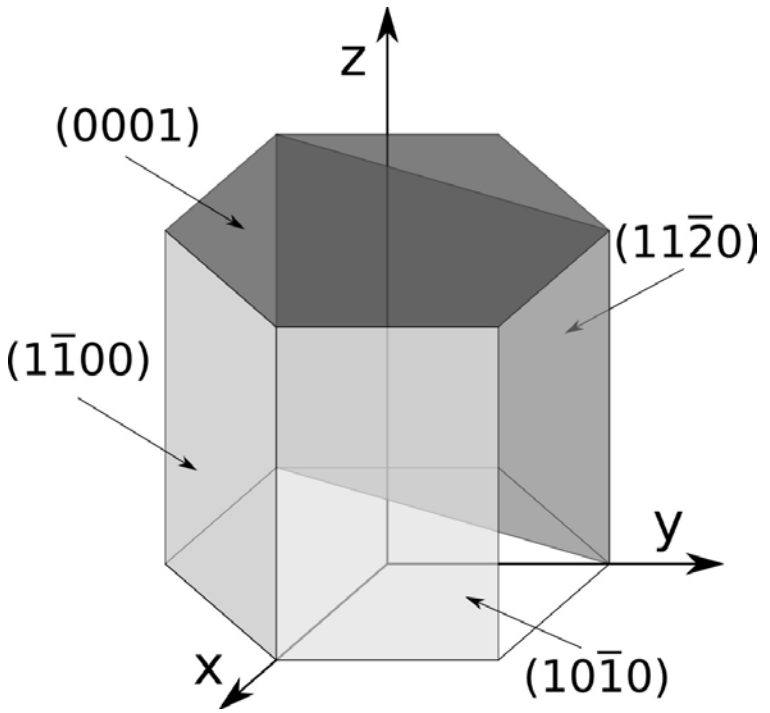

Figure 4.2: Common low index surfaces for hexagonal crystals.

viously, this cost will in general depend on the cleavage plane through the crystal, as different crystalline directions involve cutting more or less bonds, or allow for more or less favourable surface reconstructions.

From a slab calculation with N atoms or molecules, the surface formation energy E_f is determined by

$$E_f = \frac{E^{tot}_{slab} - N \times E^{tot}_{bulk}}{2A_{slab}}, \tag{4.1}$$

where E^{tot}_{slab} is the slab's total energy, E^{tot}_{bulk} is the bulk binding energy per atom/molecule, and A_{slab} is the slab surface area. Information about E_f for a variety of surfaces can be of use in determining the thermodynamic shape of a crystal – which at constant volume forms to have the smallest possible surface energy.

Table 4.1 lists the calculated formation energies for the different surface directions. Allowing optimization of the surface layers' geometries is important to obtain correct results, although the relative energetic order is

Surface direction	E_f [mJ/m^2], (ideal)	E_f [mJ/m^2], (reconstructed)	Previous work
Basal plane, (0001)	211	119	187 [a]
Prism face, $(10\bar{1}0)$	300	246	
Sec. prism face, $(11\bar{2}0)$	239	196	127[a]

[a] from Ref. [153]

Table 4.1: Surface formation energies for various low index surfaces of ice Ih for both ideal (fixed bulk) surfaces, and reconstructed surfaces, compared to previous theoretical work.

preserved. The calculated energies do not agree with previous theoretical work [153], where sums of the electrostatic energy of (semi-)infinite crystals were investigated. We assume that the *first principles* approach used here should be the more accurate description. In Figure 4.3, we show the corresponding Wulff crystal. It features prominently the basal plane, along the (0001) direction, and the secondary prism plane, along $(11\bar{2}0)$ direction. The primary prismatic face, along the $(10\bar{1}0)$ direction, is energetically too unfavourable to form. While the Wulff shape shows how an ice crystal *can* look like, the wide variety of small ice crystals is well known, and illustrates that the Wulff construction is a purely thermodynamic ansatz. It ignores kinetic properties such as diffusion coefficients and barriers, that hinder a crystal from always growing in its thermodynamically favored shape. While there are no direct measurements of ice's surface enthalpy of formation energy, we can compare our result to the surface tension of liquid water, which is about 119 mJ/m^2 [154]: the average surface tension of the Wulff crystal is about 149 mJ/m^2, thus overestimating the liquid's experimental result by about 25 per cent. This is to be expected: keeping in mind that the hydrogen bond strength in ice is overestimated by the DFT method used (by about 15 per cent), the surface formation energies tend to be too large, too.

4.3 Monomer adsorption on the basal plane

Inspired by the certainly interesting results by Batista *et al.* [152], the adsorption of water molecules on the surface of ice is studied. As found in the

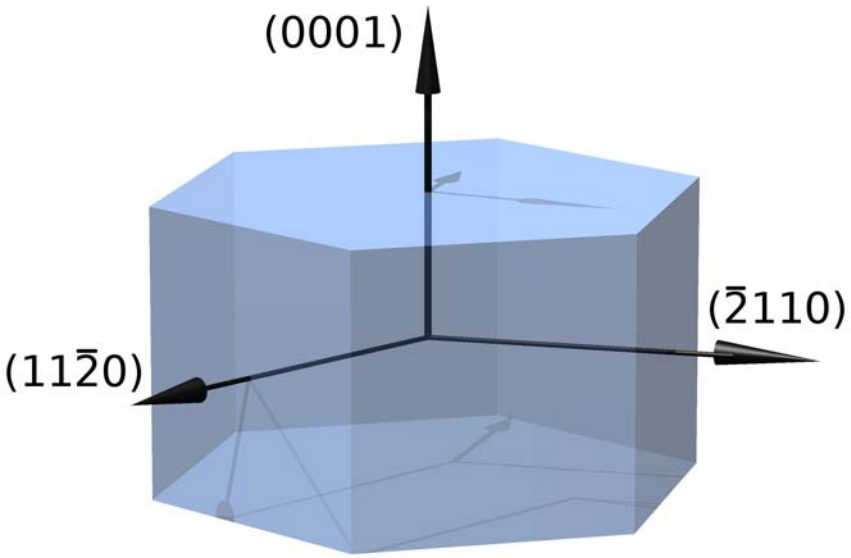

Figure 4.3: Wulff shape construction of the ice Ih crystal, with surface energy data from Table 4.1.

previous section, the basal plane is the thermodynamically most favoured crystal cleavage plane, and also appears most often in nature; we thus limit this study to water adsorption on the basal plane of hexagonal ice Ih.

Single molecule adsorption

The adsorption of single monomers on the full-bilayer terminated surface is studied first. Out of the many adsorption sites possible, we focus on the most favored structures considered in the work of Batista *et al.* [152]. The possible adsorption sites are classified by the orientation of the three water molecules in the uppermost surface layer that are closest to the adsorbing molecule (such a distinction is always possible, due to the hexagonal crystal structure of ice Ih). Four arrangements are possible, which are distinguished by the number of OH groups pointing upwards along the surface normal. The first one (here labelled "A") has one OH group pointing upwards. The possible adsorption configurations A-1 and A-2 are shown in Figure 4.4. They differ with respect to the lateral position of the ad-molecule. In both cases, the

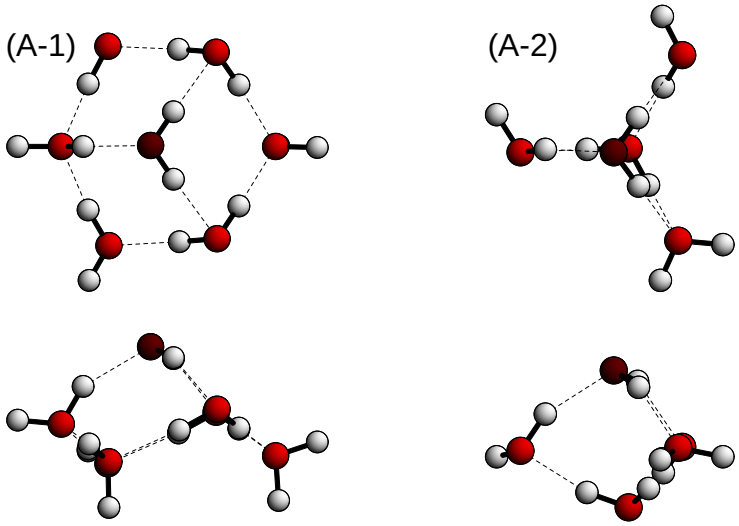

Figure 4.4: Adsorption site type A (one surface OH group pointing upwards). Adsorbate molecule (dark red oxygen atom) and uppermost surface layer molecules are shown. Left (right): optimized geometries in position A-1 (A-2). Upper panel: top views; lower panel: side views.

final positions of the adsorbed molecules are similar: they rotate towards the surface and establish hydrogen bonds with the substrate oxygen atoms' lone pairs. The nearest upward-pointing OH group on the surface rotates towards the ad-molecule to form a third hydrogen bond. This rotation is restricted by the back bonds of the surface layer molecule with the water molecules in the sub-surface layer.

The binding energy of the adsorbate in A-1 is 0.58 eV, about 82% of the bulk cohesive energy (see Table 4.2). This is in clear contrast to the TIP4P calculations that find the surface binding energy stronger than in the bulk [152]. It is, however, in agreement with the fact that macroscopic ice crystals do exist and are stable. Nevertheless, the adsorption energy calculated here is slightly larger than expected from a mere bond-counting approach, given that only three hydrogen bonds to the substrate are formed, compared to four in the bulk case. But also for the surface of liquid water it was argued recently that undercoordinated water monomers tend to enhance the existing hydrogen bonds compared to the bulk configuration [10]. In the present case, the ad-molecule does not occupy a regular crystal position and the uppermost substrate molecules also relax from their ideal bulk positions. The internal

Geometry	Adsorption energy [eV]	$d(\mathrm{OH})$ [Å]	$d(\mathrm{OH}\cdot\mathrm{O})$ [Å]	$d'(\mathrm{O}\cdot\mathrm{HO})$ [Å]
A-1	0.575	0.99	2.04	1.78
		0.99	2.06	
A-2	0.552	0.98	2.25	1.82
		0.98	2.05	
B-1	0.548	1.00	1.79	1.94
				2.60
B-2	0.550	1.00	1.81	2.07
				2.26
Bridge	0.576	1.01	1.68	1.69
		1.01	1.68	

Table 4.2: Adsorption energies and geometric parameters for the configurations shown in Figures 4.4, 4.5, and 4.6. $d(\mathrm{OH})$ are the bond length(s) of adsorbate OH group(s) involved in bonding, $d(\mathrm{OH}\cdot\mathrm{O})$ the hydrogen bond length(s) to the substrate, $d'(\mathrm{O}\cdot\mathrm{HO})$ the distance from adsorbing oxygen to upward pointing OH group(s).

relaxation of the ad-molecule is small, its OH bond lengths are only slightly stretched compared to the gas phase geometry. The uppermost substrate molecules move out of the surface by up to 0.3 Å. This decreases the OH·O hydrogen bond lengths, which vary from 1.78 Å to 2.06 Å. However, they are still remarkably larger than the bulk value of 1.69 Å. The HOO hydrogen bond angles vary from 12.9° to 18.4°. These values are well within common geometrical boundaries for hydrogen bonds [10, 88]. To estimate the influence of the substrate relaxation on the binding energy, a A-1 geometry with substrate frozen in its optimized free surface geometry was calculated. The resulting binding energy is 0.44 eV, which lets us estimate that the substrate relaxation accounts for about 0.14 eV of the total adsorption energy.

The adsorption energy at the A-2 adsorption site is 0.55 eV, about 79% of the bulk cohesive energy. The adsorbing molecule donates two hydrogen bonds to the substrate atoms and accepts one hydrogen bond from the upward-pointing OH group. The substrate atoms that participate in the bonding slightly shift towards the adsorbate. The hydrogen bond donating molecule moves the most, about 0.3 Å. The ad-molecule effectively preserves its gas phase structure: the OH bond lengths are slightly stretched to 0.98 Å,

the HOH angle decreases to 103.8°. The OH·O distances and HOO angles of the three hydrogen bonds vary between 1.82 Å and 2.25 Å, and 13.3° and 18.9°, respectively.

Another possible adsorption site (here labelled "B") has two OH groups pointing upwards in the uppermost ice layer. The corresponding relaxed adsorption configurations B-1 and B-2 are shown in Figure 4.5. Again, they differ with respect to the lateral position of the adsorbing molecule. In both cases the ad-molecule donates a single hydrogen bond to the substrate and accepts two weaker bonds from the surface molecules. Its bond donating OH group is elongated to 1.00 Å, the OH·O distance is about 1.80 Å. However, finite HOO angles of 11.0° and 10.6° remain for both B-1 and B-2, respectively. The two upward-pointing OH groups on the surface rotate towards the adsorbing molecule's oxygen atom to form weaker hydrogen bonds. The binding energies are in both cases about 0.55 eV and thus very similar to the A-2 site's binding energy. For B-1 we determine a substrate relaxation contribution of about 0.17 eV to the total adsorption energy. This is slightly larger than in the A site, because the rotation of *two* surface OH groups towards the adsorbate yields a higher gain in binding energy.

Interestingly, although the adsorption sites are clearly different, the calculated adsorption energies are rather similar, with only a slight preferrence for the A-1 site. However, if we compare the geometrical properties of the hydrogen bonds formed, see Table 4.2, we find that all adsorption situations are in fact quite similar: one rather short hydrogen bond (bond length about 1.8 Å) and two longer hydrogen bonds (longer than 2.0 Å) are formed. The longer bonds are in addition more distorted than the short bonds. This holds for all adsorption sites investigated. Thus, the direct vicinity of the adsorbing molecule is not as important for the adsorption energy as might be expected. Instead, a variety of adsorption sites offer similar possibilities for the adsorbing water molecule to establish hydrogen bonds. The contributions of zero point vibrations are therefore expected to be similar in all studied cases. Furthermore, they are expected to be smaller than the bulk value of 88 meV per molecule.

There are two more adsorption sites conceivable: with three and with zero OH groups pointing upwards at the surface, respectively. Within a 2×2 sur-

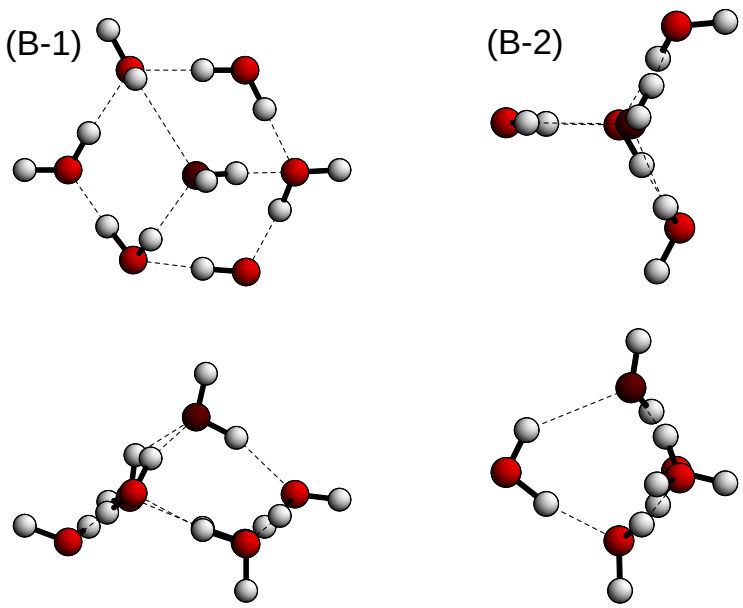

Figure 4.5: Adsorption site type B (two surface OH groups pointing upwards). Left (right): optimized geometries in position B-1 (B-2). Upper panel: top view; lower panel: side view.

face periodicity, however, no slabs for these surface configurations can be set up that obey both the ice rules and have a net zero dipole moment. Because the surface periodicity of 4×2 that is compatible with these requirements is too large for the computational resources available, these adsorption sites are not considered in this work. In any case, the adsorption of water monomers on sites with three or zero OH groups pointing upwards was previously found to be far less favored than in A or B configurations [152], mostly due to the fact that only two hydrogen bonds can be established between substrate and adsorbate.

The relation between the adsorption energy of an ad-molecule and the surface formation energy per surface molecule determines the formation of either flat or rough surfaces. We find that depending on the specific geometry the adsorption of water monomers on non-crystallographic adsorption sites lowers the surface formation energy – compared to the ideal full-bilayer termination – slightly, by up to 30 meV per molecule. The DFT calculations thus predict a weak tendency to surface roughening.

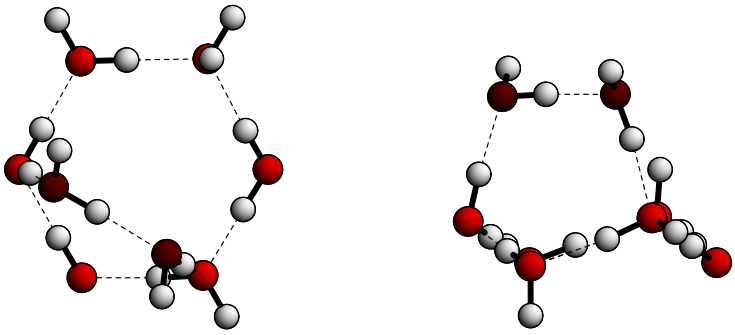

Figure 4.6: Co-adsorption of two water molecules: "dimer" or "bridge" configuration. Left: top view; right: side view.

Higher surface coverage

We also investigate one adsorption configuration for higher coverage, with two molecules arranged in the 2×2 surface cell as suggested in Ref. [147]. The optimized adsorption geometry is shown in Figure 4.6. The calculated adsorption energy for this configuration is 0.58 eV per ad-molecule and thus nearly equal to the most preferred single ad-molecule configuration A-1. Again, there is a slight overbinding compared to the bulk cohesive energy: three newly established hydrogen bonds equals to an energy of 0.38 eV per bond, compared to 0.35 eV in bulk ice. The two ad-molecules relax into a structure similar to the gas phase water dimer [155], but slightly contracted. This dimer-like structure allows for the ad-molecules to establish rather strain-free hydrogen bonds to the substrate. Indeed, all adsorption-induced hydrogen bonds have a bond length of about 1.69 Å, close to the bulk value. The relaxation of the substrate molecules is small, with displacements of 0.10 Å and 0.19 Å. However, these relaxations lead to the enhanced binding energy per bond when compared to the bulk.

Further increase of adsorbate coverage should result in the formation of the next half bilayer on the surface. However, our calculations show that this is not a stable configuration; the adsorbed half bilayer tends to separate from the underlying bulk. This result is in agreement with experimental findings [145].

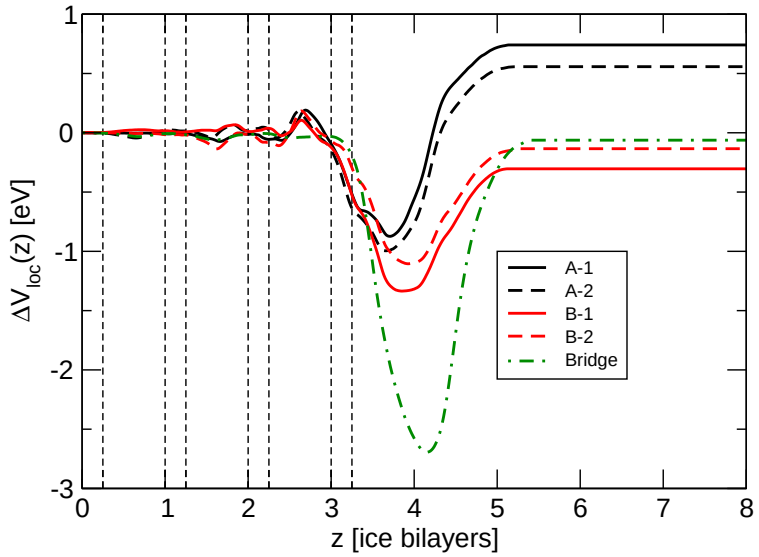

Figure 4.7: Surface plane averaged and smoothed potential differences with respect to the clean surface (see text), plotted along the surface normal. The abscissa is scaled in units of ice bilayers, dashed vertical lines indicate the positions of the substrate ice layers.

Influence on the surface dipole moment

In general, adatoms or adsorbed molecules may cause or modify a surface dipole layer. This allows to determine the initial-state contributions to the ionization energy [156, 157] that can be considered to dominate in the cases of doped semiconductors. For molecular crystals, in addition, final-state effects may be important for the total ionization energy. Still, changes of the surface dipole layer will also in this case largely determine the changes of the ionization energy. Therefore we study the influence of ad-molecules on the variation of the local electronic potential $V_{loc}(\mathbf{r})$ across the surface region. It is given in DFT-GGA as

$$V_{loc}(\mathbf{r}) = V_{loc}^{PS}(\mathbf{r}) + V_H(\mathbf{r}) + V_{xc}(\mathbf{r}), \tag{4.2}$$

where $V_{loc}^{PS}(\mathbf{r})$, $V_H(\mathbf{r})$ and $V_{xc}(\mathbf{r})$ are the local part of the pseudopotential, the Hartree and the exchange-correlation potential, respectively. Laterally averaging $V_{loc}(\mathbf{r})$ yields the in-plane averaged potential $V_{loc}(z)$. By subtracting

the potential $V^0_{loc}(z)$ of the free surface

$$\Delta V_{loc}(z) = V_{loc}(z) - V^0_{loc}(z), \tag{4.3}$$

the influence of the adsorbate on the local potential is obtained. In Figure 4.7, $\Delta V_{loc}(z)$ is plotted for all investigated configurations along the surface normal z. The potential is also averaged along the z direction over the width of one ice bilayer, thus yielding identically zero in ideal bulk regions beneath the slab surface. In all cases, the adsorbed molecules change the electrostatic potential near the surface and to some extent in the slab. However, only in the A sites a significant increase of the surface dipole layer (indicative for an increase of the ionization energy) of more than 0.5 eV is observed. This contrasts with the far larger changes of the ionization energy calculated for molecular adsorption on semiconductor surfaces, see, e.g. Ref. [158]. It is most likely related to the flexibility of the hydrogen bonds that allow for a relatively free reorientation of the ad-molecules that try to compensate rather than enhance long-range electric fields.

4.4 Conclusions

In summary, the adsorption of water monomers on the ice Ih basal plane is found to be energetically very favorable. In contrast to earlier empirical calculations, however, we do not find adsorption energies in excess of the bulk cohesive energy. Nevertheless, due to an energy gain per hydrogen bond larger than in the bulk, the adsorption of ad-molecules lowers the surface energy. This is expected to favour the formation of rough surface structures which may be suitable to explain recent experimental findings of an abundance of isotropically distributed OH groups that terminate the crystalline ice [147]. The adsorption of water monomers has little impact on the surface dipole layer.

Electricity is the power that causes all natural phenomena not known to be caused by something else.

Ambrose Bierce

5

Charge localization at the surface of ice

The properties of charged clusters or charges localizing at surfaces are of great interest in cluster and surface science, atmospheric chemistry and astrophysics. Aqueous systems are especially intriguing due to water's unique role in many biological, chemical and technological processes [159, 160]. Experiments on anionic aqueous systems range from first measurement of the spectra of a solvated electron in bulk water [161] and water clusters [162] to recent studies of ultrafast solvated electron dynamics in water and thin ice films [163–166].

Water clusters have been studied thoroughly both experimentally and theoretically over the last decades; anionic water clusters again are of special interest since the polar environment, together with the rather unrestricted rotational degrees of freedom of the water molecules involved, should allow for self-trapping of excess electrons within the clusters. Indeed, depending on cluster size and preparation conditions, possible electron localization sites have been found both at the surface and in the interior of water clus-

ters [66–68, 167–175]. While for small water clusters the excess electron's localization in a surface state seems well established, there is ongoing debate about how large a water cluster has to be to provide interior localization sites, or even for interior localization to be the dominant process [68, 167, 173–175].

Advancing from clusters to extended systems, the localization of excess electrons at the ice surface was explored in several recent theoretical studies [176–178]. In these studies, molecular dynamics techniques were usually applied. These techniques are suitable for following the dynamics of a localized electron state. However, a systematic approach directly comparing different possible localization sites that are likely to occur at real ice surfaces [85] is still missing. The results presented here are a step in this direction.

We investigate the localization of an excess electron at the basal plane surface of hexagonal ice Ih by performing gradient-corrected density functional theory calculations (DFT-GGA). In order to account for spurious self-interaction effects that artificially delocalize the excess electron, the DFT wave functions are used as input for a partial self-interaction correction (SIC) scheme [44]. Essentially, the excess electron's potential is corrected for self-interaction, whereas the remaining electrons are treated on the usual DFT basis. In the previous chapter we investigated the charge neutral ice Ih(0001) surface and found water monomer adsorption on several non-crystallographic surface sites to be favorable (see also Ref. [85]). Starting from these geometries, we find localization of an excess electron at surface adsorbed water molecules that is significantly more pronounced than on the ideally terminated ice basal plane.

5.1 Self-interaction correction

Describing localized excess charges within DFT poses an inherent problem: In contrast to Hartree-Fock (HF) calculations, the electronic self-interaction in the Hartree and the exchange-correlation contributions to the total energy do not cancel each other. This is a problem of all available approximations to the exchange-correlation energy $E_{xc}[n]$. The remaining self-interaction leads to spurious delocalization of the electronic wave function. While it is possible to perform HF-type calculations, these are computationally very de-

manding and neglect electronic correlation effects. SIC schemes [35, 44] (almost) correct the error in the exchange-correlation functional, but lead to an orbital-dependent Hamiltonian, and thus to a complicated variational principle problem that may impose technical difficulties to solve.

A partial SIC scheme that applies only to the excess electron appears as an affordable yet sufficiently accurate alternative, since the neutral system of interest (hydrogen bonded ice) is well described within DFT, see section 3.2, while the self-interaction error is largest for the localized excess charge. In a system of $2N+1$ electrons, we therefore solve

$$\{T_e + V_{\mathrm{KS}}[n]\}\,|\phi_{i\sigma}\rangle = \varepsilon_i|\phi_{i\sigma}\rangle, \quad i = 1,\ldots,N;\ \sigma = \alpha,\beta \tag{5.1}$$

$$\{T_e + V_{\mathrm{KS}}[\tilde{n}]\}\,|\phi_{\mathrm{N+1},\sigma}\rangle = \varepsilon_{\mathrm{N+1}}|\phi_{\mathrm{N+1},\sigma}\rangle, \tag{5.2}$$

where $n(\mathbf{r})$, $\tilde{n}(\mathbf{r})$ as defined by

$$n(\mathbf{r}) = \sum_{i,\sigma} f_{i\sigma}|\langle \mathbf{r}\,|\,\phi_{i\sigma}\rangle|^2, \quad \tilde{n}(\mathbf{r}) = \sum_{i,\sigma}^{N}|\langle \mathbf{r}\,|\,\phi_{i\sigma}\rangle|^2, \tag{5.3}$$

are the total and paired-electron densities, respectively, and $V_{\mathrm{KS}} = V_{en} + V_H + V_{xc}$ is the total Kohn-Sham potential given as a functional of these densities. The above equations (5.1), (5.2) can be derived from the modified energy functional

$$\begin{aligned} E[\{\phi_{i\sigma}\}] &= E_0[\{\phi_{i\sigma}\}] - E_H[n_{ex}] - \int d^3\mathbf{r}\, n_{ex}(\mathbf{r})(V_{xc}(\mathbf{r}) - \tilde{V}_{xc}(\mathbf{r})) \\ &\quad + \int d^3\mathbf{r}\, n_{ex}(\mathbf{r})\,(V_{\mathrm{KS}}[n(\mathbf{r})] - V_{\mathrm{KS}}[\tilde{n}(\mathbf{r})]) \end{aligned} \tag{5.4}$$

by variation with respect to $\langle\phi_{i\sigma}|$. There, $E_0[\{\phi_{i\sigma}\}]$ is the DFT total energy functional (2.59), evaluated using the eigenvalues and -functions from (5.1), (5.2), and the remaining terms correct for self-interaction contributions in the various parts of $E_0[\{\phi_{i\sigma}\}]$. $V_{xc}(\mathbf{r}) = \delta E_{xc}/\delta n(\mathbf{r})$ and $\tilde{V}_{xc}(\mathbf{r}) = \delta E_{xc}/\delta\tilde{n}(\mathbf{r})$ denote the exchange-correlation potential of the total and paired-electron density, respectively. $n_{ex}(\mathbf{r}) = n(\mathbf{r}) - \tilde{n}(\mathbf{r}) = |\langle \mathbf{r} \mid \phi_{\mathrm{N+1},\sigma}\rangle|^2$ is the excess charge density in the system. This approach was initially inspired by a similar scheme by Mauri *et al.* [44] that calculates SIC based on the magnetization density, which is assumed to be equal to the density of the unpaired elec-

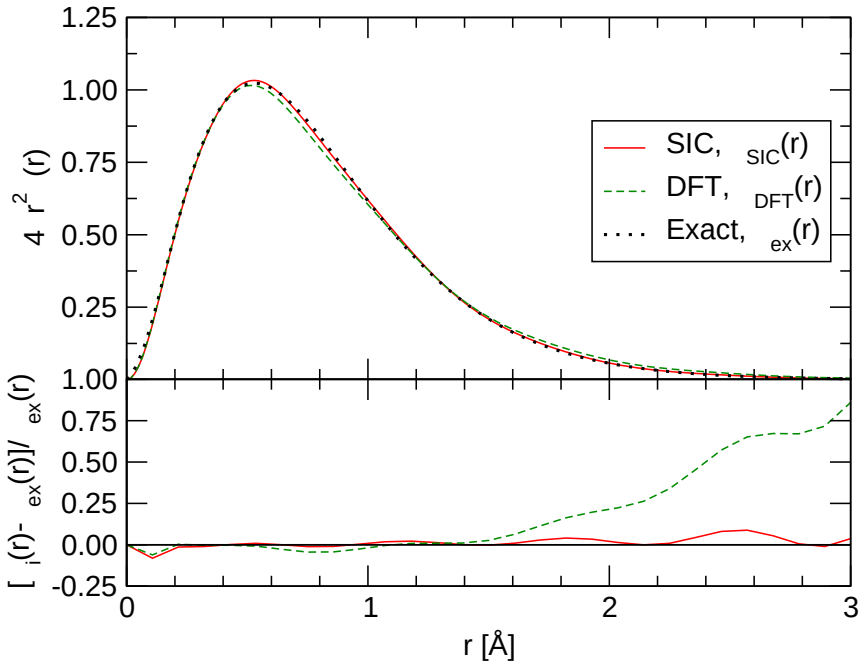

Figure 5.1: Upper panel: Radial charge density $4\pi r^2 \varrho(r)$ of hydrogen atom, calculated in DFT and with partial SIC scheme (see text), and compared to exact solution; lower panel: relative deviation of DFT and SIC density from exact result.

tron. However, it is more closely related to an earlier work by Lundin *et al.* [179] who applied the scheme described above to correct self-interaction of $4f$ electrons in atomic calculations.

5.2 Computational Details

The partial SIC scheme was implemented in the Vienna Ab-Initio Simulation Package (VASP) [105]. Due to the non-hermicity of the Hamiltonian, none of the default iterative matrix diagonalization techniques implemented in VASP [180–184] could be used. Instead, a single-band solver using the conjugate gradient method had to be employed. Subspace rotations to orthogonalize the KS orbitals also had to be switched off. For these reasons, eqs. (5.1), (5.2) are not solved self-consistently. Rather, starting from the optimized DFT wave functions, *one* SIC iteration is performed to obtain an updated wave function. A plane wave basis (kinetic energy cutoff of 15 a.u.) is employed

in conjunction with ultrasoft pseudopotentials to model the electron-ion interaction. Implementing the partial SIC scheme for the PAW method also supported by VASP would have been too difficult, mostly because of the handling of the atom-centered augmentation charges when summing up the paired electron density. The total energy expression (5.4) was implemented to determine the binding energies of the excess electron. The electronic exchange and correlation effects are described by the PW91 functional [40]. Bulk ice vacancy defects are modeled in a series of super cells with up to 128 molecules per cell. Surface calculations of the ice Ih(0001) basal plane are performed using repeated slabs consisting of four ice bilayers, that are separated by a vacuum equivalent of eight bilayers (about 28 Å). There, and in the bulk calculations, the zero wave vector term of the Ewald contribution to the total energy is neglected. That corresponds to introducing a spatially uniform positive background charge that neutralizes the cell. While this removes the divergence of the electrostatic energy of the system, a spurious interaction between the excess and the background charge is introduced, that vanishes only in the limit of infinite supercells. Analytic correction formulae for this interaction energy have been proposed and implemented [185], however, their applicability is currently under discussion [186, 187]. Their influence on the accuracy of the results could only be assessed by extrapolating from a series of calculations, which currently exceeds our computational capabilities, to infinite cell size. A dipole correction scheme prevents long-range interaction between surface slabs arising from surface dipole moments. Surface periodicity is 2×2; reciprocal space integrations are performed at the Γ point only.

As a test the partial SIC scheme is applied to the hydrogen problem. For $N = 0$ paired electrons, the scheme completely removes the Hartree- and XC-potential from the Hamiltonian. Only the electron-ion interaction (modelled by a DFT pseudopotential) remains. The resulting radial charge density is plotted in Figure 5.1 and compared to DFT-GGA and the exact result. The artificial delocalization of the DFT charge density is corrected for by the self-interaction correction. Remaining deviation from the exact solution are most probably due to the finite box size and the use of an ultrasoft pseudopotential.

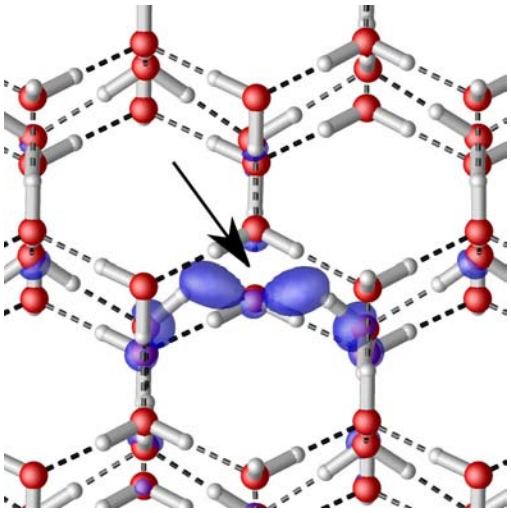

Figure 5.2: Excess electron density at bulk vacancy (located at arrow point). Isosurface value $\varrho_{iso} = 0.03e/\text{Å}^3$.

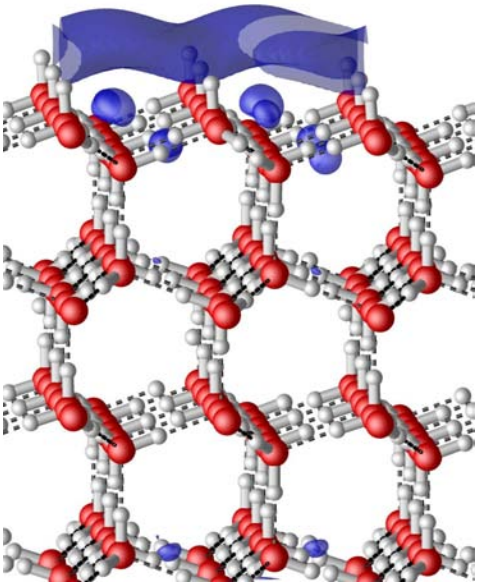

Figure 5.3: Excess electron density at ideal bilayer-terminated surface. Isosurface value $\varrho_{iso} = 0.03e/\text{Å}^3$.

5.3 Excess electron calculations

We start the calculations by considering bulk hexagonal ice Ih with vacancy defects. As shown in Figure 5.2, an excess electron can localize at bulk vacancy sites at dangling OH bonds, occupying $4a_1$-like LUMO states. It is to be expected that it could localize even better at a vacancy that has four inward pointing OH bonds, similar to interior localization sites in water clusters, or liquid water. However, it is not possible to construct a crystalline super cell that, aside from this defect, obeys the ice rules [64] everywhere else; a compensating second vacancy defect or a combination of Bjerrum defects [188] would have to be introduced. Calculations of such systems were not performed here, as it is considered unlikely that fast electron solvation, on a timescale of 0.2 ps [164], facilitates formation of such defect combinations, with defect migration times of tens of picoseconds [189]. However, the formation of Bjerrum defects [190] was found to facilitate *ionic* charge localization: a recent theoretical study found simultaneous solvation of anions

and cations in ice enhanced by common L and D defects (where zero or two hydrogen atoms are situated between adjacent oxygen atoms) [91].

At the ideal bilayer-terminated surface, a scenario similar to the bulk vacancy occurs: Excess electrons occupy $4a_1$-like LUMO states of surface water molecules. However, contrary to the bulk vacancy site, no localization occurs laterally, i.e., in the surface plane between the upward pointing OH groups as shown in Figure 5.3. The binding energy of the excess electron is 0.69 eV. Recently it was found, however, that the formation of rough ice surfaces terminated with single water monomers and dimers is energetically favored, see Ref. [85] and section 4. Other experimental studies found abundant presence of dangling OH bonds at the ice surface [147] and ice surface disorder increasing with temperature, before formation of a quasiliquid layer [191]. Therefore we also explore the localization of excess electrons at rough surfaces.

Figure 5.4 shows the excess electron density along with the in-plane averaged density $n_{ex}^{avg}(z)$ plotted along the surface normal direction for some of these surface structures. In all investigated cases, the excess electron localizes at the surface. Furthermore, in agreement with the results above, it preferentially localizes at dangling OH bonds. Therefore, on a rough ice surface, an excess electron should be expected to be confined laterally as well. The localization perpendicular to the surface plane is by and large independent of the detailed surface geometry; a slightly increased localization can be found on isolated dangling OH bonds (see Figure 5.4(b)) and for larger adsorbate complexes, where the localization sites are farther away from the ideal bulk (see Figure 5.4(d)). Binding energies range from a slightly non-binding scenario (localization at co-adsorbed water's LUMO, cf. Fig. 5.4(c)) to at most 1.11 eV (localization at surface vacancy, cf. Fig. 5.4(a)). Ionic relaxation of the surface region was not included in the present study. However, it should be expected that any atomic relaxation in response to the excess electron should enhance rather than weaken its localization and increase its binding energy. Moreover, since the local rearrangement of hydrogen bonds is easier at the surface than in the bulk crystal, we expect the self-trapping of excess electrons in unoccupied ice surface states to be more effective than in the bulk.

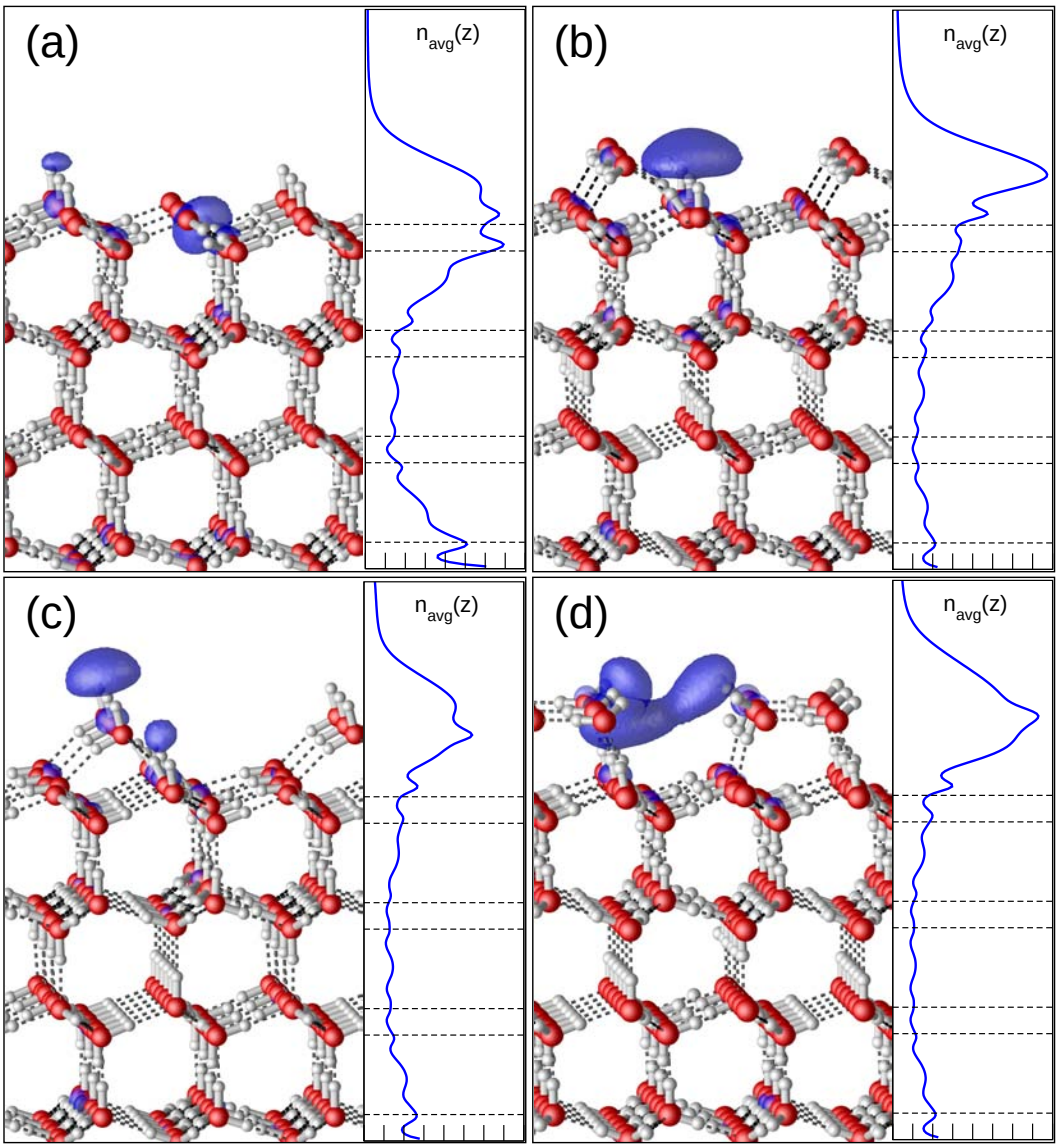

Figure 5.4: Excess electron density at various surface defect sites. Plotted are charge densities ($\varrho_{iso} = 0.03e/\text{Å}^3$) and laterally averaged densities $n_{avg}(z)$. Surface defects, with electron binding energy: (a) surface vacancy, $E_b = 1.11$ eV, (b) and (c) water monomer adsorbed surfaces, $E_b = 0.08$ eV and $E_b = -0.06$ eV, and (d) water dimer adsorbed surface, $E_b = 0.04$ eV; all per 2×2 surface cell.

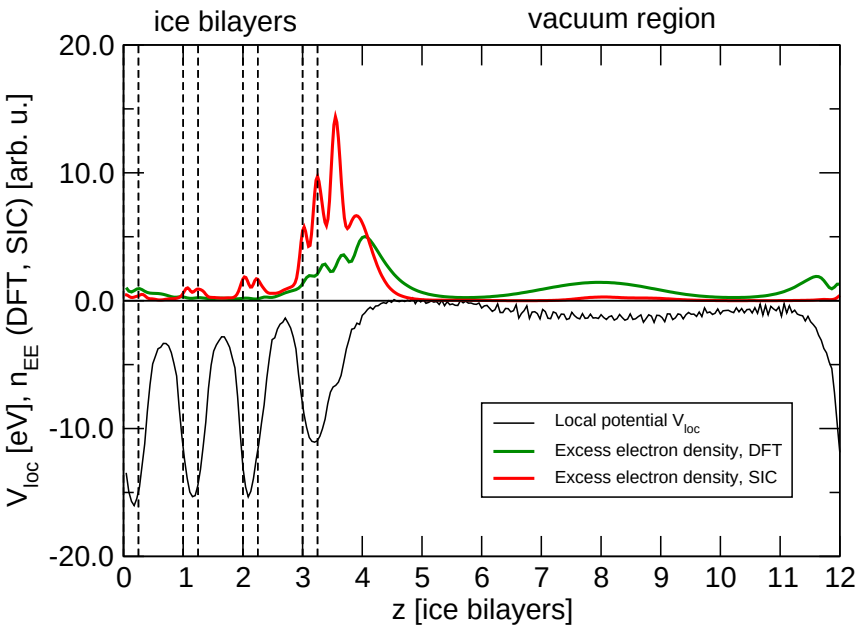

Figure 5.5: Side view on slab cell: comparison of excess electron density from DFT and SIC calculations. Local potential from DFT calculation is also given; dashed lines indicate positions of ice bilayers.

5.4 Discussion

The results above show that excess charges in aqueous systems prefer to occupy LUMO-like states at dangling OH bonds of water molecules. The presence of these in ice bulk vacancy sites or in various ice surface terminations allows for electron localization even in these rigidly hydrogen-bonded systems. The application of SIC leads to an increased localization compared to DFT results in all cases studied. For some configurations, SIC is necessary to achieve a physical solution; see Figure 5.5, where we compare the in-plane averaged charge densities of the excess electron for one of the ice surface terminations, as arising from the DFT and the SIC calculations. In DFT, the excess electron is smeared out in the vacuum region between adjacent slabs; removing its self-interaction then leads to localization near the surface. Rough surfaces allow for increased lateral electron localization. The degree of vertical localization, along the surface normal, is by and large independent of the detailed adsorbate geometry. In addition, we find the highest electron binding energy for a surface vacancy site that provides several OH dangling

bonds. Localization at an ad- or surface molecule's OH group is found to be energetically much less favorable. The general result that excess charges in ice preferentially localize at the surface confirms recent electron solvation experiments on ice clusters, grown on a Cu substrate [164]. It also suggests that atmospheric reactions that are catalyzed or assisted by ice surfaces may often take place in a charged environment. Provided the underlying ice surface is ionized, e.g., by cosmic radiation, uptake and reaction mechanisms of atmospheric molecules may differ significantly from commonly studied neutral ice substrates [160, 178, 192]. Recent interpretations of atmospheric data see the role of charge-assisted heterogeneous reactions in ozone depletion differently [193–195]; however, our findings that realistic models of the ice surface provide a variety of electron localization sites should justify further experimental and theoretical studies on these systems.

One can enjoy a rainbow without necessarily forgetting the forces that made it.

Mark Twain

6

The optical spectrum of water and ice

In this chapter, the optical absorption of small water clusters, water chains, liquid water, and crystalline ice is analyzed computationally. Two competing mechanisms are identified that determine the energy of the optical absorption onset: electronic transitions involving "surface" molecules of finite clusters or chains cause a redshift upon molecular aggregation compared to monomers. At the same time, a strong blueshift is caused by the electrostatic environment experienced by water monomers embedded in a hydrate shell. Regarding the recent dispute over the microscopic structure of the liquid state of water, the present results support the conventional fourfold coordinated structural model of water, as obtained from *ab initio* molecular dynamics simulations.

6.1 Water's Optical Absorption Anomaly

Understanding the excited state properties of water in its many phases is fundamental to research in fields as diverse as corrosion, cellular biology, and atmospheric chemistry. For instance, without UV protection from the ozone layer, liquid water offers little protection against UV damage to marine life, as radiation penetrates liquid water far into the vacuum UV region near the surface. At the same time, UV penetration into liquid water would allow for increased mutation rates of marine organisms, and play a part in the evolution of life. The onset of optical absorption is blueshifted (i.e., shifted to higher energies) in liquid water and ice, as compared to water molecules in the gas phase. The lowest absorption peak shifts from the gas phase value of 7.4 eV (λ=168 nm) to 8.2 eV (151 nm) for liquid water and to 8.7 eV (143 nm) for ice (in its hexagonal, cubic and amorphous phase) [196–199]. Figure 6.1 gives a compilation of experimental results, taken from Ref. [197]. The figure illustrates the blueshift of the absorption onset upon condensation, an effect which seems counter-intuitive. Typically, upon condensation of molecules a transition from molecular energy levels to dispersive energy bands occurs, which reduces the gap between occupied and empty electronic states. As a result, the optical absorption is expected to redshift (i.e., shifted towards lower energies) for the condensed phases, as compared to the gas phase. Explaining, and even reproducing, this anomalous behaviour of water has been a longstanding quest for theoretical scientists.

Not only are the electronic and optical properties of water intriguing, there are also interesting questions concerning the structural properties of its ubiquitous liquid phase. A recent X-ray absorption (XA) study [10] indicated that the widely replicated 100-year-old picture of the structure of liquid water might, in fact, be wrong. Until recently practically all state-of-the-art molecular dynamics (MD) calculations (see, e.g., [200, 201]) supported the theory that hydrogen bonds pulled liquid water into an extended network, with each water molecule bonded to four others. The recent synchrotron results suggest that many water molecules are, in fact, bonded to only two neighbors. The XA spectral features near the energy of the oxygen 1*s* state were found to be similar not to *bulk* ice, but more to the *surface* of ice [10]. In the latter, a water molecule would clearly have about two neighbours on average,

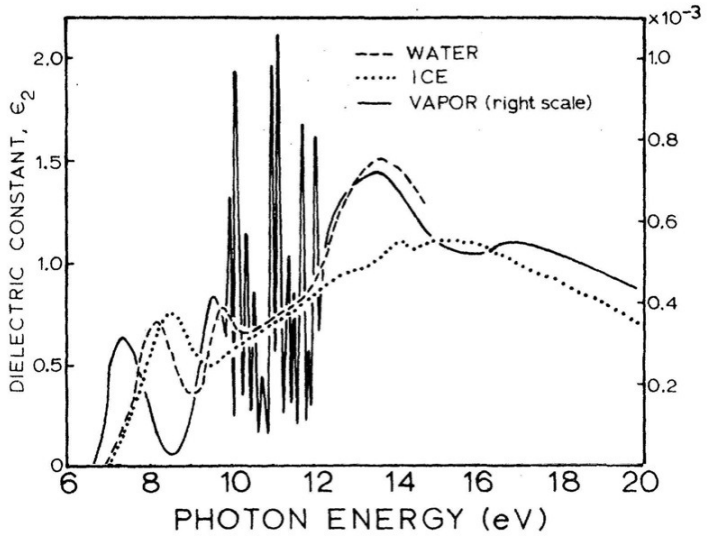

Figure 6.1: Experimental absorption spectra of water in its three phases, from [197]. Lowest absorption peaks in vapor (water, ice) are at 7.4 (8.2, 8.7) eV.

whereas in the former each water molecule has four nearest neighbours.

Standard experimental approaches to analyze the crystal structures (X-ray and neutron diffraction) can provide detailed information on ordered phases of ice, but only indirect, and often limited, information on amorphous ice and liquid water. On the theoretical side, classical and *first principles* molecular dynamics simulations based on density functional theory (DFT) have been used extensively to study water and solvation processes, see, e.g., Refs. [202,203]. However, it is not yet fully understood how accurate the various gradient-corrected functionals in DFT describe the structural and diffusive properties of liquid water [204–206]. Furthermore, the quantitative influence of the inclusion of proton quantum effects in *ab initio* simulations remains to be established. Therefore, methodologies that solely depend on computational data may have difficulties in reliably determining the structural properties of liquid water. In these circumstances, the comparison of spectroscopic data such as the optical response with fingerprints calculated for structural candidates may be of value.

Remarkably, a recently calculated optical absorption spectrum of liquid water deviates significantly from experiment. Coincidentally quite close to

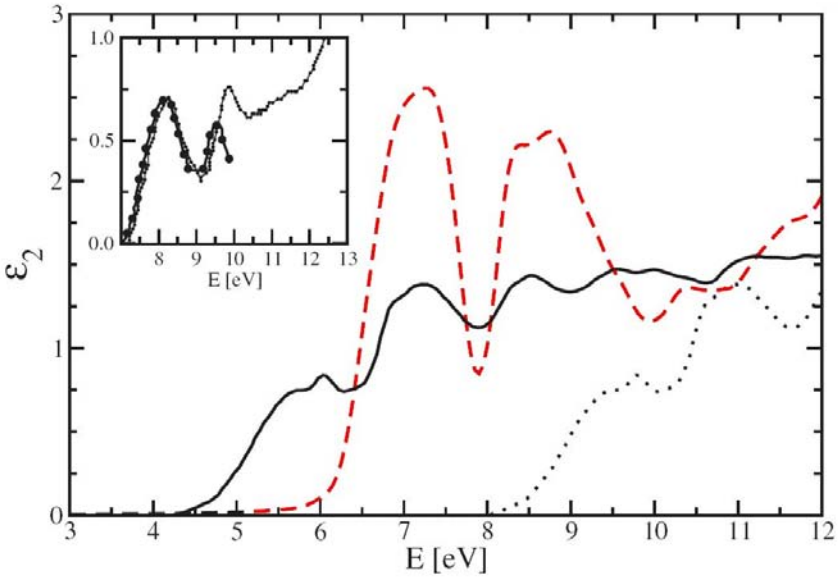

Figure 6.2: Calculated optical absorption spectrum of liquid water, from Ref. [207]. Solid line: DFT absorption spectrum; dotted line: DFT+GW quasi particle spectrum; red dashed line: excitonic spectrum, with first peak at 7.3 eV. Inset shows experimental absorption data, from Refs. [197, 208].

the first absorption peak of gas phase molecules, the calculated onset of the optical absorption occurs at about 7.3 eV, see Figure 6.2. The spectrum was obtained by solving the Bethe-Salpeter equation for a variety of structural snapshots obtained from classical periodic boundary condition MD simulations of liquid water (see Ref. [207] for details). The calculations included excitonic effects. As *first principles* calculations for the water molecule [209] and crystalline ice Ih [210] reproduce the measured optical absorption peaks well, this discrepancy could be indicative of the failure of the standard, tetrahedral model of liquid water. Whereas the latter is supported by recent MD simulations with an *ab initio* based force field [75], calculations of XA spectra were interpreted to support either the tetrahedral model [211, 212] or twofold bonding configurations [213, 214].

In this work, the impact of the coordination and the electrostatic environment on the excited-state properties of hydrogen-bonded water monomers is analyzed in detail. We investigate small water clusters, chains of water molecules, solid ice as well as liquid water obtained from *ab initio* MD sim-

ulations. Two competing mechanisms are identified that considerably shift the excitation energies of hydrogen-bonded monomers compared to single molecules: A redshift is caused by "surface" effects for undercoordinated structures, while the local electric fields of neighboring molecules shift the spectrum to higher energies (blueshift). The optical response calculated for *ab initio* liquid water agrees remarkably well with experiment.

6.2 Computational Details

6.2.1 Ground state properties

Structural properties of crystalline ice and water clusters are optimized using DFT with a plane-wave basis and the projector augmented wave (PAW) method [104] as implemented in the Vienna Ab-initio Simulation Package (VASP) [105, 106]. Computational details are similar to those introduced in section 3.2. Specifically, hexagonal ice Ih is calculated, the hydrogen disorder of which is accounted for by using a 12 or 16 molecule super cell [84, 93]. The plane wave cutoff energy is 15 a.u., and a special k-point set is used to approximate Brillouin zone integrations. Small water clusters are placed in the center of a super cell large enough to avoid spurious interaction between the cluster and its repeated images. A box size of $20 \cdots 28$Å was chosen and found to suffice for all cluster calculations. The Brillouin zone for all cluster calculations is sampled using the Gamma point only. All ionic and (in case of the crystal) unit cell degrees of freedom are optimized such that the remaining forces on the atoms are below 5 meV/Å. The DFT exchange-correlation energy is described using the PW91 functional [40], as it reasonably describes hydrogen bonds in crystalline ice, see section 3.2: geometric properties are usually in very good agreement with experiment, even though the binding energy at least in crystalline ice is overestimated significantly.

Ab initio MD simulations are performed using VASP: a 64 molecule super cell is constructed such that it has the mass density of water at room temperature: $\varrho = 0.99707\text{g/cm}^3$. The ionic kinetic energy is normalized to correspond to a temperature of $T = 298$K. Pre-optimized liquid water from a classical MD simulation using the TIP4P pair interaction potential [71] serves

as input for an *ab initio* equilibration; structural snapshots are then obtained every 200 fs from a 4 ps production run. *Ab initio* water MD simulations as suggested in chapter 3 are not feasible yet. The quality of the "DFT-MD water" used here, i.e. its agreement with the real liquid on the microscopic level can thus not be assessed directly. As mentioned above, however, the comparison of calculated observables (like optical excitation spectra) with experimental data is a valuable option to evaluate the theoretical methods used.

6.2.2 Excited state calculations

Based on the ground state DFT calculations, optical absorption spectra are calculated, including many-body effects. Depending on size and dimension of the system, this is done either by performing GW and Bethe-Salpeter (BSE) type calculations [215], occupation-constrained DFT (ΔSCF) calculations in VASP, or wave function based symmetry-adapted cluster configuration interaction (SAC-CI) calculations using GAUSSIAN03 [31, 216].

Green's function method for optical spectra of ice

The Green's function formalism is used for infinite chains and bulk ice, utilizing the implementation outlined in Refs. [62, 209], and described here in more detail.

The electronic self energy is calculated in the GW approximation, as outlined in section 2.5.3. As described there, the self energy operator Σ is not calculated self-consistently, but instead in a "one-shot" iteration $\Sigma = G_0 W_0$ from the DFT-derived quantities G_0 and W_0. The self energy Σ is then treated as a perturbation of the Kohn-Sham Hamiltonian, and the quasi-particle energies are obtained from equation (2.105). The computationally most expensive part in the calculation of the screened interaction W_0 is determining the inverse of the microscopic dielectric function $\epsilon_0^{-1}(\mathbf{q}, \omega)$ at every frequency value ω. However, $W_0 = \epsilon_0^{-1} v$ contains an integral over all frequencies, so that the details of the frequency dependence of $\epsilon(\mathbf{q}, \omega)$ are not expected to be important. For those reasons, $\epsilon(\mathbf{q}, \omega)$ is approximated here by a model

dielectric function [55]

$$\epsilon(\mathbf{q}, n) = 1 + \left[\frac{1}{\epsilon_0 - 1} + \frac{5\mathbf{q}^2}{4q_{TF}^2} + \frac{3\mathbf{q}^4}{4k_F^2 q_{TF}^2} \right]^{-1}, \tag{6.1}$$

that depends via the Fermi wave vector k_F and the Thomas-Fermi wave vector q_{TF} on the local electron density n. Despite being a static approximation, $\epsilon(\mathbf{q})$ from (6.1) gives remarkably good results over a wide range of materials, in part probably due to the fact that it interpolates between the free electron gas for large values of $|\mathbf{q}|$, a Thomas-Fermi like behaviour for small values of $|\mathbf{q}|$, and the static dielectric constant ϵ_0 for $\mathbf{q} = 0$. Another prominent approximation for $\epsilon_0(\mathbf{q}, \omega)$ is the plasmon-pole approximation, where the dielectric function is described by a single peak at a plasmon frequency ω_p [56].

The model dielectric function from (6.1) comes with one adjustable parameter: the static dielectric constant ϵ_0. For all GW and BSE calculations of ice, a constant of $\epsilon_0 = 2.0$ is chosen. Thus we choose ϵ_0 to be close to the high-frequency dielectric constant of ice, which is appropriate considering the energy range and time scales of the electronic excitations that are studied here.

Occupation-constrained DFT for optical spectra of water clusters

The ΔSCF, or occupation-constraint DFT method, allows for calculations of excitation energies at the computational cost of a standard self consistency loop for the ground state. In short, the Kohn-Sham equations (2.64) are solved for a set of occupation numbers $\{f_i\}$ that do not correspond to the ground state, but to a desired excited state, for instance an excitation from the highest occupied into the lowest unoccupied molecular orbital of a molecule. Since the equations (2.64) are solved self-consistently, as usual, all correlation effects between the excited electron and the hole are included in the total energy. The difference between the total energy of the excited state configuration and the ground state energy equals to the excitation energy. Transition dipole moments are calculated from the ground state DFT wave functions, i.e. final state effects are not taken into account. The ΔSCF method

is a means to calculate excitation energies of molecules and clusters at the computational cost of a self-consistency step. Each transition, however, has to be treated independently. Occupation constraint DFT is not applicable to excitations in extended systems, due to the usual problem of describing a single electronic excitation within a periodic boundary framework.

For the water molecule and small water clusters, ΔSCF calculations are performed using VASP, and utilizing the geometries obtained as described in the previous section. For excited states, large box sizes are necessary to avoid interaction between the (more delocalized) excited electrons in adjacent super cells. The box sizes mentioned previously were tested for converged first excitation energies.

6.3 Solid state: crystalline ice Ih

For all excited state calculations of ice we use the ground state geometry from DFT calculations, as introduced in section 3.2. In particular, the irreducible orthorhombic part of Morrison's 16 molecule super cell is used: it contains eight water molecules.

See Figure 6.3 for the electronic band structure of ice, obtained both from DFT eigenvalues, and using quasi-particle energies from the perturbative treatment of the electronic self energy in the GW approximation. The valence bands can be matched to the molecular orbitals $1b_2$, $3a_1$, and $1b_1$ they originate from. They show (with the exception of the $3a_1$ bands) little dispersion. In DFT, ice is an insulator with a direct band gap of 5.50 eV at the Gamma point of the Brillouin zone. Quasi-particle energy correction lead to a quasi-rigid shift of the conduction band energies, opening the band gap by about 4.5 eV. The quasi-particle gap of ice is calculated to be 10.12 eV. In Figure 6.4, the quasi-particle energy shifts $\Delta\epsilon_{n\mathbf{k}}$ are plotted versus the corresponding DFT eigenvalues. The $\Delta\epsilon_{n\mathbf{k}}$ depend linearly on the eigenvalues $\epsilon_{n\mathbf{k}}$, however with a gap of about 4 eV between valence and conduction bands. The energy shifts are more irregular for higher energetic conduction bands which correspond to quasi-free electronic states.

The optical spectrum of ice is first calculated on single particle level, from DFT wave functions and eigenvalues. Transition energies and oscillator

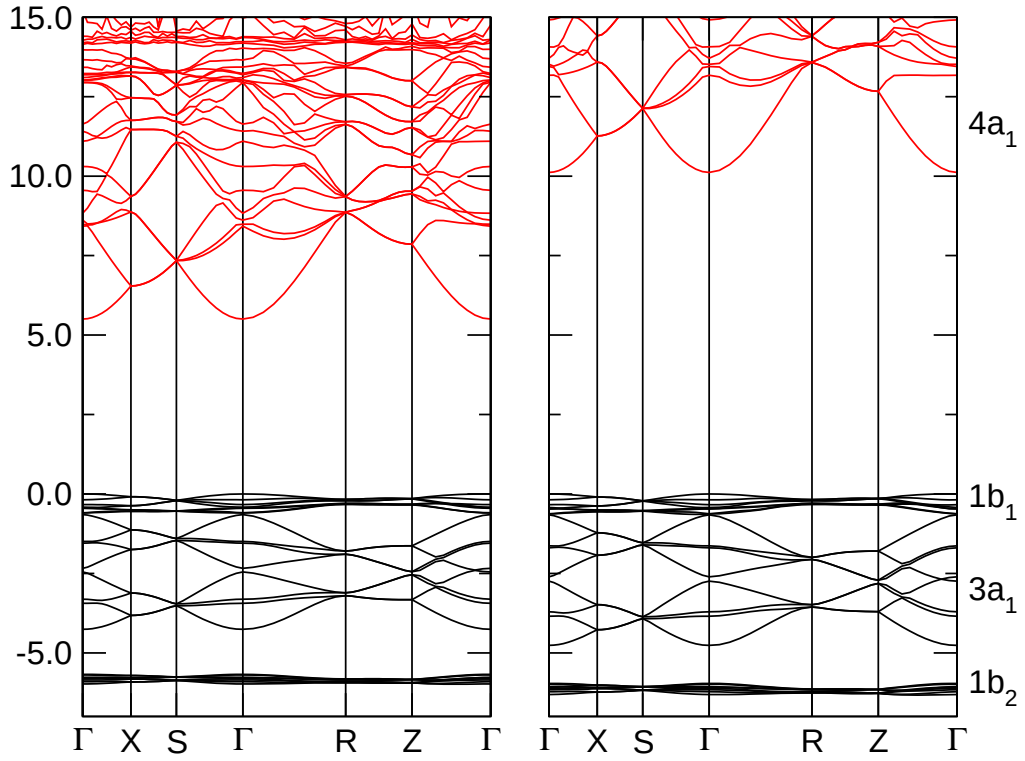

Figure 6.3: Electronic band structure of hexagonal ice Ih: left, from DFT-GGA calculations; right: including quasi-particle energy corrections from GW calculations. Black lines: valence bands; red lines: conduction bands. Energies are in eV, and normalized to valence band maximum energy (the Fermi level ε_F is positioned within the band gap).

strengths are determined for sets of random k-points, which in comparison with ordered k-point sets avoid over-emphasized high-symmetry spectral features, and give spectra which converge monotonously with increased number of k-points towards the dense k-point limit. The spectra are shown in Figure 6.5, which also serves as a benchmark to determine the necessary number of conduction bands and k-points to obtain converged spectra. From Figure 6.5, we conclude that 48 conduction bands (the unit cell has 64 valence electrons, hence 32 valence bands) and 64 random k-points yield a well converged spectrum up to an excitation energy of about 20 eV. Naturally, the spectrum does not agree very well with experimental data: its onset of absorption occurs at about 6 eV, and the dominant first excitation peak is

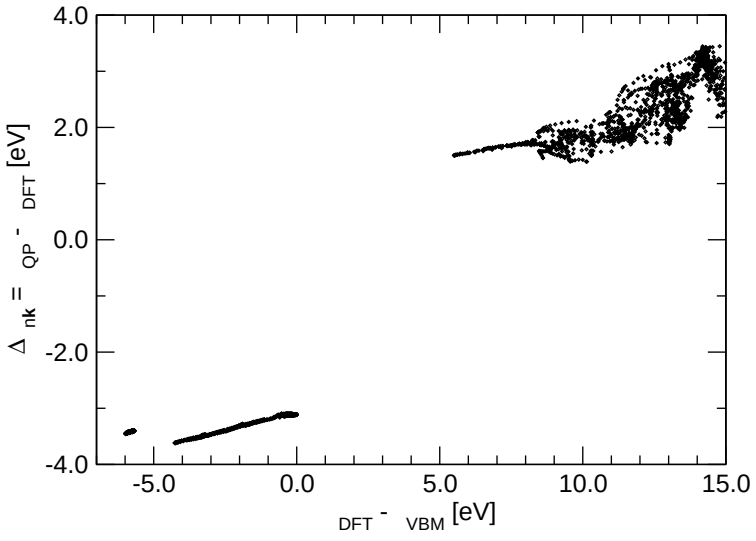

Figure 6.4: Hexagonal ice Ih: quasi-particle energy shifts $\Delta\epsilon_{n\mathbf{k}}$ from GW calculations vs. DFT eigenvalues ϵ_{DFT}, normalized to valence band maximum ϵ_{VBM}.

missing. Instead, the majority of oscillator strength forms a distinct peak at around 14 eV.

To go beyond DFT, it is possible to calculate an optical spectrum using the quasi-particle energies from a GW calculation. The spectra obtained, however, does not go beyond the random phase approximation, and would certainly not improve agreement with experiment. This is only achieved when taking the interaction between excited electron and hole into account, i.e. by solving the Bethe-Salpeter equation. For these calculations, we use the computational parameters determined above from the DFT spectra calculations: 32 valence and 48 conduction bands, and (the same) 64 random k-points. The excitonic Hamiltonian matrix (2.117) thus has a rank of $N = 32 \times 48 \times 64 = 98,304$. However, we restrict the calculation to transitions with a quasi-particle gap of at most 25 eV. That reduces the matrix size to about 70,000 at the equilibrium lattice constant of ice. Solving the initial-value problem for the macroscopic dielectric function is then possible with about 40GB of computer memory.

The spectra obtained from the GW and BSE approach are compiled in Figure 6.6, together with the DFT spectrum and experimental data from

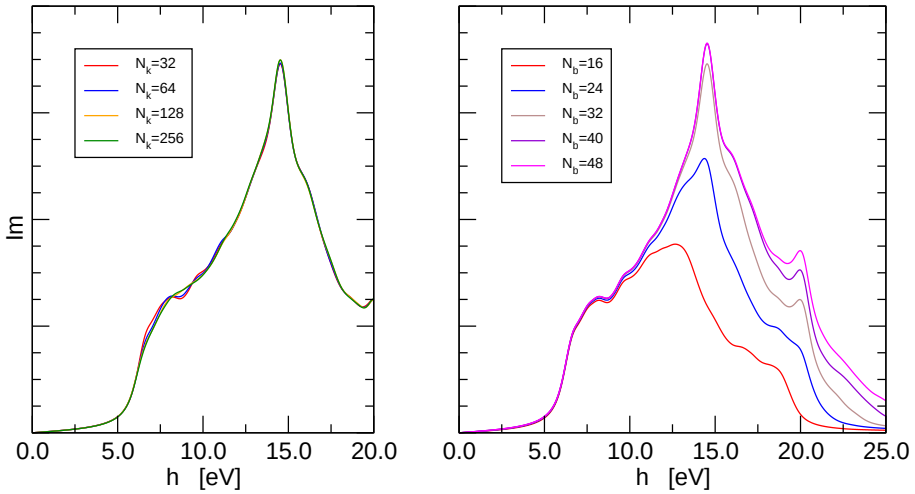

Figure 6.5: Hexagonal ice Ih: single particle spectrum from DFT; convergence tests with respect to number of k-points (left panel, with number of conduction bands $N_b = 32$) and conduction bands (right panel, with number of k-points $N_k = 32$).

Ref. [217]. All calculated spectra are convoluted with a broadening of 0.5 eV. The GW spectrum is basically a blue-shifted version of the DFT spectrum; this is to be expected as the GW quasi-particle correction mainly results in a rigid blueshift of the conduction bands, see Figure 6.3. Agreement with experiment does not improve significantly. Including the electron-hole correlation leads, however, to a spectrum that agrees very well with the experimental data: the excitonic first absorption peak at 8.7 eV, and the subsequent peaks at 10.3 eV, 12.0 eV, and 14.3 eV coincide with the experimental features. Mind that the BSE spectrum is likely to lack oscillator strength in the high energy region, due to the energy cutoff of 25 eV for quasi-particle transition energies. It does, however, reproduce the experimental blueshift of water's absorption onset within experimental uncertainty. Although using a two-particle picture proves essential and valuable in reproducing water's optical spectrum, it inherently leads to a breakdown of the one-particle picture of "occupied state", "excited state", and transition energies involved. It is thus much more difficult to dissect the spectral features. A recent work [210] interpreted ice's blueshift in terms of delocalization of the bound exciton between excited electron and hole in the crystal, thus leading to a reduced excitonic

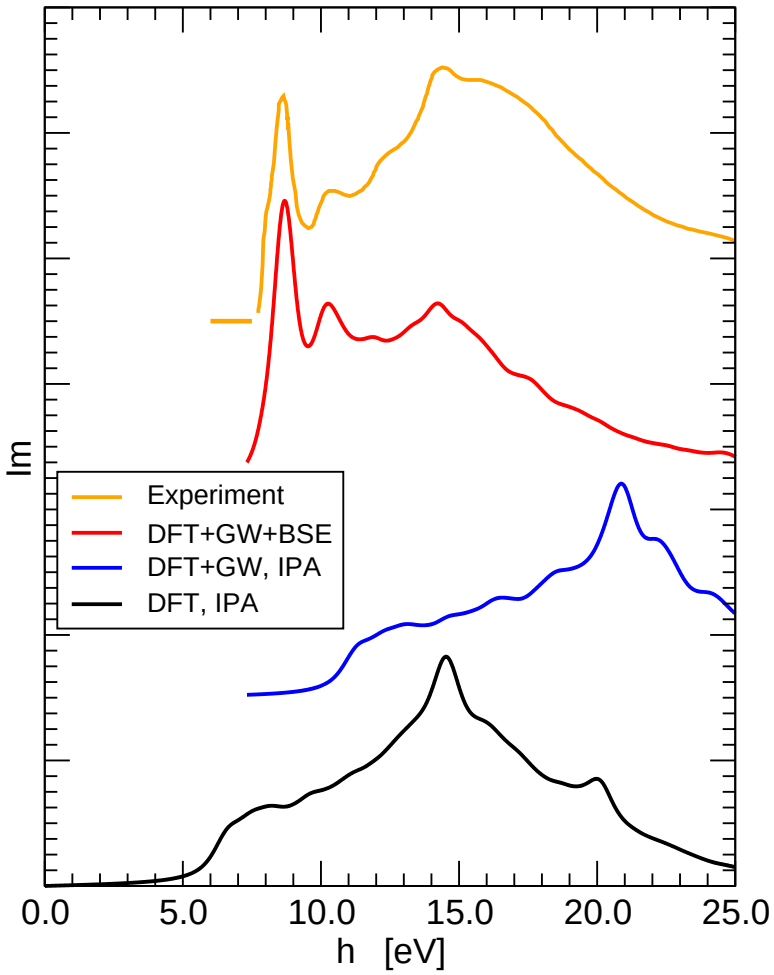

Figure 6.6: Hexagonal ice Ih: Optical absorption spectrum calculated by DFT, DFT+GW, and DFT+GW+BSE, and compared to experiment, from [217].

binding energy compared to the gas phase molecule. This would then cause a blueshift of the excitonic absorption peak. After discussing the optical spectra of gas phase water cluster structures in the next section, we introduce a model system that not only reproduces ice's optical spectral features but also allows for much easier interpretation of the spectral features.

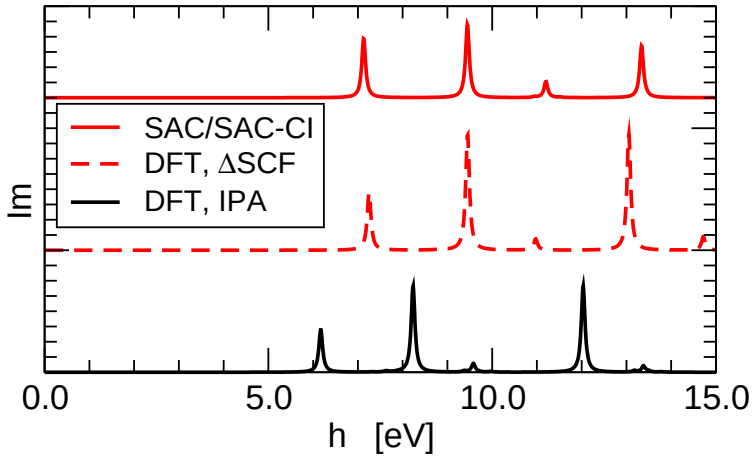

Figure 6.7: Water molecule in the gas phase: Optical excitation spectrum, calculated from various methods.

Excitation	DFT	ΔSCF	SAC-CI	Experiment
$1b_1 \rightarrow 4a_1$	6.16 (0.007)	7.25	7.13 (0.049)	7.4 (0.050)
$3a_1 \rightarrow 4a_1$	8.22 (0.026)	9.45	9.45 (0.107)	9.7 (0.073)
$3a_1 \rightarrow 2b_2$	9.64 (0.003)	10.97	11.20 (0.033)	
$1b_2 \rightarrow 4a_1$	12.02 (0.055)	13.05	13.34 (0.149)	

Table 6.1: Water molecule: Excitation energies (in eV) and transition dipole moments in brackets (in a.u.), from various methods and experiment [218]. ΔSCF transition dipole moments are the same as obtained from DFT.

6.4 Gas phase: water molecule, clusters, and infinite chain

For the water molecule in the gas phase, ΔSCF calculations using VASP are compared to SAC-CI calculations using GAUSSIAN03 [216]. The latter use augmented correlation consistent valence double-zeta basis sets [125]. The ΔSCF method allows for the calculation of optical spectra over the whole desired energy range, whereas the SAC-CI calculations had to be restricted to solving the CI secular equations for the 20 lowest excitations. The different approaches account comparably for self-energy and excitonic effects: While DFT predicts the optical gap of the water monomer at 6.16 eV, we obtain 7.24 eV from ΔSCF, and 7.15 eV from SAC-CI, both close to the experimental

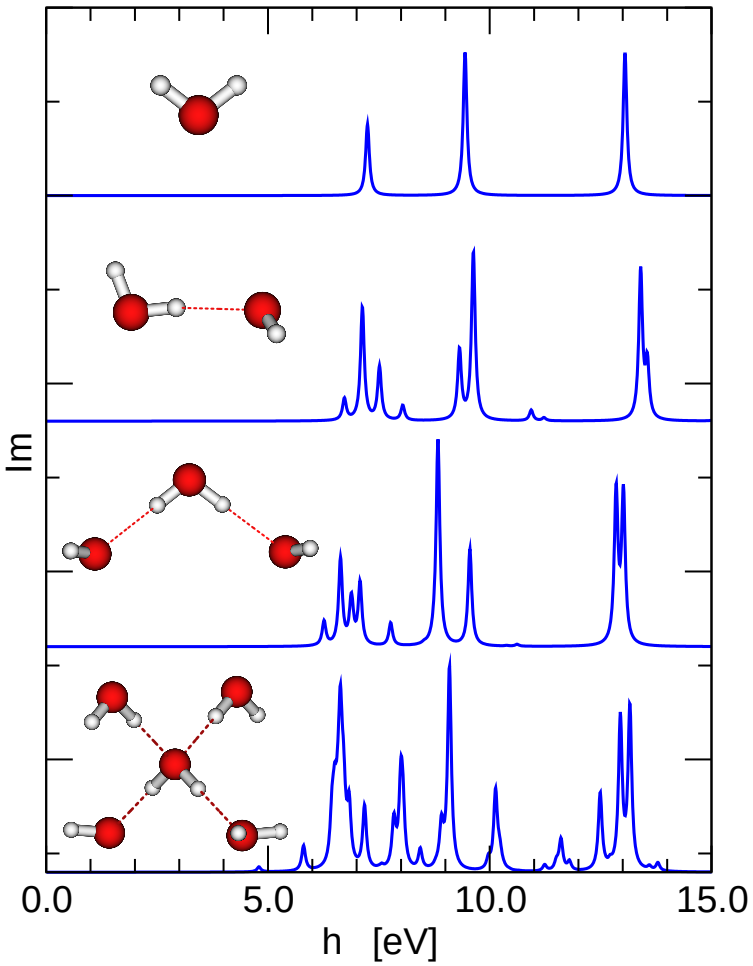

Figure 6.8: Optical absorption spectra of small compact water clusters (see structures on the left), from ΔSCF calculations.

value of 7.4 eV. Figure 6.7 compiles these spectra: not only compare the excitation energies of SAC-CI and ΔSCF very well, but also the relative oscillator strengths are in good agreement. Table 6.1 lists the excitation energies and transition dipole moments that were used to produce the spectra of Figure 6.7. The good agreement of occupation constraint DFT not only with high-level quantum chemical calculations but also experimental data justifies its application to computing excitation spectra of larger water clusters. In the literature, a recent EOM-CCSD(T) calculation for the water monomer obtained 7.54 eV for water's first excitation energy [219].

The optical absorption spectra of small water clusters are calculated to

study the effect of molecular nucleation on the absorption onset. It is certainly of interest to explore whether small water clusters already show the interesting feature of the extended phases, an optical spectrum that is blueshifted with respect to the gas phase molecular spectrum. Thus, we study cluster structures that "fill up" the first coordination shell of a water molecule. Going beyond a water pentamer, however, exceeds the computational resources available. The investigated structures are shown in the left panel of Figure 6.8. All structures are (at least local) minima on the respective potential energy surface. The dimer structure is the global minimum, and compares very well to existing data: the OO distance ($r_{\mathrm{OO}} = 2.87$Å), total binding energy ($E_b = 0.24$ eV), and angular deviation from a linear hydrogen bond ($\delta_{\mathrm{HOO}} = 6.6^\circ$) agree well with experiment [220] and quantum chemical calculations [221].

Upon increasing cluster size, the three main excitations of the monomer are split and the absorption onset is redshifted towards slightly smaller energies, see Figure 6.8. In every cluster, the highest occupied (HOMO) and lowest unoccupied molecular orbitals (LUMO) are localized on a hydrogen-bond donating and accepting molecule, respectively. The HOMO-LUMO excitation is an inter-molecular transition that occurs (most clearly for the pentamer $(H_2O)_5$) between cluster surface states. The influence of these surface transitions can be expected to fade with further increased cluster size: spatial separation of the surface molecules and a decreasing surface-to-bulk ratio will contribute to this effect. For the infinite crystal, no surface effects occur. However, this trend is not observed for the (rather small) clusters studied here. The results thus indicate that compact clusters are no suitable model to explain the optical absorption of extended water phases, in particular the shift of the absorption onset to about 8.2 eV (in the liquid phase) and 8.7 eV (in the solid phase).

According to Ref. [10], most molecules of liquid water form hydrogen bonded chains or rings. Thus, the optical response of finite chains up to $(H_2O)_7$ and of an infinite molecular chain are calculated. The geometries of the finite chains could not be optimized (they would revert into smaller ring structures), and were thus kept frozen as cut-out from a crystalline structure. They feature OH bond lengths of 0.975Å and $OH \cdots O$ hydrogen bond

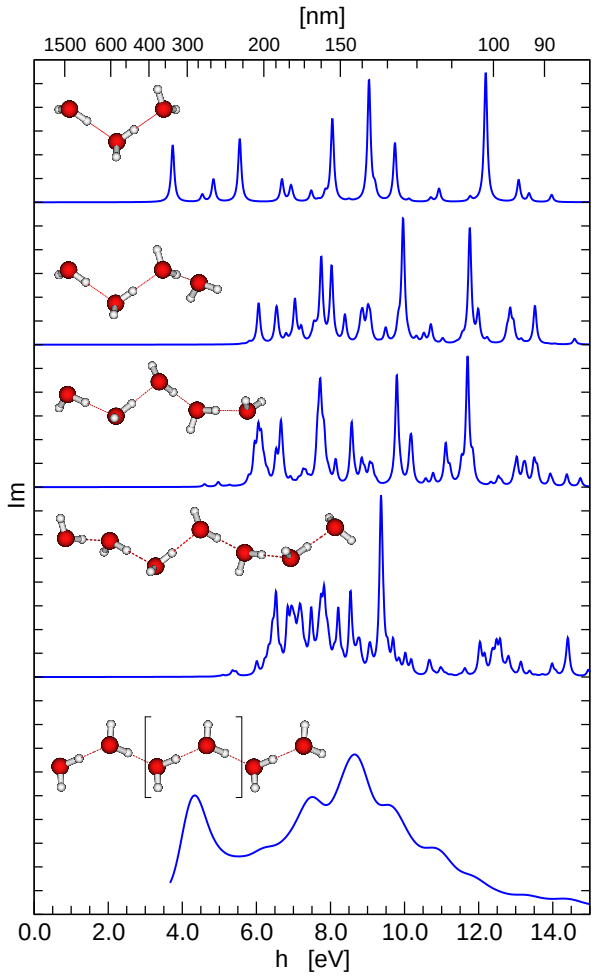

Figure 6.9: Optical absorption spectra of finite and infinite water chains (see structures on left), from ΔSCF and Green's function calculations.

lengths of 1.75Å. The infinite water chain is a 1-D periodic structure, with two molecules in the unit cell. The optical spectra of the finite chains were calculated using VASP and the ΔSCF method; the infinite chain's absorption spectrum was calculated by solving the Bethe-Salpeter equation, and obtaining the macroscopic dielectric function along the chain direction. The spectra obtained are compiled in Figure 6.9, which also contains sketches of the cluster's and the infinite chain's geometries.

Similar to the compact clusters discussed above, the onset of the optical absorption of finite chains is found to occur below the monomer value. How-

ever, the onset is blueshifted with increased chain length. This is the visible result of the spatial separation of HOMO and LUMO (which are localized at opposing ends of the water chain), and thus a quenching of the related optical excitation. But even so, the first absorption band with noticeable oscillator strength occurs at energies below the first monomer absorption energy. For the heptamer chain $(H_2O)_7$, a broad absorption band can be seen between 6.5 eV and 9 eV. This broad band also appears in the many-particle spectrum of the infinite water chain. The latter, however, is dominated by a strong excitonic peak at 4.3 eV, see Figure 6.9. Obviously, chains of under-coordinated water molecules in vacuum are not suitable either to explain the optical response of liquid water.

6.5 Modelling electrostatic interactions in water and ice

The chain and cluster structures studied so far have not proven suitable model systems to connect the gas phase with the extended liquid or solid phases. This is hardly surprising, however: to start with, they do not experience the long-range electrostatic interaction with a surrounding aqueous environment [222]. Including this part of the hydrogen bond interaction with a water cluster calculation would enable one to calculate localized excitations, while also accounting for the dielectric environment. Thus, it would be possible to study separately the influence of local fields and hydrogen bonds on the optical absorption. The electrostatic energy of a water molecule in ice is to more than 90% accounted for by its interaction with surrounding water molecules' dipole moments [223]. Therefore, including the dipole field of the aqueous environment of a water cluster should give a much more realistic model to study extended water phases' optical excitations. This construction does not only consider the electrostatic contribution to the hydrogen bond, but also (at least partially) the orbital delocalization. Other contributions to the total binding energy such as dispersive or closed shell repulsion interactions are, of course, not included; the results presented below justify in retrospect the neglect of these parts of the hydrogen bond interaction. The dipole electrostatic field around a water cluster is constructed by placing

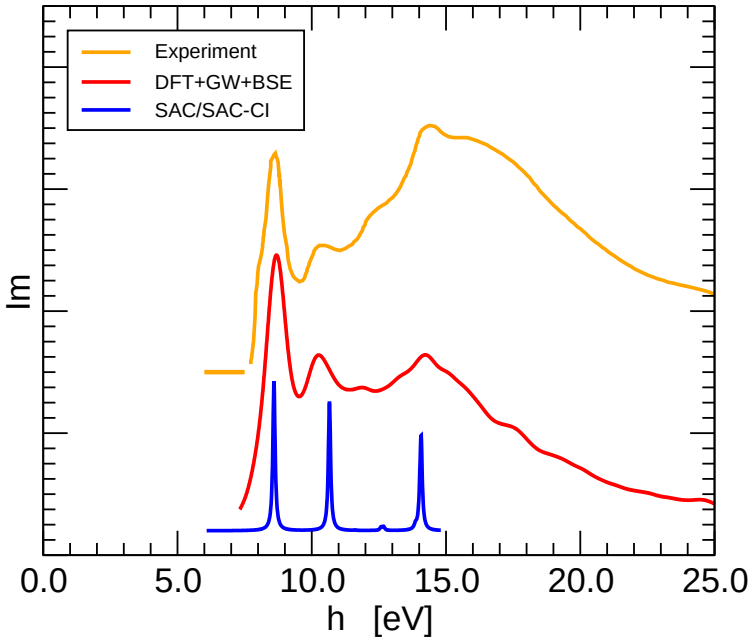

Figure 6.10: Hexagonal ice Ih: Optical absorption spectrum, calculated from Green's function formalism, and from SAC/SAC-CI for water molecule including electrostatic environment. Experiment from Ref. [217].

point charges at the positions of oxygen and hydrogen atoms both of the optimized ice structure and liquid water MD snapshots. Their magnitudes are adjusted to account for the enhanced dipole moment of water in ice [224] and the liquid [225]. The optical spectra of a water molecule or cluster embedded in this way are then calculated.

6.6 Embedded molecule absorption spectra

6.6.1 Crystalline ice spectrum

The local structural environment of a water molecule in crystalline ice is taken from DFT calculations. A spherical cluster of water dipole moments is constructed from this structural information, and placed around a central water molecule or cluster. The optical spectrum is then calculated using the SAC/SAC-CI method as implemented in the GAUSSIAN03 program

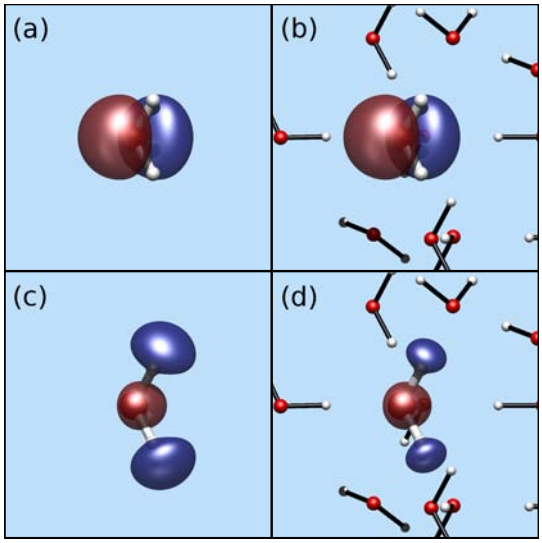

Figure 6.11: Plots of water's single-particle orbitals: $1b_1$ HOMO in (a) vacuum, and (b) ice-like electric field; $4a_1$ LUMO in (c) vacuum, and (d) ice-like electric field. Isosurface value 0.06 a.u. Right column plots also show positions of hydrate shell point charges.

suite [31, 216]. The spectrum of a single water molecule is found to be converged when including the dipole moments of the water molecules of the three closest coordination shells. For the spectra presented here, eight coordination shells of dipole moments were included. In Figure 6.10, the spectrum of the embedded water molecule is compared to the BSE result presented in section 6.3 and experiment. We find excellent agreement with both the sophisticated two-particle calculation and the experimental data. The electric field induced by the surrounding hydrate environment of crystalline ice shifts the absorption onset of the water monomer from 7.2 eV to 8.6 eV, which is in very good agreement with the data available for ice Ih. Excitation peaks at 8.6, 10.8, (12.7) and 14.2 eV also agree very well with the calculated solid state spectrum and experiment.

Figure 6.11 illustrates on the single-particle level the influence of the dipole electrostatic environment on the shapes of molecular HOMO and LUMO: while the $1b_1$ HOMO is almost unchanged (being only slightly delocalized), the $4a_1$ LUMO is significantly quenched upon repulsive interaction with neighboring, hydrogen-bonded molecules. Table 6.2 confirms this trend: single particle orbital energies are listed from both DFT and HF calculations of

	DFT Orbital energies [eV]		HF Orbital energies [eV]	
Molecular Orbital	in vacuum	in dipole field	in vacuum	in dipole field
$4a_1$	-1.28	-0.17	0.94	1.83
$1b_1$	-7.20	-7.41	-13.74	-13.88
$3a_1$	-9.24	-9.27	-15.55	-15.69
$1b_2$	-12.94	-12.44	-18.92	-18.61
$2a_1$	-24.92	-24.67	-36.19	-36.06
$1a_1$	-511.61	-511.39	-560.13	-559.90

Table 6.2: Single particle orbital energies, from DFT and HF calculations, both in vacuum and in crystalline electrostatic field.

a water molecule, both in vacuum and in the electrostatic dipole field of the crystalline ice environment. Although the absolute values of the orbital energies are not helpful in obtaining reasonable values for the optical gap, their shifts under the influence of the dipole electric field certainly illustrate the effect described above – a significant raise in energy for the $4a_1$ LUMO state, and a lowered energy for the $1b_1$ HOMO state. The reason for this effect is the high directionality of the hydrogen bonds in ice, that leads to strong local electric fields that in turn influence the molecular energy levels as decribed above. Since all bound excitations in Figure 6.10 are dominated by single-particle excitations into the LUMO, all are shifted similarly under the influence of the surrounding aqueous environment. It is interesting to note that the blueshift of the optical absorption upon aggregation of water molecules to ice explained by many-body effects in Ref. [210] can thus be understood already in a single-particle picture, provided the local electrostatic environment is taken into account.

The influence of the dipole electric field is corroborated by calculations for a water pentamer cluster (the geometry of which was taken fixed "as is" from the crystalline ice structure) embedded in the crystalline dipole field. The absorption onset of the cluster is shifted from 7.0 eV to 8.7 eV, see Figure 6.12, again very close to the value of crystalline ice. A similar explanation holds here: All low-energy excitations populate the LUMO and LUMO+1 states that are combinations of water's molecular LUMO's; these are quenched similarly under the influence of the aqueous environment. Note that the spectra in Figure 6.8 and Figure 6.12a differ in parts because of the pentamers' differ-

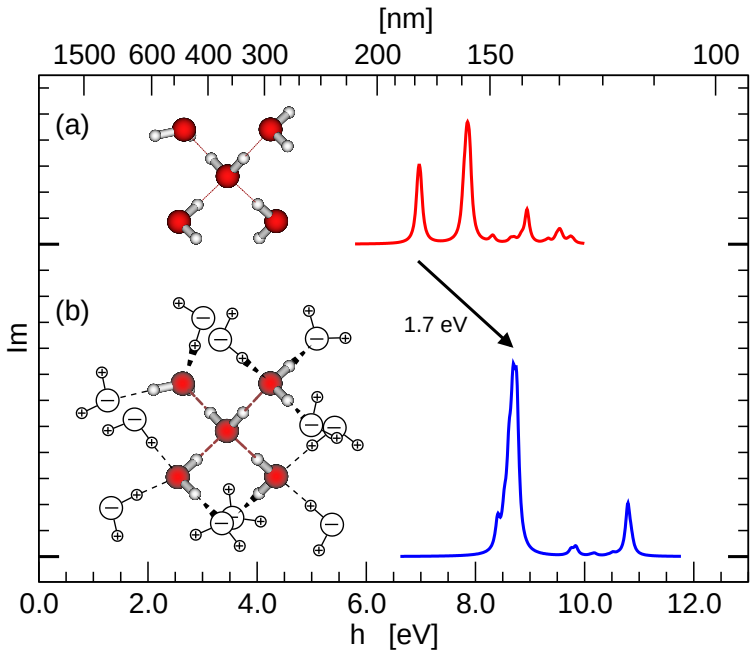

Figure 6.12: Low-energy excitations of a water pentamer (a) in vacuum, and (b) in electric field of surrounding crystalline ice from SAC-CI calculations.

ent structures, but mostly because the SAC-CI method used for the latter is restricted to the 20 lowest transitions. Both spectra feature dominant peaks at 6.5-7.0 eV and 8 eV, but the higher energy region is not accessible to the SAC-CI method.

6.6.2 Liquid water spectrum

Based on the excellent agreement between experiment and the electrostatic embedding calculations for crystalline ice, this methodology is now applied to the *ab initio* liquid phase. The liquid water absorption spectrum is obtained by accumulating spectra of MD snapshot configurations until the spectral features are converged in line shape and position. For each snapshot, 64 absorption spectra are calculated for the 64 individual molecules in the MD supercell. For each of these calculations, all other molecules in the unit cell and in the surrounding unit cells are replaced by their dipole moment (again modelled by point charges at the hydrogen and oxygen atoms' positions). The spectra were found to be converged after averaging over 20 structural

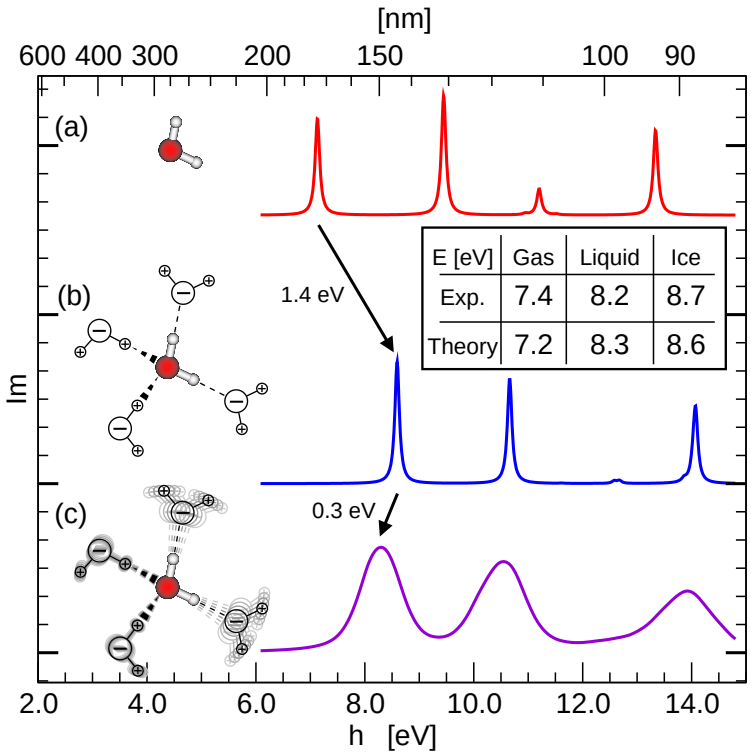

Figure 6.13: Absorption spectra of a single water molecule (a) in vacuum, (b) in electric field of surrounding crystalline ice, and (c) in electric field of surrounding liquid water. Inset compares absorption onset from these SAC-CI calculations with experimental data [196–199].

snapshots. The result is shown in the lower panel of Figure 6.13, where it is also compared to the SAC-CI spectra of a gas phase water molecule, and water in the crystalline electrostatic environment. For the liquid phase, the first absorption peak is redshifted with respect to crystalline ice to 8.3 eV, very close to the experimental value of 8.2 eV. The other main peaks at 10.5 and 13.9 eV are also close to experimentally identified maxima at 10.0 and 13.7 eV [198]. We failed to achieve a similar degree of agreement with experiment on the basis of a two-fold coordinated water molecule embedded in an appropriate electrostatic environment, unless the density of the liquid was drastically reduced (by at least 25%) compared to the experimental value. The excellent agreement of the optical response calculated for the *ab initio* liquid with the measured absorption certainly strongly supports the conventional picture of fourfold coordinated water molecules in the liquid.

This result complements XA spectra calculations which usually probe dipole transitions of a different character [226]. However, given the large number of adjustable parameters, the possibility of alternative structural models for the liquid phase of water cannot be ruled out completely on the basis of the optical absorption data alone, even though we believe that it is most unlikely.

6.7 Conclusions

In conclusion, *first principles* calculations show that the onset of the optical absorption of a network of undercoordinated water monomers in vacuum is redshifted with respect to the monomer excitation. This effect is related to intermolecular transitions involving edge or surface molecules that give rise to low-energy absorption peaks. These are suppressed for long water chains, however, infinitely long chains feature a strong excitonic peak at low photon energy. The local electric fields caused by the hydrate shell surrounding water monomers or clusters, however, are responsible for a large (more than one eV) competing shift of the optical absorption to higher energies. In fact, the calculations identify the local electric fields in the condensed water phases as the major force opening the optical transmission window of liquid and solid water compared to the gas phase. The *ab initio* structural model of nearly fourfold coordinated molecules in the liquid phase of water is found to be consistent with the optical absorption experiments.

I have seen too much not to know that the impression of a woman may be more valuable than the conclusion of an analytical reasoner.

Sir Arthur Conan Doyle

7 Conclusions

Describing aqueous systems correctly from *first principles* computer simulations has been and will remain challenging: the unique properties of the hydrogen bond, which create the vast number of physical and thermodynamical anomalies of water and ice, are difficult to grasp. It is, however, possible to achieve accurate *ab initio* results, provided care is taken when choosing computational methods and procedures.

The present work treats a heterogeneous ensemble of problems associated with the theoretical description of water and ice. Combining tools and methods from quantum chemistry and solid state physics proved necessary to achieve good agreement with experiment, and ultimately lead to a better understanding of ground- and excited-state properties of the systems studied.

Crystalline ice was studied using an incremental approach for the treatment of the correlation energy on many-body perturbation and coupled cluster levels of theory. It was shown that the many-body decomposition of the correlation energy essentially converge after summation of the two-body terms. Contributions from the three-body summation are much smaller, and were shown in the case of water clusters to be cancelled out by four-

body terms. Accordingly, excellent agreement with experimental data was achieved for the first time. Compared to results from DFT, significant improvement mainly of the binding energy, but also for structural parameters, was achieved. The fast convergence of the correlation energy in terms of the many-body decomposition hints at the possibility to simulate *ab initio* water, using periodic Hartree-Fock calculations together with a parametrized two-body potential for the correlation energy. The construction of such a potential is, however, beyond the scope of this work.

Adsorption of water molecules on the surface of ice was studied in a periodic framework from DFT calculations. Non-crystallographic surface adsorption sites were shown to provide binding energies higher than a simple bond counting argument would suggest, thus lowering the surface energy, and favouring the formation of rough surfaces. Possible follow-ups for this work could look into kinetic effects such as surface diffusion rates and barriers, and pre-melting of the surface at temperatures below the bulk melting point.

Studying excess charge localization is a very demanding task for theory and experiment alike. Excess electrons are present in the upper atmosphere as a result of the impact of ionizing cosmic radiation. Their influence on surface-assisted atmospheric reactions has, however, still to be assessed. It was shown that the correct treatment of excess charges needs to overcome the self-interaction issues present in DFT calculations. A partial self-interaction correction scheme was introduced and implemented, which proved crucial to avoid unphysical results. The localization of excess electrons at the surface of ice was found to be favourably supported by co-adsorbed water molecules as investigated in the previous chapter.

Optical excitation processes are a challenge for theoreticians. Apart from time-dependent DFT, the Green's function method offers the only feasible methodology for calculating optical spectra beyond the random phase approximation for extended systems. In water, the anomalous blueshift of the absorption onset upon condensation presented a long-standing challenge for theoretical descriptions. However, in this research, the optical spectrum of ice was calculated in very good agreement with experimental data by solving the Bethe-Salpeter equation for the two-particle polarization function. In

spite of this, due to the two-particle nature of the theory, there is a certain loss of self-evidence behind the optical spectrum's features. Thus, the two-particle spectrum served as a benchmark for an embedding model, which reduces the hydrogen bond interaction to its main part: the electrostatic dipole interaction. This model was found to sufficiently describe all main features of the optical spectrum of ice. Consequently, it was applied to a study of the optical spectrum of liquid water, which yielded a spectrum in quantitative agreement with experiment. Not only is this the first study to present quantitatively correct optical spectra for water in all three states of matter, but it also allowed the identification of the driving force in water's anomalous optical blueshift. Furthermore, it was thus shown that water structures from *first principles* molecular dynamics simulations yield correct optical shifts and spectra. With regard to the ongoing discussion in the literature about the coordination of water in the liquid state, it seems unnecessary, based on the findings of this research, to abandon the quasi-fourfold coordinated picture in favour of a twofold coordination scenario. However, if water simulations were able to produce such a twofold coordinated structure (which is not possible at present), the electrostatic embedding model introduced in this work could certainly be utilized, and would yield a spectroscopic fingerprint for useful comparison with experiment.

A

Publications

Peer-reviewed publications co-authored by Andreas Hermann while undertaking his PhD research at Massey University, as of April 17, 2009.

1. **A. Hermann**, P. Schwerdtfeger. Ground-state properties of crystalline ice from periodic Hartree-Fock and a coupled-cluster-based many-body decomposition of the correlation energy. *Phys. Rev. Lett.* **101**, 183005 (2008).
   Selected for *Virtual Journal of Biological Physics Research* **16(9)**, 2008.

2. **A. Hermann**, W. G. Schmidt, P. Schwerdtfeger. Resolving the Optical Spectrum of Water: Coordination and Electrostatic Effects. *Phys. Rev. Lett.* **100**, 207403 (2008).
   Selected for *Virtual Journal of Biological Physics Research* **15(11)**, 2008.

3. B. Vest, Z. Varga, M. Hargittai, **A. Hermann**, P. Schwerdtfeger. The Elusive Structure of $CrCl_2$ – A Combined Computational and Gas-Phase Electron-Diffraction Study. *Chem.-Eur. J.* **14**, 5130 (2008).

4. **A. Hermann**, P. Schwerdtfeger, W. G. Schmidt. Theoretical study of the localization of excess electrons at the surface of ice. *J. Phys.: Cond. Mat.* **20**, 225003 (2008).

5. W. G. Schmidt, M. Albrecht, S. Wippermann, S. Blankenburg, E. Rauls, F. Fuchs, C. Rödl, J. Furthmüller, **A. Hermann**. $LiNbO_3$ ground- and excited-state properties from first-principles calculations. *Phys. Rev. B* **77**, 035106 (2008).

6. **A. Hermann**, R. P. Krawczyk, M. Lein, P. Schwerdtfeger, I. P. Hamilton, J. J. P. Stewart. Convergence of the many-body expansion of interaction potentials: From van der Waals to covalent and metallic systems. *Phys. Rev. A* **76**, 013202 (2007).
   Selected for *Virtual Journal of Biological Physics Research* **14(3)**, 2007.

7. **A. Hermann**, M. Lein, P. Schwerdtfeger. The Search for the Species with the Highest Coordination Number. *Angew. Chem. Int. Ed.* **46**, 2444 (2007).

8. **A. Hermann**, B. Vest, P. Schwerdtfeger. Density functional study of α-$CrCl_2$: Structural, electronic, and magnetic properties. *Phys. Rev. B* **74**, 224402 (2006).

9. W. G. Schmidt, K. Seino, M. Preuss, **A. Hermann**, F. Ortmann, F. Bechstedt. Organic molecule adsorption on solid surfaces: chemical bonding, mutual polarisation and dispersion interaction. *Appl. Phys. A* **85**, 387 (2006).

10. C. Thierfelder, **A. Hermann**, P. Schwerdtfeger, W. G. Schmidt. Strongly bonded water monomers on the ice Ih basal plane: Density-functional calculations. *Phys. Rev. B* **74**, 045122 (2006).
    Selected for *Virtual Journal of Nanoscale Science & Technology* **14(6)**, 2006.

11. S. Biering, **A. Hermann**, W. G. Schmidt. Adsorption of water on chlorine-terminated Si(111) from first principles: Substrate-induced ordering versus intermolecular interactions. *Phys. Rev. B* **73**, 235429 (2006).
    Selected for *Virtual Journal of Nanoscale Science & Technology* **14(2)**, 2006.

12. W. G. Schmidt, **A. Hermann**, F. Fuchs, F. Bechstedt. Si(001) surface optical anisotropies induced by π-conjugated overlayers and oxidation. *Curr. Appl. Phys.* **6**, 525 (2006).

Bibliography

[1] W. S. Benedict, N. Gailar, and E. K. Plyler. Rotation-Vibration Spectra of Deuterated Water Vapor. *J. Chem. Phys.* **24**, 1139 (1956).

[2] S. A. Clough, Y. Beers, G. P. Klein, and L. S. Rothman. Dipole moment of water from Stark measurements of H_2O, HDO, and D_2O. *J. Chem. Phys.* **59(5)**, 2254 (1973).

[3] F. Martin and H. Zipse. Charge distribution in the water molecule - A comparison of methods. *J. Comput. Chem.* **26**, 97 (2005).

[4] V. F. Petrenko and R. W. Whitworth. *Physics of Ice*. Oxford University Press, Oxford (1999).

[5] G. Tammann. Ueber die Grenzen des festen Zustandes IV. *Ann. Phys.* **307(5)**, 1 (1900).

[6] B. Schwager and R. Boehler. H_2O: another ice phase and its melting curve. *High Press. Res.* **28(3)**, 431 (2008).

[7] O. Mishima, L. D. Calvert, and E. Whalley. 'Melting ice' I at 77 K and 10 kbar: a new method of making amorphous solids. *Nature* **310**, 393 (1984).

[8] O. Mishima and H. E. Stanley. The relationship between liquid, supercooled and glassy water. *Nature* **396**, 329 (1998).

[9] A. K. Soper. The radial distribution functions of water and ice from 220 to 673 K and at pressures up to 400 MPa. *Chem. Phys.* **258**, 121 (2000).

[10] P. Wernet, D. Nordlund, U. Bergmann, M. Cavalleri, M. Odelius, H. Ogasawara, L. A. Näslund, T. K. Hirsch, L. Ojamäe, P. Glatzel, L. G. M. Pettersson, and A. Nilsson. The Structure of the First Coordination Shell in Liquid Water. *Science* **304**, 995 (2004).

[11] Breakthrough of the Year: The Runners-Up. *Science* **306(5704)**, 2013 (2004).

[12] A. Szabo and N. S. Ostlund. *Modern Quantum Chemistry: Introduction to Advanced Electronic Structure Theory*. Dover Publications, New York (1996).

[13] F. Jensen. *Introduction to Computational Chemistry*. John Wiley & Sons Inc., Hoboken, NJ (1999).

[14] T. Helgaker, P. Jørgensen, and J. Olsen. *Molecular Electronic-Structure Theory*. John Wiley & Sons Inc., Hoboken, NJ (2000).

[15] N. W. Ashcroft and N. D. Mermin. *Solid State Physics*. Brooks/Cole, London (1976).

[16] C. Kittel. *Introduction to Solid State Physics*. John Wiley & Sons Inc., Hoboken, NJ (1996).

[17] G. D. Mahan. *Many-particle Physics*. Springer, Heidelberg (2000).

[18] V. S. Fock. Näherungsmethode zur Lösung des quantenmechanischen Mehrkörperproblems. *Z. Physik A* **61**, 126 (1930).

[19] J. C. Slater. The Theory of Complex Spectra. *Phys. Rev.* **34(10)**, 1293 (1929).

[20] C. Møller and M. S. Plesset. Note on an Approximation Treatment for Many-Electron Systems. *Phys. Rev.* **46**, 618 (1934).

[21] D. R. Hartree, W. Hartree, and B. Swirles. Self-Consistent Field, Including Exchange and Superposition of Configurations, with Some Results for Oxygen. *Phil. Trans. R. Soc. A* **238**, 229 (1939).

[22] S. F. Boys. Electronic Wave Functions. II. A Calculation for the Ground State of the Beryllium Atom. *Proc. R. Soc. Lond. A* **201**, 125 (1950).

[23] I. Shavitt. The history and evolution of configurationc interaction. *Mol. Phys.* **94**, 3 (1998).

[24] F. Coester. Bound states of a many-particle system. *Nucl. Phys.* **7**, 421 (1958).

[25] F. Coester and H. Kümmel. Short-range correlations in nuclear wave functions. *Nucl. Phys.* **17**, 477 (1960).

[26] O. Sinanoğlu. Many-Electron Theory of Atoms and Molecules. I. Shells, Electron Pairs vs Many-Electron Correlations. *J. Chem. Phys.* **36**, 706 (1962).

[27] J. Čížek. On the Correlation Problem in Atomic and Molecular Systems. Calculation of Wavefunction Components in Ursell-Type Expansion Using Quantum-Field Theoretical Methods. *J. Chem. Phys.* **45**, 4256 (1966).

[28] H. Nakatsuji and K. Hirao. Cluster expansion of the wavefunction. Symmetry-adapted-cluster expansion, its variational determination, and extension of open-shell orbital theory. *J. Chem. Phys.* **68(5)**, 2053 (1978).

[29] H. Nakatsuji. Cluster expansion of the wavefunction. Electron correlations in ground and excited states by SAC (symmetry-adapted-cluster) and SAC CI theories. *Chem. Phys. Lett.* **67**, 329 (1979).

[30] H. Nakatsuji. Cluster expansion of the wavefunction. Excited states. *Chem. Phys. Lett.* **59(2)**, 362 (1978).

[31] H. Nakatsuji. Cluster expansion of the wavefunction. Calculation of electron correlations in ground and excited states by SAC and SAC-CI theories. *Chem. Phys. Lett.* **67**, 334 (1979).

[32] P. Hohenberg and W. Kohn. Inhomogeneous Electron Gas. *Phys. Rev.* **136**, B864 (1964).

[33] W. Kohn and L. Sham. Self-Consistent Equations Including Exchange and Correlation Effects. *Phys. Rev.* **140(4A)**, A1133 (1965).

[34] D. M. Ceperley and B. J. Alder. Ground State of the Electron Gas by a Stochastic Method. *Phys. Rev. Lett.* **45**, 566 (1980).

[35] J. P. Perdew and A. Zunger. Self-interaction correction to density-functional approximations for many-electron systems. *Phys. Rev. B* **23**, 5048 (1981).

[36] S. H. Vosko, L. Wilk, and M. Nusair. Accurate Spin-Dependent Electron Liquid Correlation Energies for Local Spin-Density calculations - a critical anlysis. *Can. J. Phys.* **58**, 1200 (1980).

[37] E. Wigner. On the interaction of electrons in metals. *Phys. Rev.* **46**, 1002 (1934).

[38] M. Gell-Mann and K. A. Brueckner. Correlation Energy of an Electron Gas at High Density. *Phys. Rev.* **106**, 364 (1957).

[39] Y. Wang and J. P. Perdew. Correlation hole of the spin-polarized electron gas, with exact small-wave-vector and high-density scaling. *Phys. Rev. B* **44**, 13298 (1991).

[40] J. P. Perdew, J. A. Chevary, S. H. Vosko, K. A. Jackson, M. R. Pederson, D. J. Singh, and C. Fiolhais. Atoms, molecules, solids and surfaces: Applications of the generalized gradient approximation for exchange and correlation. *Phys. Rev. B* **46**, 6671 (1992).

[41] J. P. Perdew, K. Burke, and M. Ernzerhof. Generalized Gradient Expansion Made Simple. *Phys. Rev. Lett.* **77**, 3865 (1996).

[42] J. P. Perdew, R. G. Parr, M. Levy, and J. L. Balduz. Density-Functional Theory for Fractional Particle Number: Derivative Discontinuities of the Energy. *Phys. Rev. Lett.* **49(23)**, 1691 (1982).

[43] H. Stoll, C. M. E. Pavlidou, and H. Preuß. On the calculation of correlation energies in the spin-density functional formalism. *Theor. Chim. Acta* **49**, 143 (1978).

[44] M. d'Avezac, M. Calandra, and F. Mauri. Density functional theory description of hole-trapping in SiO_2: A self-interaction-corrected approach. *Phys. Rev. B* **71**, 205210 (2005).

[45] E. Runge and E. K. U. Gross. Density-Functional Theory for Time-Dependent Systems. *Phys. Rev. Lett.* **52(12)**, 997, Mar 1984.

[46] G. Vignale and W. Kohn. Current-Dependent Exchange-Correlation Potential for Dynamical Linear Response Theory. *Phys. Rev. Lett.* **77(10)**, 2037, Sep 1996.

[47] J. F. Dobson, G. Vignale, and M. P. Das, editors. *Electronic Density Functional Theory: Recent Progress and New Directions*. Springer, Heidelberg (1998).

[48] L. Hedin. New Method for Calculating the One-Particle Green's Function with Application to the Electron-Gas Problem. *Phys. Rev.* **139**, A796 (1965).

[49] L. Hedin and S. Lundqvist. *Solid State Physics*, volume 23, page 1. Academic Press, New York (1969).

[50] F. Aryasetiawan and O. Gunnarsson. The GW method. *Rep. Prog. Phys.* **61**, 237 (1998).

[51] G. Onida, L. Reining, and A. Rubio. Electronic excitations: density-functional versus many-body Green's-function approaches. *Rev. Mod. Phys.* **74(2)**, 601 (2002).

[52] A. A. Abrikosov, L. P. Gorkov, I. E. Dzyaloshinski, and R. A. Silverman. *Methods of Quantum Field Theory in Statistical Physics*. Dover Publications, New York (1975).

[53] M. S. Hybertsen and S. G. Louie. First-Principles Theory of Quasiparticles: Calculation of Band Gaps in Semiconductors and Insulators. *Phys. Rev. Lett.* **55**, 1418 (1985).

[54] R. W. Godby, M. Schlüter, and L. J. Sham. Accurate Exchange-Correlation Potential for Silicon and Its Discontinuity on Addition of an Electron. *Phys. Rev. Lett.* **56**, 2415 (1986).

[55] F. Bechstedt, R. D. Sole, G. Cappellini, and L. Reining. An efficient method for calculating quasiparticle energies in semiconductors. *Solid State Commun.* **84**, 765 (1992).

[56] M. S. Hybertsen and S. G. Louie. Electron correlation in semiconductors and insulators: Band gaps and quasiparticle energies. *Phys. Rev. B* **34(8)**, 5390 (1986).

[57] H. Ehrenreich and M. H. Cohen. Self-Consistent Field Approach to the Many-Electron Problem. *Phys. Rev.* **115**, 786 (1959).

[58] S. L. Adler. Quantum Theory of the Dielectric Constant in Real Solids. *Phys. Rev.* **126**, 413 (1962).

[59] N. Wiser. Dielectric Constant with Local Field Effects Included. *Phys. Rev.* **129**, 62 (1963).

[60] D. Weaire, D. Hobbsa, G. J. Morgan, J. M. Holenderb, and F. Wooten. New applications of the equation-of-motion method: Optical properties. *J. Non-Cryst. Solids* **166**, 877 (1993).

[61] S. Glutsch, D. S. Chemla, and F. Bechstedt. Numerical calculation of the optical absorption in semiconductor quantum structures. *Phys. Rev. B* **54**, 11592 (1996).

[62] W. G. Schmidt, S. Glutsch, P. H. Hahn, and F. Bechstedt. Efficient $\mathcal{O}(N^2)$ method to solve the Bethe–Salpeter equation. *Phys. Rev. B* **67**, 085307 (2003).

[63] J. D. Bernal and R. H. Fowler. A theory of water and ionic solution, with particular reference to hydrogen and hydroxyl ions. *J. Chem. Phys.* **1**, 515 (1933).

[64] L. Pauling. The Structure and Entropy of Ice and of Other Crystals with Some Randomness of Atomic Arrangement. *J. Am. Chem. Soc.* **57**, 2680 (1935).

[65] B. Kamb, W. C. Hamilton, S. J. LaPlaca, and A. Prakash. Ordered Proton Configuration in Ice II, from Single-Crystal Neutron Diffraction. *J. Chem. Phys.* **55(4)**, 1934 (1971).

[66] K. S. Kim, I. Park, S. Lee, K. Cho, J. Y. Lee, J. Kim, and J. D. Joannopoulos. The Nature of a Wet Electron. *Phys. Rev. Lett.* **76**, 956 (1996).

[67] S. Lee, J. Kim, S. J. Lee, and K. S. Kim. Novel Structures for the Excess Electron State of the Water Hexamer and the Interaction Forces Governing the Structures. *Phys. Rev. Lett.* **79(11)**, 2038 (1997).

[68] L. Turi, W.-S. Sheu, and P. J. Rossky. Characterization of Excess Electrons in Water-Cluster Anions by Quantum Simulations. *Science* **309**, 914 (2005).

[69] H. J. C. Berendsen, J. R. Grigera, and T. P. Straatsma. The missing term in effective pair potentials. *J. Phys. Chem.* **91**, 6269 (1987).

[70] W. L. Jorgensen, J. Chandrasekhar, J. D. Madura, R. W. Impey, and M. L. Klein. Comparison of simple potential functions for simulating liquid water. *J. Chem. Phys.* **79(2)**, 926 (1983).

[71] W. L. Jorgensen and J. D. Madura. Temperature and size dependence for Monte Carlo simulations of TIP4P water. *Mol. Phys.* **56**, 1381 (1985).

[72] M. W. Mahoney and W. L. Jorgensen. A five-site model for liquid water and the reproduction of the density anomaly by rigid, nonpolarizable potential functions. *J. Chem. Phys.* **112**, 8910 (2000).

[73] A. A. Chialvoa and P. T. Cummings. Simple transferable intermolecular potential for the molecular simulation of water over wide ranges of state conditions. *Fluid Phase Equil.* **150**, 73 (1998).

[74] B. Chen, J. Xing, and J. I. Siepmann. Development of Polarizable Water Force Fields for Phase Equilibrium Calculations. *J. Phys. Chem. B* **104(10)**, 2391 (2000).

[75] R. Bukowski, K. Szalewicz, G. C. Groenenboom, and A. van der Avoird. Predictions of the Properties of Water from First Principles. *Science* **315**, 1249 (2007).

[76] R. Bukowski, K. Szalewicz, G. C. Groenenboom, and A. van der Avoird. Polarizable interaction potential for water from coupled cluster calculations. I. Analysis of dimer potential energy surface. *J. Chem. Phys.* **128(9)**, 094313 (2008).

[77] R. Bukowski, K. Szalewicz, G. C. Groenenboom, and A. van der Avoird. Polarizable interaction potential for water from coupled cluster calculations. II. Applications to dimer spectra, virial coefficients, and simulations of liquid water. *J. Chem. Phys.* **128(9)**, 094314 (2008).

[78] D. Vanderbilt. Soft self-consistent pseudopotentials in a generalized eigenvalue formalism. *Phys. Rev. B Rapid Comm.* **41**, 7892 (1990).

[79] C. Lee, D. Vanderbilt, K. Laasonen, R. Car, and M. Parrinello. Ab initio studies on high pressure phases of ice. *Phys. Rev. Lett.* **69(3)**, 462 (1992).

[80] C. Lee, D. Vanderbilt, K. Laasonen, R. Car, and M. Parrinello. Ab initio studies on the structural and dynamical properties of ice. *Phys. Rev. B* **47**, 4863 (1993).

[81] R. Car and M. Parrinello. Unified Approach for Molecular Dynamics and Density-Functional Theory. *Phys. Rev. Lett.* **55(22)**, 2471 (1985).

[82] K. Laasonen, M. Sprik, M. Parrinello, and R. Car. "Ab initio" liquid water. *J. Chem. Phys.* **99**, 9080 (1993).

[83] K. Laasonen, A. Pasquarello, R. Car, C. Lee, and D. Vanderbilt. Car-Parrinello molecular dynamics with Vanderbilt ultrasoft pseudopotentials. *Phys. Rev. B* **47**, 10142 (1993).

[84] D. R. Hamann. H_2O hydrogen bonding in density-functional theory. *Phys. Rev. B* **55**, R10157 (1997).

[85] C. Thierfelder, A. Hermann, P. Schwerdtfeger, and W. G. Schmidt. Strongly bonded water monomers on the ice Ih basal plane: Density-functional calculations. *Phys. Rev. B* **74**, 045422 (2006).

[86] T. K. Hirsch and L. Ojamäe. Quantum-Chemical and Force-Field Investigations of Ice Ih: Computation of Proton-Ordered Structures and Prediction of Their Lattice Energies. *J. Phys. Chem. B* **108**, 15856 (2004).

[87] M. de Koning, A. Antonelli, A. J. R. da Silva, and A. Fazzio. Orientational Defects in Ice Ih: An Interpretation of Electrical Conductivity Measurements. *Phys. Rev. Lett.* **96**, 075501 (2006).

[88] E. Schwegler, G. Galli, and F. Gygi. Water under Pressure. *Phys. Rev. Lett.* **84**, 2429 (2000).

[89] Melting of ice under pressure. *Proc. Natl. Acad. Sci.* **105(39)**, 14779 (2008).

[90] B. C. Garrett. Ions at the Air/Water Interface. *Science* **303**, 1146 (2004).

[91] P. J. Feibelman. Substitutional NaCl hydration in ice. *Phys. Rev. B* **75(21)**, 214113 (2007).

[92] V. F. Petrenko and I. A. Ryzhkin. Electron energy spectrum of ice. *Phys. Rev. Lett.* **71**, 2626 (1993).

[93] I. Morrison, J.-C. Li, S. Jenkins, S. S. Xantheas, and M. C. Payne. Ab-Initio Total Energy Studies of the Static and Dynamical Properties of Ice Ih. *J. Phys. Chem. B* **101**, 6146 (1997).

[94] J. C. Slater. Atomic Shielding Constants. *Phys. Rev.* **36(1)**, 57 (1930).

[95] S. F. Boys. Electronic Wave Functions. I. A General Method of Calculation for the Stationary States of Any Molecular System. *Proc. R. Soc. London A* **200**, 542 (1950).

[96] W. Schulze and D. Kolb. H_2^+ correlation diagram from finite element calculations. *Chem. Phys. Lett.* **122**, 271 (1985).

[97] E. L. Briggs, D. J. Sullivan, and J. Bernholc. Real-space multigrid-based approach to large-scale electronic structure calculations. *Phys. Rev. B* **54**, 14362 (1996).

[98] H. Hellmann. A New Approximation Method in the Problem of Many Electrons. *J. Chem. Phys.* **3(1)**, 61 (1935).

[99] E. Fermi. Motion of neutrons in hydrogenous substances. *Ricerca Sci.* **7**, 13 (1936).

[100] J. C. Phillips and L. Kleinman. New Method for Calculating Wave Functions in Crystals and Molecules. *Phys. Rev.* **116**, 287 (1959).

[101] D. Hamann, M. Schlüter, and C. Chiang. Norm-Conserving Pseudopotentials. *Phys. Rev. Lett.* **43**, 1494 (1979).

[102] Pseudopotentials that work: From H to Pu. *Phys. Rev. B* **26**, 4199 (1982).

[103] N. Troullier and J. L. Martins. Efficient pseudopotentials for plane-wave calculations. *Phys. Rev. B* **43**, 1993 (1991).

[104] P. E. Blöchl. Projector augmented-wave method. *Phys. Rev. B* **50**, 17953 (1994).

[105] G. Kresse and J. Furthmüller. Efficient iterative schemes for *ab initio* total-energy calculations using a plane-wave basis set. *Phys. Rev. B* **54**, 11169 (1996).

[106] G. Kresse and D. Joubert. From ultrasoft pseudopotentials to the projector augmented-wave method. *Phys. Rev. B* **59**, 1758 (1999).

[107] H. J. Monkhorst and J. D. Pack. Special points for Brillouin-zone integration. *Phys. Rev. B* **13**, 5188 (1976).

[108] P. Vinet, J. Ferrante, J. R. Smith, and J. H. Rose. A universal equation of state for solids. *J. Phys. C: Solid State Phys.* **19**, L467 (1986).

[109] E. Whalley. The Difference in the Intermolecular Forces of H_2O and D_2O. *Trans. Faraday Soc.* **53**, 1578 (1957).

[110] R. Brill and A. Tippe. Gitterparameter von Eis I bei tiefen Temperaturen. *Acta Crystallogr.* **23**, 343 (1967).

[111] P. H. Gammon, H. Kiefte, and M. J. Clouter. Elastic constants of ice samples by Brillouin spectroscopy. *J. Phys. Chem.* **87(21)**, 4025 (1983).

[112] P. Fulde. *Electron Correlations in Molecules and Solids*. Springer Series in Solid-State Sciences. Springer, Heidelberg (1995).

[113] R. J. Bartlett and M. Musiał. Coupled-cluster theory in quantum chemistry. *Rev. Mod. Phys.* **79(1)**, 291 (2007).

[114] H. Stoll. Correlation energy of diamond. *Phys. Rev. B* **46(11)**, 6700 (1992).

[115] B. Paulus. The method of increments - a wavefunction-based ab initio correlation method for solids. *Phys. Rep.* **428(1)**, 1 (2006).

[116] N. Gaston, B. Paulus, K. Rosciszewski, P. Schwerdtfeger, and H. Stoll. Lattice structure of mercury: Influence of electronic correlation. *Phys. Rev. B* **74(9)**, 094102 (2006).

[117] A. Hermann, R. P. Krawczyk, M. Lein, P. Schwerdtfeger, I. P. Hamilton, and J. J. P. Stewart. Convergence of the many-body expansion of interaction potentials: From van der Waals to covalent and metallic systems. *Phys. Rev. A* **76**, 013202 (2007).

[118] I. G. Kaplan, R. Santamaria, and O. Novaro. Non-Additive Forces in Atomic Clusters. The case of Ag_n. *Mol. Phys.* **84(1)**, 105 (1995).

[119] R. Dovesi, V. R. Saunders, C. Roetti, R. Orlando, C. M. Zicovich-Wilson, F. Pascale, B. Civalleri, K. Doll, N. M. Harrison, I. J. Bush, P. D'Arco, and M. Llunell. CRYSTAL06 User's Manual. University of Torino, Torino, 2006.

[120] E. Polak. *Computational Methods in Optimization*. Academic Press, New York (1971).

[121] W. H. Preuss, S. A. Teukolsky, W. T. Vetterling, and B. P. Flannery. *Numerical Recipes in Fortran: The Art of Scientific Computing*. Cambridge University Press, Cambridge (1992).

[122] S. F. Boys and F. Bernardi. The calculation of small molecular interactions by the differences of separate total energies. Some procedures with reduced errors. *Mol. Phys.* **19(4)**, 553 (1970).

[123] L. Valenzano, F. J. Torres, K. Doll, F. Pascale, C. M. Zicovich-Wilson, and R. Dovesi. *Ab Initio* Study of the Vibrational Spectrum and Related Properties of Crystalline Compounds; the Case of $CaCO_3$ Calcite. *Z. Phys. Chem.* **220(7)**, 893 (2006).

[124] J. Scaranto and S. Giorgianni. A quantum-mechanical study of CO adsorbed on TiO_2: A comparison of the Lewis acidity of the rutile (110) and the anatase (101) surfaces. *J. Mol. Struct.: THEOCHEM* **858**, 72 (2008).

[125] R. Kendall, T. Dunning, Jr., and R. Harrison. Electron affinities of the first-row atoms revisited. Systematic basis sets and wave functions. *J. Chem. Phys.* **96**, 6796 (1992).

[126] A. J. Thakkar, T. Koga, M. Saito, and R. E. Hoffmeyer. Double and Quadruple Zeta Contracted Gaussian Basis Sets for Hydrogen through Neon. *Int. J. Quant. Chem.* **48(27)**, 343 (1993).

[127] B. Silvi. Importance of electrostatic interactions between nonbonded molecules in ice. *Phys. Rev. Lett.* **73**, 842 (1994).

[128] L. Ojamäe, K. Hermansson, R. Dovesi, C. Roetti, and V. Saunders. Mechanical and molecular properties of ice VIII from crystal-orbital *ab initio* calculations. *J. Chem. Phys.* **100**, 2128 (1994).

[129] P. C. Hariharan and J. A. Pople. The influence of polarization functions on molecular orbital hydrogenation energies. *Theo. Chim. Acta* **28(3)**, 213 (1973).

[130] R. Krishnan, J. Binkley, R. Seeger, and J. Pople. Self-consistent molecular orbital methods. XX. A basis set for correlated wave functions. *J. Chem. Phys.* **72**, 650 (1980).

[131] T. H. Dunning, Jr. Gaussian basis sets for use in correlated molecular calculations. I. The atoms boron through neon and hydrogen. *J. Chem. Phys.* **90(2)**, 1007 (1989).

[132] K. Raghavachari, G. W. Trucks, J. A. Pople, and M. Head-Gordon. A fifth-order perturbation comparison of electron correlation theories. *Chem. Phys. Lett.* **157**, 479 (1989).

[133] R. J. Bartlett. Coupled-Cluster Approach to Molecular Structure and Spectra: A Step toward Predictive Quantum Chemistry. *J. Phys. Chem.* **93**, 1697 (1989).

[134] P. Schwerdtfeger, N. Gaston, R. P. Krawczyk, R. Tonner, and G. E. Moyano. Extension of the Lennard-Jones potential: Theoretical investigations into rare-gas clusters and crystal lattices of He, Ne, Ar, and Kr using many-body interaction expansions. *Phys. Rev. B* **73(6)**, 064112 (2006).

[135] G. Dantl. Die elastischen Moduln von Eis-Einkristallen. *Phys. Kondens. Mater.* **7(5)**, 390 (1968).

[136] A. Hermann, W. G. Schmidt, and P. Schwerdtfeger. Resolving the Optical Spectrum of Water: Coordination and Electrostatic Effects. *Phys. Rev. Lett.* **100**, 207403 (2008).

[137] T. Todorova, A. Seitsonen, J. Hutter, I.-F. Kuo, and C. Mundy. Molecular Dynamics Simulation of Liquid Water: Hybrid Density Functionals. *J. Phys. Chem. B* **110(8)**, 3685 (2006).

[138] M. Städele, J. A. Majewski, P. Vogl, and A. Görling. Exact Kohn-Sham Exchange Potential in Semiconductors. *Phys. Rev. Lett.* **79**, 2089 (1997).

[139] S. Ivanov, S. Hirata, and R. J. Bartlett. Exact Exchange Treatment for Molecules in Finite-Basis-Set Kohn-Sham Theory. *Phys. Rev. Lett.* **83(26)**, 5455 (1999).

[140] H. H. G. Jellinek. Liquid-like (transition) layer on ice. *J. Colloid Interface Sci.* **25**, 192 (1967).

[141] J. G. Dash, A. W. Rempel, and J. S. Wettlaufer. The physics of premelted ice and its geophysical consequences. *Rev. Mod. Phys.* **78**, 695 (2006).

[142] M. Faraday. Note on Regelation. *Proc. R. Soc. London* **10**, 440 (1860).

[143] N. Materer, U. Starke, A. Barbieri, M. A. Van Hove, G. A. Somorjai, G.-J. Kroes, and C. Minot. Molecular Surface Structure of a Low-Temperature Ice Ih(0001) Crystal. *J. Phys. Chem.* **99**, 6267 (1995).

[144] N. Materer, U. Starke, A. Barbieri, M. A. Van Hove, G. A. Somorjai, G.-J. Kroes, and C. Minot. Molecular surface structure of ice(0001): dynamical low-energy electron diffraction, total-energy calculations and molecular dynamics simulations. *Surf. Sci.* **381**, 190 (1997).

[145] J. Braun, A. Glebov, A. P. Graham, A. Menzel, and J. P. Toennies. Structure and Phonons of the Ice Surface. *Phys. Rev. Lett.* **80**, 2638 (1998).

[146] P. Parent, C. Laffon, C. Mangeney, F. Bournel, and M. Tronc. Structure of the water ice surface studied by x-ray absorption spectroscopy at the O K-edge. *J. Chem. Phys.* **117**, 10842 (2002).

[147] D. Nordlund, H. Ogasawara, P. Wernet, M. Nyberg, M. Odelius, L. Pettersson, and A. Nilsson. Surface structure of thin ice films. *Chem. Phys. Lett.* **395**, 161 (2004).

[148] X. Wei, P. B. Miranda, and Y. R. Shen. Surface Vibrational Spectroscopic Study of Surface Melting of Ice. *Phys. Rev. Lett.* **86**, 1554 (2001).

[149] H. Dosch, A. Lied, and J. H. Bilgram. Glancing-angle X-ray scattering studies of the premelting of ice surfaces. *Surf. Sci.* **327**, 145 (1995).

[150] G.-J. Kroes. Surface melting of the (0001) face of TIP4P ice. *Surf. Sci.* **275**, 365 (1992).

[151] Y. A. Mantz, F. M. Geiger, L. T. Molina, and M. J. Molina. First-principles molecular-dynamics study of surface disordering of the (0001) face of hexagonal ice. *J. Chem. Phys.* **113**, 10733 (2000).

[152] E. R. Batista and H. Jonsson. Diffusion and Island formation on the ice Ih basal plane surface. *Comp. Mat. Sci.* **20**, 325 (2001).

[153] J. M. Douillard and M. Henry. Calculation of surface enthalpy of solids from an ab initio electronegativity based model: case of ice. *J. Coll. Int. Sci.* **263(2)**, 554 (2003).

[154] R. Defay, I. Prigogine, A. Bellemans, and D. H. Everett. *Surface Tension and Adsorption*. Longmans Green London (1966).

[155] F. N. Keutsch and R. J. Saykally. Water clusters: Untangling the mysteries of the liquid, one molecule at a time. *Proc. Natl. Acad. Sci.* **98**, 10533 (2001).

[156] M. Schlüter, J. R. Chelikowsky, S. G. Louie, and M. L. Cohen. Self-consistent pseudopotential calculations for Si (111) surfaces: Unreconstructed (1 x 1) and reconstructed (2 x 1) model structures. *Phys. Rev. B* **12**, 4200 (1975).

[157] W. G. Schmidt, F. Bechstedt, and G. P. Srivastava. Adsorption of group-V elements on III-V(110) surfaces. *Surf. Sci. Rep.* **25**, 141 (1996).

[158] K. Seino, W. G. Schmidt, and F. Bechstedt. Organic modification of surface electronic properties: A first principles study of uracil on Si(001). *Phys. Rev. B* **69**, 245309 (2004).

[159] S. Solomon. Strastospheric Ozone Depletion: A Review of Concepts and History. *Rev. Geophys.* **37(3)**, 275 (1999).

[160] J. P. D. Abbatt. Interactions of Atmospheric Trace Gases with Ice Surfaces: Adsorption and Reaction. *Chem. Rev.* **103**, 4783 (2003).

[161] E. J. Hart and J. W. Boag. Absorption Spectrum of the Hydrated Electron in Water and in Aqueous Solutions. *J. Am. Chem. Soc.* **84**, 4090 (1962).

[162] M. Armbruster, H. Haberland, and H.-G. Schindler. Negatively Charged Water Clusters, or the First Observation of Free Hydrated Electrons. *Phys. Rev. Lett.* **47(5)**, 323 (1981).

[163] C. Gahl, U. Bovensiepen, C. Frischkorn, and M. Wolf. Ultrafast Dynamics of Electron Localization and Solvation in Ice Layers on Cu(111). *Phys. Rev. Lett.* **89**, 107402 (2002).

[164] J. Stähler, M. Mehlhorn, U. Bovensiepen, M. Meyer, D. O. Kusmierek, K. Morgenstern, and M. Wolf. Impact of Ice Structure on Ultrafast Electron Dynamics in D_2O Clusters on Cu(111). *Phys. Rev. Lett.* **98**, 206105 (2007).

[165] G. Baldacchino, V. D. Waele, H. Monard, S. Sorgues, F. Gobert, J. Larbre, G. Vigneron, J. Marignier, S. Pommeret, and M. Mostafavi. Hydrated electron decay measurements with picosecond pulse radiolysis at elevated temperatures up to 350 °C. *Chem. Phys. Lett.* **424**, 77 (2006).

[166] D. Nordlund, H. Ogasawara, H. Bluhm, O. Takahashi, M. Odelius, M. Nagasono, L. G. M. Pettersson, and A. Nilsson. Probing the Electron Delocalization in Liquid Water and Ice at Attosecond Time Scales. *Phys. Rev. Lett.* **99**, 217406 (2007).

[167] R. N. Barnett, U. Landman, C. L. Cleveland, and J. Jortner. Electron localization in water clusters. II. Surface and internal states. *J. Chem. Phys.* **88(7)**, 4429 (1988).

[168] J. V. Coe, G. H. Lee, J. G. Eaton, S. T. Arnold, H. W. Sarkas, K. H. Bowen, C. Ludewigt, H. Haberland, and D. R. Worsnop. Photoelectron spectroscopy of hydrated electron cluster anions, $(H_2O)^-_{n=2-69}$. *J. Chem. Phys.* **92(6)**, 3980 (1990).

[169] P. Ayotte, G. H. Weddle, C. G. Bailey, M. A. Johnson, F. Vila, and K. D. Jordan. Infrared spectroscopy of negatively charged water clusters: Evidence for a linear network. *J. Chem. Phys.* **110(13)**, 6268 (1999).

[170] D. M. A. Smith, J. Smets, and L. Adamowicz. Ab initio theoretical study of dipole–bound anions of molecular complexes: Water pentamer anions. *J. Chem. Phys.* **110(8)**, 3804 (1999).

[171] N. I. Hammer, J.-W. Shin, J. M. Headrick, E. G. Diken, J. R. Roscioli, G. H. Weddle, and M. A. Johnson. How Do Small Water Clusters Bind an Excess Electron? *Science* **306**, 675 (2004).

[172] H. M. Lee, S. B. Suh, P. Tarakeshwar, and K. S. Kim. Origin of the magic numbers of water clusters with an excess electron. *J. Chem. Phys.* **122(4)**, 044309 (2005).

[173] A. E. Bragg, J. R. R. Verlet, A. Kammrath, O. Cheshnovsky, and D. M. Neumark. Hydrated Electron Dynamics: From Clusters to Bulk. *Science* **306**, 669 (2004).

[174] J. R. R. Verlet, A. E. Bragg, A. Kammrath, O. Cheshnovsky, and D. M. Neumark. Observation of Large Water-Cluster Anions with Surface-Bound Excess Electrons. *Science* **307**, 93 (2005).

[175] T. Sommerfeld and K. D. Jordan. Electron Binding Motifs of $(H_2O)_n^-$ Clusters. *J. Am. Chem. Soc.* **128**, 5828 (2006).

[176] F. Baletto, C. Cavazzoni, and S. Scandolo. Surface Trapped Excess Electrons on Ice. *Phys. Rev. Lett.* **95**, 176801 (2005).

[177] Á. Madarász, P. J. Rossky, and L. Turi. Excess electron relaxation dynamics at water/air interfaces. *J. Chem. Phys.* **126**, 234707 (2007).

[178] Y. Yoon and S. Shin. Effects of surface trapped excess electrons on the dynamics of HCl adsorbed ice surfaces. *Chem. Phys. Lett.* **440**, 83 (2007).

[179] U. Lundin and O. Eriksson. Novel method of self-interaction corrections in density functional calculations. *Int. J. Quant. Chem.* **81**, 247 (2001).

[180] B. Liu. In C. Moler and I. Shavitt, editors, *Report on Workshop "Numerical Algorithms in Chemistry: Algebraic Methods"*, page 49, Berkeley, CA (1978). Lawrence Berkeley Lab.

[181] E. R. Davidson. Methods in computational molecular physics. In G. H. F. Diercksen and S. Wilson, editors, *NATO Advanced Study Institute*, volume 113, page 95. Plenum, New York (1983).

[182] P. Pulay. Convergence Acceleration of Iterative Sequences. The Case of SCF Iteration. *Chem. Phys. Lett.* **73**, 393 (1980).

[183] P. Bendt and A. Zunger. *Bull. Am. Phys. Soc.* **27**, 248 (1982).

[184] D. M. Wood and A. Zunger. A new method for diagonalising large matrices. *J. Phys. A: Math. Gen.* **18(9)**, 1343 (1985).

[185] G. Makov and M. C. Payne. Periodic boundary conditions in ab initio calculations. *Phys. Rev. B* **51**, 4014 (1995).

[186] U. Gerstmann, P. Deák, R. Rurali, B. Aradi, T. Frauenheim, and H. Overhof. Charge corrections for supercell calculations of defects in semiconductors. *Phys. B: Cond. Mat.* **340**, 190 (2003).

[187] A. F. Wright and N. A. Modine. Comparison of two methods for circumventing the Coulomb divergence in supercell calculations for charged point defects. *Phys. Rev. B* **74(23)**, 235209 (2006).

[188] N. Bjerrum. Structure and Properties of Ice. 1. Position of the Hydrogen Atoms and the Zero-Point Entropy. 2. Change in Configuration and Molecular Turns. 3. Ionisation of Ice and Molecular Turns Produced by the Ions - the Proton Jump Conductivity of Ice (and Water). *Mat.-Fys. Medd. K. Dan. Vidensk. Selsk.* **27**, 1 (1951).

[189] R. Podezwa and V. Buch. Structure and Dynamics of Orientational Defects in Ice. *Phys. Rev. Lett.* **83**, 4570 (1999).

[190] N. Bjerrum. Structure and properties of ice. *Science* **115**, 385 (1952).

[191] M. T. Suter, P. U. Andersson, and J. B. C. Pettersson. Surface properties of water ice at 150-191 K studied by elastic helium scattering. *J. Chem. Phys.* **125**, 174704 (2006).

[192] S.-H. Lee, D. C. Leard, R. Zhang, L. T. Molina, and M. J. Molina. The HCl+$ClONO_2$ reaction rate on various water ice surfaces. *Chem. Phys. Lett.* **340**, 7 (1999).

[193] Q.-B. Lu and L. Sanche. Effects of Cosmic Rays on Atmospheric Chlorofluorocarbon Dissociation and Ozone Depletion. *Phys. Rev. Lett.* **87(7)**, 078501 (2001).

[194] N. R. P. Harris, J. C. Farman, and D. W. Fahey. Comment on "Effects of Cosmic Rays on Atmospheric Chlorofluorocarbon Dissociation and Ozone Depletion". *Phys. Rev. Lett.* **89(21)**, 219801 (2002).

[195] P. K. Patra and M. S. Santhanam. Comment on "Effects of Cosmic Rays on Atmospheric Chlorofluorocarbon Dissociation and Ozone Depletion". *Phys. Rev. Lett.* **89(21)**, 219803 (2002).

[196] R. Onaka and T. Takahashi. Vacuum UV Absorption Spectra of Liquid Water and Ice. *J. Phys. Soc. Jpn.* **24**, 548 (1968).

[197] G. D. Kerr, R. N. Hamm, M. W. Williams, R. D. Birkhoff, and L. R. Painter. Optical and Dielectric Properties of Water in the Vacuum Ultraviolet. *Phys. Rev. A* **5**, 2523 (1972).

[198] J. M. Heller, Jr., R. N. Hamm, R. D. Birkhoff, and L. R. Painter. Collective oscillation in liquid water. *J. Chem. Phys.* **60**, 3483 (1974).

[199] H. Hayashi, N. Watanabe, Y. Udagawa, and C.-C. Kao. The complete optical spectrum of liquid water measured by inelastic x-ray scattering. *Proc. Natl. Acad. Sci.* **97**, 6264 (2000).

[200] M. Sprik, J. Hutter, and M. Parrinello. Ab initio molecular dynamics simulation of liquid water: Comparison of three gradient-corrected density functionals. *J. Chem. Phys.* **105**, 1142 (1996).

[201] P. L. Silvestrelli and M. Parrinello. Structural, electronic, and bonding properties of liquid water from first principles. *J. Chem. Phys.* **111**, 3572 (1999).

[202] Towards an assessment of the accuracy of density functional theory for first principles simulations of water. *J. Chem. Phys.* **120**, 300 (2004).

[203] D. Marx. Proton Transfer 200 Years after von Grotthuss: Insights from Ab initio Simulations. *ChemPhysChem* **7**, 1848 (2006).

[204] B. Santra, A. Michaelides, and M. Scheffler. On the accuracy of density-functional theory exchange-correlation functionals for H bonds in small water clusters: Benchmarks approaching the complete basis set limit. *J. Chem. Phys.* **127**, 184104 (2007).

[205] J. VandeVondele, F. Mohamed, M. Krack, J. Hutter, M. Sprik, and M. Parrinello. The influence of temperature and density functional models in ab initio molecular dynamics simulation of liquid water. *J. Chem. Phys.* **122(1)**, 014515 (2005).

[206] M. V. Fernández-Serra and E. Artacho. Network equilibration and first-principles liquid water. *J. Chem. Phys.* **121**, 11136 (2004).

[207] V. Garbuio, M. Cascella, L. Reining, R. Del Sole, and O. Pulci. *Ab Initio* calculation of optical spectra of liquids: Many-body effects in the electronic excitations of water. *Phys. Rev. Lett.* **97**, 137402 (2006).

[208] L. R. Painter, R. N. Hamm, E. T. Arakawa, and R. D. Birkhoff. Electronic properties of liquid water in the vacuum ultraviolet. *Phys. Rev. Lett.* **21(5)**, 282 (1968).

[209] P. H. Hahn, W. G. Schmidt, and F. Bechstedt. Molecular electronic excitations calculated from a solid-state approach: Methodology and numerics. *Phys. Rev. B* **72**, 245425 (2004).

[210] P. H. Hahn, W. G. Schmidt, K. Seino, M. Preuss, F. Bechstedt, and J. Bernholc. Optical Absorption of Water: Coulomb Effects versus Hydrogen Bonding. *Phys. Rev. Lett.* **94**, 037404 (2004).

[211] D. Prendergast and G. Galli. X-Ray Absorption Spectra of Water from First Principles Calculations. *Phys. Rev. Lett.* **96**, 215502 (2006).

[212] B. Hetényi, F. D. Angelis, P. Giannozzi, and R. Car. Calculation of near-edge x-ray-absorption fine structure at finite temperatures: Spectral signatures of hydrogen bond breaking in liquid water. *J. Chem. Phys.* **120(18)**, 8632 (2004).

[213] M. Cavalleri, M. Odelius, D. Nordlund, A. Nilsson, and L. G. M. Pettersson. Half or full core hole in density functional theory X-ray absorption spectrum calculations of water? *Phys. Chem. Chem. Phys.* **7**, 2854 (2005).

[214] M. Odelius, M. Cavalleri, A. Nilsson, and L. G. M. Pettersson. X-ray absorption spectrum of liquid water from molecular dynamics simulations: Asymmetric model. *Phys. Rev. B* **73(2)**, 024205 (2006).

[215] L. Reining, V. Olevano, A. Rubio, and G. Onida. Excitonic Effects in Solids Described by Time-Dependent Density-Functional Theory. *Phys. Rev. Lett.* **88**, 066404 (2002).

[216] M. J. Frisch et al. Gaussian 03, Revision C.02. Gaussian, Inc., Wallingford, CT, 2004.

[217] K. Kobayashi. Optical Spectra and Electronic Structure of Ice. *J. Phys. Chem.* **87**, 4317 (1982).

[218] W. F. Chan, G. Cooper, and C. E. Brion. The electronic spectrum of water in the discrete and continuum regions. Absolute optical oscillator strengths for photoabsorption (6-200 eV). *Chem. Phys.* **178**, 387 (1993).

[219] D. M. Chipman. Excited electronic states of small water clusters. *J. Chem. Phys.* **122**, 044111 (2005).

[220] J. A. Odutola and T. R. Dyke. Partially deuterated water dimers: Microwave spectra and structure. *J. Chem. Phys.* **72**, 5062 (1980).

[221] A. Halkier, H. Koch, P. Jørgensen, O. Christiansen, I. M. B. Nielsen, and T. Helgaker. A systematic ab initio study of the water dimer in hierarchies of basis sets and correlation models. *Theor. Chem. Acc.* **97**, 150 (1997).

[222] A. Osted, J. Kongsted, K. V. Mikkelsen, and O. Christiansen. Linear Response Properties of Liquid Water Calculated Using CC2 and CCSD within Different Molecular Mechanics Methods. *J. Phys. Chem. A* **108**, 8646 (2004).

[223] C. A. Coulson and D. Eisenberg. Interactions of H_2O Molecules in Ice. II. Interaction Energies of H_2O Molecules in Ice. *Proc. Roy. Soc. London* **291**, 454 (1965).

[224] E. R. Batista, S. S. Xantheas, and H. Jónsson. Molecular multipole moments of water molecules in ice Ih. *J. Chem. Phys.* **109**, 4546 (1998).

[225] P. L. Silvestrelli and M. Parrinello. Water Molecule Dipole in the Gas and in the Liquid Phase. *Phys. Rev. Lett.* **82**, 3308 (1999).

[226] M. Cavalleri, H. Ogasawara, L. G. M. Pettersson, and A. Nilsson. The interpretation of X-ray absorption spectra of water and ice. *Chem. Phys. Lett.* **364**, 363 (2002).